Controlling the physical microenvironment of cells with microfluidics for studying mechanically regulated cellular behaviors

Submitted in partial fulfillment of the requirements for the

degree of

Doctor of Philosophy

in

Department of Mechanical Engineering

Utku M. Sönmez

B.S., Mechanical Engineering Department, Istanbul Technical
University M.S., Biomedical Engineering Department, Carnegie
Mellon University

Carnegie Mellon University
Pittsburgh, PA

August 2022

ACKNOWLEDGEMENTS

Regarding the academic matters, first, I would like to thank my advisor, Philip LeDuc, for supporting and guiding me throughout my graduate school. I still cannot wrap my head around how someone can be that nice and I believe investigation of this would easily be a separate PhD thesis. I also would like to thank our collaborators Lance Davidson, Pawel Kalinski, Jonathan Minden, Beth Roman, Greg Delgoffe, and Dayana Rivadeneira for opening their labs to me and making this work possible with their helps, insights, and fruitful discussions. Last but not least, I would like to express my gratitude to my thesis committee members Rebecca Taylor, Jonathan Minden, Beth Roman, and the thesis committee chair Philip LeDuc for helping me in putting my research studies together.

Regarding the social matters, I am deeply indebted to my family, specifically to my mom Ferah Sönmez and to my cousin Pembegul Inamli for always supporting me in every aspect of my life and literally keeping me alive. I would like to thank again to my advisor Philip LeDuc for supporting me not only in the academic matters but also at personal level and outside the university as well. I also would like to thank my Pittsburgh friends, Joey Anolik, Drew Brisley, Mana Aliabadi and many others for always welcoming fresh off the boat guy like me and making me feel at home throughout the years that I spent here.

Regarding internal motivation, I would like to thank all the natural philosophers and scientists of the past, from ancient Greece to 21st century, for inspiring me to dedicate a good portion of my life to research. Also, I should acknowledge the thinkers who also produced considerable number of

popular science assays such as Carl Sagan, Ernst Mayr, Richard Feynman, Richard Dawkins, Bertrand Russel, Celâl Şengör, Çağrı Mert Bakırcı and many others for attracting my attention to philosophy, science, technology, and skepticism since my teenage years.

Lastly, I want to thank my loyal portable space heater for accompanying me during the never-ending cold days of Pittsburgh in the last five years or so. I lost her to a tragic overheating accident a couple of days ago. May her soul rest in peace.

ABSTRACT

Mechanical cues are one of the most important biophysical regulators of cellular machinery under both physiological and pathophysiological conditions. Advancements in the microtechnology in the last two decades allowed researchers to develop automated, high-throughput, and multifunctional experimental tools based on microfluidic techniques in order to facilitate conventional mechanobiological experiments and enable novel experimental paradigms that would not be possible otherwise. In this work, we developed various microfluidic devices and techniques that can be used to generate different mechanical microenvironments for the understanding of the role of mechanical cues at the cellular level.

Suspended mammalian cells such as lymphocytes constantly migrate within the tissues following the complex patterns of chemokine gradients in order to carry out diverse immune system functions. The in vitro analysis of the immune cell migration under precisely controlled microenvironments have a potential to enable in-depth understanding of the mechanism that regulate immune cell motility behaviors. However, in order to unveil the cell migration through cellular locomotion suspended immune cells should be isolated from external mechanical forces such as shear stress dependent drag forces. Therefore, we generated a microfluidic flow-free gradient generator system and used this approach with Jurkat cells to analyze their motion patterns within various CXCL12 gradients and extracellular matrix configuration. Using this system, we found that the strength of the chemotactic response of Jurkat cells to CXCL12 gradient was reduced by increasing surface fibronectin in a dose-dependent manner. Moreover, we the observed that the chemotaxis of Jurkat cells was governed not only by the CXCL12 gradient but also by the average CXCL12 concentration. Moreover, we developed a framework where the distinct migratory behaviors in response to chemokine gradients in different contexts

might be physiologically relevant for shaping the host immune response and may serve to optimize the targeting and accumulation of immune cells to the inflammation site. Lastly, we used this system with primary murine CD8+ T cells obtained from either healthy mice or B16 mouse tumor model in order investigate effect of tumor microenvironment in T cell motility.

Another example of the biological phenomena where mechanics plays an important role is development. *Drosophila melanogaster* (fruit fly) is a well-established model organism which has been used in developmental biology studies for over a century. Although most of the Drosophila research largely focused on biochemistry and genetics as the regulatory mechanisms for development, recent studies showed that both internally and externally generated mechanical signals also play an important role during development. In this regard, we developed a novel microfluidic system for automatically aligning and loading hundreds of Drosophila embryos into microchannels where they can be simultaneously compressed to desired levels using pneumatically actuated deformable sidewalls. Using this microsystem, we demonstrated the effect of different levels of acute and chronic compression on the developmental progression and viability of the *Drosophila* embryos. Furthermore, we quantitatively characterized dose- and time-dependent induction of the ectopic expression of *Twist* —a crucial transcription factor that governs gastrulation process— upon mechanical compression.

One of most mechanically sensitive cell type in mammalian body is the endothelial cells —monolayer of which constitutes the inner wall of the vasculature— as they are constantly subjected to mechanical cues in the form of blood shear stress. We further enhanced the scope of this work by developing a novel microfluidic system that can generate various physiologically relevant shear stress modalities such as different levels of shear stress and shear stress gradients for the investigation of endothelial cell polarity and orientation in response to flow which is

considered to be a marker for endothelial dysfunction. In this microfluidic device, human umbilical vein endothelial cells (HUVECs) exhibited a rapid and robust response to shear stress, with the relative positioning of the Golgi and nucleus transitioning from non-polarized to polarized in a shear stress magnitude- and gradient-independent manner. By contrast, polarized HUVECs oriented their Golgi and nucleus polarity to the flow vector in a shear stress magnitude-dependent manner, with positive shear stress gradients inhibiting and negative shear stress gradients promoting this upstream orientation.

Lastly, we developed a new microfabrication technique called Polycarbonate Heat Molding (PCH molding) that can facilitate the fabrication of microfluidic devices. We tested this technique with master molds fabricated through photolithography, mechanical micromilling as well as 3D printing. Using this technique, we were able to successfully copy microstructures with submicron feature sizes and high aspect ratios. We characterized the copying fidelity of this technique and tested mechanically active microfluidic devices fabricated via PCH molding. We also used this approach to combine different master molds with up to 19 unique geometries into a single monolithic copy mold in a single step displaying the effectiveness of the copying technique over a large footprint area to scale up the microfabrication. This novel microfabrication technique can be performed outside the cleanroom without using any sophisticated equipment, suggesting a simple way for high-throughput rigid monolithic mold fabrication that can be used in mechanobiological studies.

Table of Contents

LIST OF FIGURES

Chapter 1 Figures

Chapter 2 Figures

Chapter 3 Figures

Chapter 4 Figures

Chapter 0: Introduction to this Thesis

Microfluidics is an interdisciplinary field that include both the science and technology of microtechnological systems that handles small amounts of fluids through the use of microchannels that have dimensions ranging from tens to hundreds of micrometers[1]. Since the introduction of rapid prototyping techniques in the second half of 1990s, biomedical microfluidics have attracted an immense attention and the number of number of applications in this field increased exponentially since then. Characteristic properties of microfluidic systems often emerge only at small length scales such as strict control over spatiotemporal parameters, reduced sample volume, precise flow regimes, predictable mass or energy transfer, portability, parallel and streamlined assaying capability as well as easy integration with microsensors, actuators, microcontrollers and other automation tools[2]. These properties enable them to be used to devise novel biological assays that would be extremely hard if not impossible to have with conventional laboratory techniques.

Understanding how biological organisms function as a system at cellular, subcellular, and macroscopic levels is still one of the key problems of modern biology after it was highlighted by Edmund Beecher Wilson more than a century ago: "There is at present no biological question of greater moment than the means by which the individual cell-activities are coordinated, and the organic unity of the body maintained; for upon this question hangs not only the problem of the transmission of acquired characters, and the nature of development, but our conception of life itself"[3]. Today, it is known that the genetic, epigenetic, and environmental cues regulate biological processes to determine how system-level functions are achieved. However, how these

cues synchronously regulate and execute the complex biological processes such as development, motility, and vascular homeostasis in an astonishingly robust manner across many different species still begs an answer[4]. Further understanding of the complex spatiotemporal interactions that enable these biological processes requires precisely controlled interventions and high-throughput experimental systems to unveil the unique role of each of these cues on the process that is under investigation[5].

In the past two decades, it has been increasingly evident that one of the key environmental factors that contributes to the functionality and the fate of biological systems is mechanical effects such as hydrostatic pressure, shear stress, compression, and tension. This is because all the living beings are subjected to physical laws and biophysical cues such as mechanical forces are affecting them at all scales ranging from individual proteins to whole organs and tissues where cells are equipped with variety of modules that can either internally generate mechanical forces or sense the externally generated mechanical forces through their mechanotransduction mechanisms. Impairment of one these modules can contribute to the etiology of diseases and pathophysiological conditions. The term mechanobiology is therefore coined to refer to the investigation of the mechanical effects in biological systems at the cellular and subcellular level[6]. The actual potential of mechanobiological studies in elucidating various biological phenomena was recently recognized worldwide as the 2021 Nobel Prize in Physiology or Medicine was awarded to David Julius and Ardem Patapoutian for their joint effort in discovering cellular transducers such as TRP and PIEZO that sense and respond to mechanical cues.

It is not a simple coincidence that both the increased focus into mechanics at cellular level and the development of microfluidic systems appeared at the same time. This is because

microfluidic technologies are capable of generating different modes of spatiotemporally controlled mechanical stimulations which can be used for devising novel biological assays for the quantitative characterization of the mechanical considerations in various biological phenomena such as development, cellular motility, and vascular homeostasis. Further advancement in new microfabrication techniques and their implementation in mechanobiology studies have a potential to foster interdisciplinary research studies as engineers familiarize themselves with biological systems while presenting the most recent advances in microengineering strategies to biologists, promoting mutual understanding. Keeping this in mind this work has been established through various collaborations between engineers such as myself and biologists. To emphasize the interdisciplinary nature of this work, I tend to use the pronoun "we" instead of "I" throughout this thesis.

In the chapter 1 of this thesis, which is based on my recent publication; Sonmez et al., Micromachines, 2020[7], I introduced a microfluidic approach that we developed for the investigation of the motility of suspended immune cells within stable chemokine gradients. Although the generation of stable chemokine gradients requires the constant flow of chemokine solutions, our approach manages to isolate the immune cells from the flow channels in order prevent them from being dragged by the flow. This flow-free stable chemokine gradient generation approach therefore enabled us to observe the motions of the suspended cells over a long period of time as a result of the forces generated internally by themselves. Furthermore, we designed this system in such a way that the cells can be imaged with high resolution confocal microscopy. This feature of our microfluidic system facilitated the imaging of a single cell in detail paving the way of other research studies for the investigation of cellular locomotion mechanisms. We characterized this microfluidic flow-free concentration gradient generation

system using analytical, numerical, and finally experimental techniques. After completing this step, we conducted proof-of-concept experiments with Jurkat cells (a human T cell lymphoma line) using this system. Our results indicated that both the intensity of extracellular matrix on which cells were moving and the properties associated with chemokine concentration gradient independently regulate the resultant motility characteristics of the cells. Interestingly, while the increased surface extracellular matrix concentration made cells more motile as expected, it also prevented cells to follow chemokine gradients, leading to random cell migration pattern. A similar effect was also observed when the average concentration of the chemokine gradient was increased. However, these results as well as other characteristics of cell motility that we observed may indeed have a functional role in the recruitment of immune cells to the inflammation site. Based on our results, we speculate a paradigm that optimizes the duration of immune cell recruitment while increasing the possibility of the contact of immune cells with target cells at the inflammation site. After completing the proof-of-concept applications, we continued to use an improved version of this system with primary murine CD8+ T cells (also known as cytotoxic T cells) that contain genetically encoded fluorogen-activating protein (FAP) which targets their mitochondria. In this way, we could specifically damage the mitochondria of these T cells upon illumination with infrared light before the cell motility experiments without killing them. This approach enabled us to investigate the role of mitochondria in T cell motility within chemokine gradients. Furthermore, we repeated these experiments in a hypoglycemic environment in order to observe the interplay between role of mitochondrial function and glucose concentration of media in regulating the motility. Our results indicated that mitochondrial activity was crucial for the high motility rates for CD8+ T cells while it enhanced the random motility component of chemotaxis. On the other hand, hypoglycemic environment had an opposite effect where it

reduced the extend of cell motility while promoting cells to follow chemotactic cues. As T cell

motility is crucial for the destruction of target cells, and mitochondrial dysfunction and

hypoglycemic microenvironment are very well-known side effects of tumor microenvironment

(TME), we believe this study will be very relevant to development of new strategies for T cell-

based immunotherapies.

In the chapter 2 of this thesis, which is based on another recent publication of mine;

Sonmez et al., Lab on a Chip, 2019[8], I presented an entirely novel microfluidic approach that can

be used to align, immobilize, and mechanically stimulate various multicellular biological entities

ranging from the whole embryos of small model organisms to tumor organoids with high

throughput (i.e. it can simultaneously process around 180 of them). This approach took

advantage of the elastic nature of the polydimethylsiloxane (PDMS), one of the most commonly

used material to fabricate microfluidic channels. By designing this microfluidic system in such a

way that the target organisms were surrounded by thin deformable PDMS walls and we were

able to mechanically compress them through pneumatic actuation. Similar to chapter 1, we first

characterized this system using analytical, numerical, and experimental tools. After that, we

conducted our experiments with fruit flies (*Drosophila melanogaster*) in order to investigate the

effects of external mechanical compression on gastrulation process: a crucial step in embryonic

development which transforms otherwise similar cells in blastula into three germ layers by cell

migration and rearrangement. Our results indicated that the fruit fly embryos can continue to

develop in a normal fashion within the microfluidic system for prolonged times. The

compression, on the other hand, either slowed down the development or completely the killed the

embryos when it was applied for prolonged durations and at high doses. However, when the

mechanical compression was applied at a reasonable dose the survival rate of the fruit flies

increased. We also found out that this level of compression induces higher expression of one of the transcription factors, *twist*, which is crucial for the gastrulation process.

In chapter 3 of this thesis, which is also based on one of my recent publications; Sonmez et al., Lab on a Chip, 2020[9], I showcased another novel microfluidic system that we developed in order to apply different physiological shear stress modalities. Similar to the gradients of soluble factors mentioned in chapter 1, the gradients of shear stress are also thought to be affecting the migration of mechanosensitive cells (such as endothelial cells that are constantly exposed to shear stress caused by blood flow) via regulating their orientation and polarization. The main goal of this project was to identify the polarization and orientation of the Human Umbilical Vein Endothelial Cells (HUVECs, a primary human endothelial cell type isolated from the umbilical cords of the babies) in response to different fluid shear stress modalities created within this microfluidic system. We designed this system such that these different fluid shear stress modalities can be generated simultaneously within the same device by connecting 14 microchannel geometries in parallel. Needless to mention, this approach allowed us to conduct 14 experiments at the same time, saving a lot of time and resources. After characterizing this microfluidic system similarly using analytical, numerical, and experimental means, we conducted shear stress experiments and investigated the HUVEC responses to shear stress via endpoint imaging. Our final results indicated that increased levels of shear stress magnitude cause Golgi-nucleus orientation of the endothelial cells against flow, a hint which may imply the migration of these cells against the flow. We also observed that the gradients of shear stress either inhibits or promotes the Golgi-nucleus orientation against flow, depending on the direction of shear stress gradient where the negative shear stress gradients (meaning that the shear stress magnitude is decreasing in the direction of the flow) promoting and the positive shear stress

gradients (meaning that the shear stress magnitude is increasing in the direction of the flow) inhibiting the orientation against the flow. Unlike the Golgi-nucleus orientation, our results indicated that the Golgi-nucleus polarization is equally boosted by shear stress regardless of the magnitude or the gradient. This device has already started being used by other researchers at the University of Pittsburgh for the investigation of the downstream signaling mechanisms that regulate the polarization, orientation, and migration of endothelial cells in response to fluid shear stress.

Lastly, in the chapter 4 of this thesis, which again is based on one of my publications; Sonmez et al., Small, 2020[10], I introduced a new microfabrication technique for the fabrication of complex microfluidic channels and geometries that can be used in mechanobiology studies. This approach suggests a way to copy the existing micropatterned molds into a unified monolithic polycarbonate mold which in turn can be used for high throughput fabrication of microstructures out of elastomeric polymers outside the cleanroom facilities. In this way, our technique enabled the fabrication of microstructures and even nanostructures without risking the expensive and fragile master molds. Furthermore, here I described the steps of this fabrication in detail, showed various complex geometries we readily fabricated using this technique, and defined the limits of this approach. As a proof-of-concept experiment, I also showed the fabrication of the embryo compression microchannels presented in chapter 2 of this thesis and tested them through pneumatic actuation in order to present the copying fidelity of this technique. I hope that this simple technique can also be useful for other researchers without engineering background to fabricate microengineered geometries for their mechanobiology studies as it can be performed without using any sophisticated equipment.

Chapter 1: Microfluidics-enabled Investigation of Immune Cell Motility

Introduction

In nature, gradients of soluble molecules guide cellular responses in biological activities ranging from embryogenesis[11], tissue regeneration[12], and axon growth in neural development[13] to immune cell activation and migration[14]. In addition, many immunodeficiency diseases, autoimmune diseases[15], chronic inflammation[16], and cancer metastases[17,18] develop as a result of pathological sensing or establishing inappropriate gradients of soluble signaling molecules[19]. Therefore, the characterization of cellular responses to soluble cell-signaling molecules and to their gradients is of great importance for understanding how multicellular collective behaviors are organized and regulated. Understanding the roles of gradient sensing in disease also guides us toward novel therapies including regenerative stem cell therapy for neural injury, localized drug delivery for immunomodulation of inflammatory diseases[20], and T-cell engineering for the immunotherapy of cancer[21].

Most *in vitro* and *ex vivo* migration models used to evaluate the responses of different cells to individual chemokines involve specialized migration chambers such as the Boyden chamber[22]. Boyden chambers have two reservoirs, an upper and lower chamber, separated by a semipermeable membrane. Once a chemokine is diluted into the upper chamber a transient concentration gradient develops. If responsive, cells initially seeded in the upper chamber sense the gradient and migrate into the lower chamber. Cell movements in the Boyden chamber are essentially 1-dimensional as cells move from one compartment to another. The major limitation of Boyden chambers and other similar systems lies in their inability to track spatial and

temporal parameters of cell migration. Additionally, since these systems allow only limited control over the microenvironment, cells cannot be challenged by sequential events, such as the ability on one chemokine to sensitize cells to exposure by subsequent factors.

Microtechnology provides novel tools that allow precise spatiotemporal control over microenvironments to better understand the operation of complex biological systems [23-25]. Advances in microfabrication over the last two decades have enabled the development of sophisticated microfluidic chemotaxis systems where dynamic and complex movement of chemotactic cells can be studied in precisely defined microenvironments[26]. The first generation of microfluidic chemotaxis systems that enabled precise control of biochemical concentration gradients relied on diffusion between adjacent laminar flow streams[27,28]. Variations of these flow-based gradient systems have been widely applied to study cellular responses to ligand gradients; however, it is now apparent that fluid flow over migrating cells can both modulate the concentration distribution of soluble molecules across the cell membrane[29] as well as exert shear stress on cells[30,31]. These coupled characteristics can cause issues as cells that normally do not experience shear stress in their native environment respond differentially to signaling molecules when shear stress is present[32]. For instance, some chemokine receptors such as CXCR4 (receptor of CXCL12) can be downregulated by laminar shear stress[33]. Moreover, bulk fluid flow continuously elutes autocrine and paracrine factors secreted by migrating cells. Continuous elution in these systems may eliminate the biochemical communication networks established by collectively migrating cells under normal physiological conditions. These studies suggest it that it is important to minimize using flow-based devices for chemotaxis studies of cells that do not normally experience flow in their physiological microenvironment.

To establish flow-free conditions, microfluidic devices can incorporate porous materials such as hydrogels, matrigel, or agarose[34-39]. Although, these systems can create stable gradients, their applications have been limited since they often require extended times to establish a gradient due to the relatively low diffusivity in porous materials[40]. More complex designs that rely on sink and source channels connected with ladder-shaped microgroove arrays have been developed to overcome this problem[41-44]. In some of these designs, transient gradients can be established[45] in a short period of time; however, fabrication of these multi-depth[46] and multilayer channels[47] can be complex and require extensive usage of cleanroom facilities[48]. However, simpler implementations of these ladder-shaped designs are possible by creating a direct pressure balance between the flow fields in sink and source channels[49-51], but these designs are often susceptible to mechanical noise from syringe pumps that introduce pressure imbalance across the gradient chamber[52].

We developed a microtechnology that would enable rapid progress in future studies of chemotaxis[53] through a defined set of design criteria. Such technology should (1) have the ability to generate concentration gradients in flow-free conditions; (2) have the ability to create combinatorial chemical gradients to mimic physiologically-relevant complex gradient patterns; (3) be compatible with media and thin cover slips to enable high-resolution time-lapse imaging with oil immersion objectives; (4) have the ability to develop stable gradients and to exchange media to allow for long-term analysis; (5) be compatible with manual micropipettes to allow simple assembly and fluid-handling; (6) allow co-fabrication of multiple parallel chambers with different gradient slopes in a single microfluidic device; and (7) have low volume media consumption to reduce costs of reagent usage.

In this study, we develop a microfluidic chemotaxis system to meet all of these design considerations. Our device generates flow-free concentration gradient by the diffusion of soluble species from two flow channels into a microchamber[52]. We fabricate our system by combining AM with conventional soft lithography[54] for rapid-prototyping as improvements in the feature resolution of AM techniques have facilitated the fabrication of complex microfluidic systems without a need for expensive materials and cleanroom facilities[55,56]. Our approach enables high resolution confocal imaging of diffusible fluorescent reporters and allows us to validate the gradient formation against theoretical calculations and finite-element modelling (FEM). We then apply a CXCL12 chemokine gradient together with a controlled fibronectin surface concentration to investigate Jurkat cells motility which is a human T cell lymphoma cell line frequently used for studying cell signaling in immune cell chemotaxis[57,58].

Materials and Methods

System Design

The microfluidic system was made of two separate PDMS layers that sandwich a 0.4 µm PC membrane filter (EMD Millipore, Billerica, MA) **(Figure 1.1a)**[59]. The upper layer consisted of two symmetric flow channels, their respective inlet and outlet ports, and a cell introduction port. The lower layer consisted of narrow and wide flow-free chambers that spanned 1.9 and 2.9 mm, respectively. Fluidic resistance was created by the membrane at the sides of the upper surface of the flow-free chamber that blocked the fluid flow from the upper flow channels to the lower chambers, leaving diffusion as the main mechanism for mass transfer between the two flow channels. Linear concentration gradients of soluble species were formed within the

flow-free chamber as species diffuse through the semipermeable membrane. Continuous

exchange between the upper and lower layers kept the reagent concentrations constant in the

flow-free gradient chambers **(Figure 1.1b)**. The concentration gradients generated within the

chambers were determined based on the steady-state version of Fick's Second Law (i.e.

$\partial c / \partial t = 0$):

$$\frac{\partial^2 c}{\partial x^2} + \frac{\partial^2 c}{\partial y^2} + \frac{\partial^2 c}{\partial z^2} = 0 \qquad \text{(eq. 1.1)}$$

where c was the local concentration and x, y, and z were Cartesian coordinates defined

within the chambers **(Figure 1.1c inset)**. As the concentrations at the chamber boundaries did

not change in the y-direction (along the length of the chamber), the second term of Eq. (1) was

neglected. Although, the concentration gradient generated in x-direction (across the width of

the chamber) dominates, a shallow concentration gradient is also formed in the z-direction

(along the depth of the chamber) due to the height of the gradient chambers. Therefore, the

height of the gradient chamber was selected carefully to avoid deviation of the concentration

gradient by more than $\pm 5\%$ between the top and bottom surface of the gradient chambers.

Different gradient patterns can be produced depending on the application's requirements, for

instance, one flow channel can be filled with only a buffer solution while the other one can be

supplied with a buffer containing a soluble molecule to create single species concentration

gradients from one side. Alternatively, both channels can be filled with the solutions of

different soluble molecules to generate combinatorial gradients. Furthermore, both flow

channels can contain the same reagent to establish combinatorial gradients of two species on

top of the uniform concentration background of a third species. Concentration gradients in the

flow-free chamber can be measured directly by imaging fluorophores with similar molecular weight to that of the chemokines (e.g. FITC-dextran MW:10,000 or Fluoro-ruby MW: 10,000).

Small media reservoirs (500 μm radius) were fabricated in our PDMS device near the flow channel inlets to reduce flow fluctuations such as those caused by a syringe pump that might otherwise introduce a pressure imbalance between two flow channels. Cells were seeded into the gradient chambers through a cell introduction port through micropipetting prior to establishing the gradient **(Figure 1.1c)**. The height of the cell introduction port was one-half of the height of the gradient chamber to generate a more homogenous distribution of cells within the gradient chamber **(Figure 1.1c inset)**. Stable gradients were established once cells attached to the bottom glass surface of the gradient chamber.
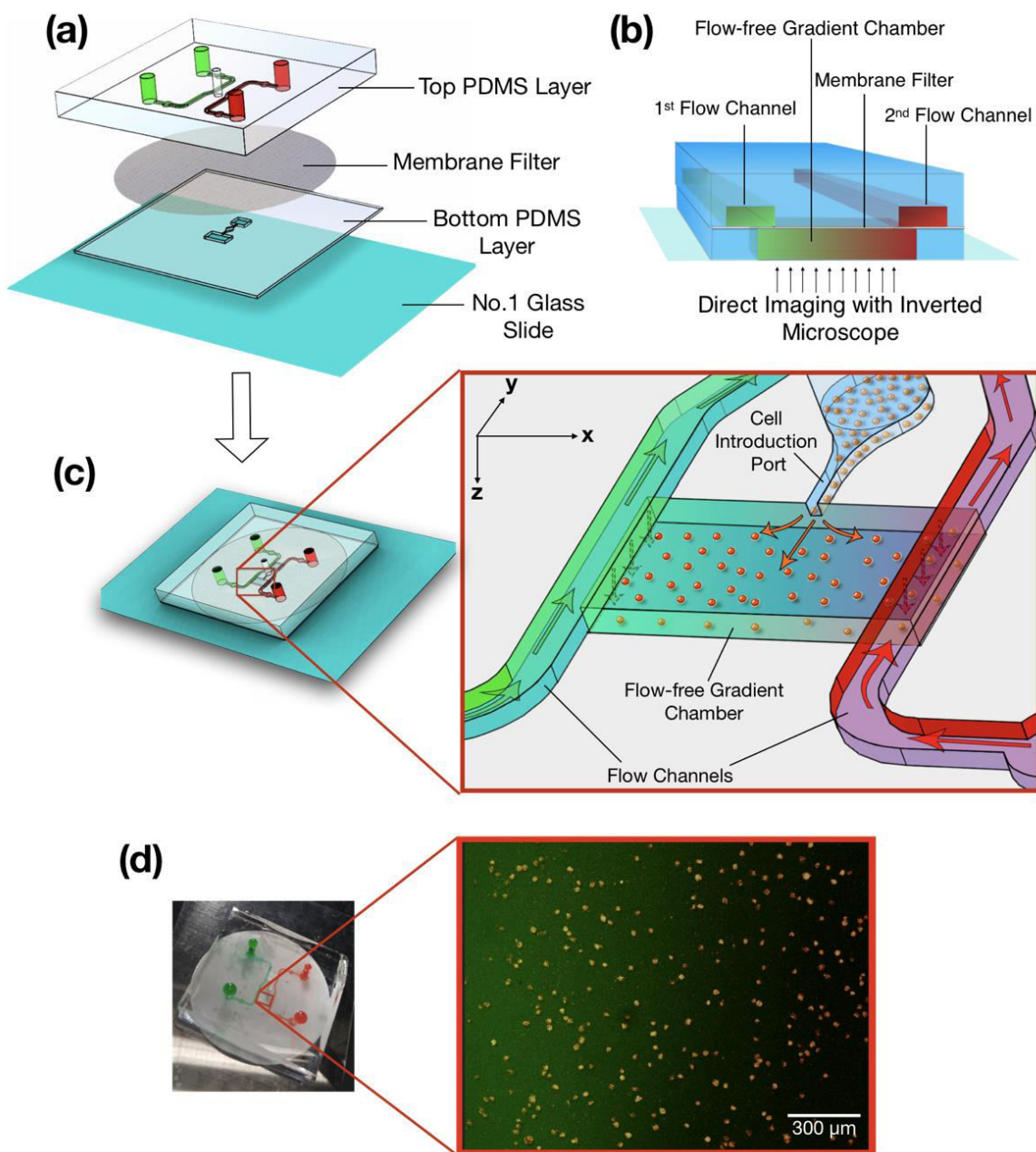
Figure 1. 1 Chemotaxis of Jurkat cells in microfluidic flow-free gradient chambers. (a) An enlarged view of microfluidic flow-free gradient generator. The top PDMS layer has two parallel flow channels and a cell introduction port that is connected to bottom PDMS layer with a membrane filter. The entire assembly is attached to a thin glass coverslip at the bottom to enable high numerical aperture imaging. (b) Schematic of the flow-free gradient chamber approach. Soluble species diffuse through the membrane to the bottom layer creating linear concentration gradients in the flow-free gradient chambers. (c) Schematic of the microfluidic device after assembly. (inset) The introduction of cells into the gradient chamber through the cell introduction port and the generation of a gradient across the cells. (d) Image of the actual microfluidic device where flow channels are filled with dye for visualization after fabrication. (inset) Composite fluorescent image taken from the flow-free-gradient chamber where the Jurkat cells are in a linear concentration gradient of FITC-Dextran.

Fabrication

Both layers of the microfluidic device were fabricated using PDMS replica molding. First, negatives of the 3D channel geometries were drawn in SolidWorks 2016 (Dassault Systèmes, Vélizy-Villacoublay, France). The negative molds for both layers of the device were manufactured using VIPER si2T Stereolithography System (3D Systems, Rock Hill, South California, USA) in high quality mode with Accura SI 10 Polymer as the photocurable resin. Fabricated molds were post-cured with UV and their functional surfaces were coated with Tridecafluoro-1,1,2,2-tetrahydrooctyl-1-trichlorosilane (TFOCS, United Chemical Technology, product no. T2492). Sylgard 184 PDMS (Dow Corning, Midland, Michigan, USA), was mixed with its curing agent at a 5:1 mass ratio, and the mixture was degassed. Pre-cured PDMS was then poured on the molds slowly to avoid any bubble formation **(Figure 1.2a)**. For the fabrication of the thin lower layer, a polycarbonate (PC) sheet was laid over the pre-cured PDMS and a 500-g weight was placed on top of the PC sheet to put mechanical pressure on the pre-cured PDMS to reduce the final PDMS thickness needed for hollow gradient chambers **(Figure 1.2d,e)**. Upper and lower parts were then placed in a 60°C convection oven for 1 hour. After curing, the lower part was removed from the mold and bonded to a 45 mm x 50 mm #1.5 cover slip after treating their surfaces with oxygen plasma (Harrick Plasma Cleaner, 1 min, 18 W). The upper layer was also removed from the mold, and its inlet and outlet holes were punched with a G20 blunt tip needle **(Figure 1.2b)**. Integration of the membrane filter and the PDMS parts was accomplished through a silane coupling technique, which was performed by immersing the PC membrane

filter in a 5% solution of 3-aminopropyltriethoxysilane (APTES, Sigma-Aldrich) that has been

pre-warmed to 80 °C for 20 minutes. The solution was covered during the process to avoid

evaporation. Later, the membrane filter was removed from the solution and both faces were

dried for 10 seconds. Immediately afterwards, the membrane filter and the upper PDMS layer

of the microfluidic system were placed in an oxygen plasma cleaner for 20 seconds to create an

irreversible bond between them **(Figure 1.2c)**. The lower PDMS-glass slide assembly was bound

to the upper PDMS layer in the same manner so that the PC membrane was sandwiched

between these two PDMS layers. To improve alignment, we assembled the device within the

field-of-view of a stereo microscope immediately after the oxygen plasma treatment (see

Figure 1.2f for assembled device).

Before using the microfluidic system in cell migration studies, the gradient chambers

were coated with fibronectin which one of the most commonly used ECM proteins for in vitro

chemotaxis assays[60]. The fibronectin was diluted to the desired concentration in 0.2 μm filtered

deionized (DI) water, chambers filled with fibronectin solution through the cell introduction

port, and the microfluidic system kept at 37°C until the solution dried.
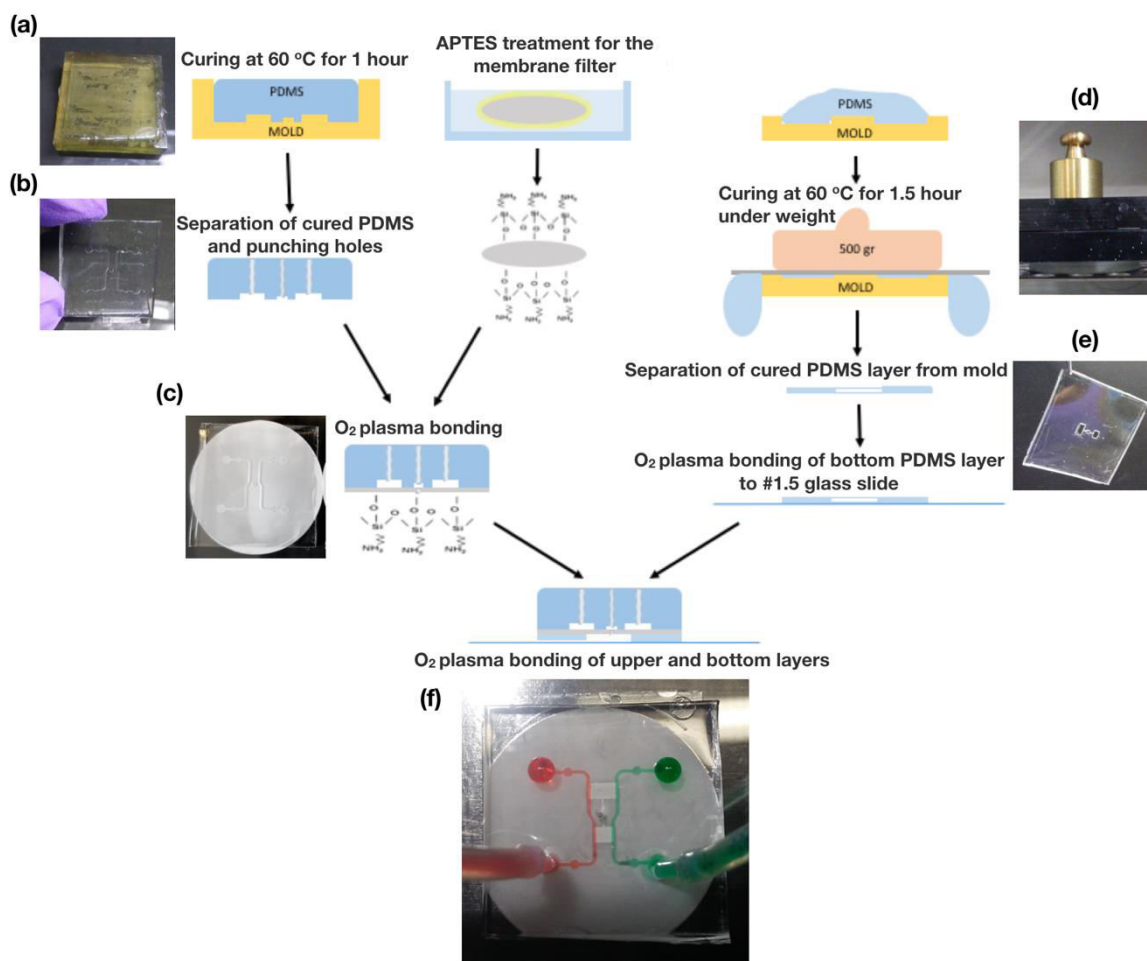
Figure 1. 2 Fabrication of our flow-free microfluidic device. (a) Uncured PDMS is poured into 3D printed molds. (b) After curing, the top PDMS layer is separated from the mold, and inlet and outlet holes are punched. (c) A polycarbonate membrane is bonded to the top PDMS layer through O_2 plasma bonding after APTES treatment. (d) A weight is placed on top of the pre-cured PDMS during the curing process to create a thin PDMS layer with the gradient chambers. (e) Image of the bottom PDMS layer with hollow gradient chambers after being separated from the mold. (f) Functional flow-free microfluidic device with green and red dye in water for flow visualization.

Experimental setup

Our microfluidic system was connected to a Chemyx Fusion digital double-syringe pump (Thermo Scientific, Waltham, MA) with 1 mL plastic syringes (BD plastic, Franklin Lakes, NJ) and thin polyethylene tubing (ID: 0.58 mm, OD:0.965 mm) to minimize reagent consumption. The microfluidic system was then placed in a stage-top environmental chamber (Pathology Devices,

17

Westminster, MD) where temperature, humidity, and CO_2 concentration was controlled by an environmental chamber control unit to maintain incubation conditions (37°C, 5% CO_2, and %90 humidity).

Confocal time-lapse sequences for cell tracking and gradient observation were captured using a confocal laser scan head (SP5 Leica Microsystems) mounted on an inverted compound microscope (DMI6000, Leica Microsystems) equipped with APO 10X/0.4 n.a. dry objective. A 488 nm Argon laser was used to illuminate stained cells and FITC-Dextran, and a 543 nm HeNe laser was used for live gradient observation (Fluoro-ruby). High resolution images of Jurkat cells were acquired using APO 63X/1.4 n.a. oil immersion objective.

Cell culture

Jurkat cells were grown in ATCC-formulated RPMI-1640 Medium supplemented with 10% Fetal Bovine Serum (FBS) (Sigma-Aldrich, MO, USA) and 1% 100 U/mL penicillin-streptomycin (Sigma-Aldrich, MO, USA). Cells were sub-cultured every 3 to 4 days and kept in sterile incubation conditions for mammalian cells (37°C, 5% CO_2, and 90% humidity) according to ATCC protocols. Jurkat cells were assessed for expression of CD3, CXCR4, and CCR5 by flow cytometry **(Appendix 1.1)**. The percentage of CD3$^+$ Jurkat cells was 27.8%. For the chemokine receptors, while 99.4% was CXCR4$^+$, only 1.78% was found to be CCR5$^+$. Although Jurkat cells originate from T cells where the CD3 molecule is constitutively expressed on the cell surface, their heterogeneity in terms of CD3 expression was previously reported[61]; we found no correlation between CD3$^-$ and CXCR4$^-$ expression.

For vital staining, 500 µL of cell suspension was collected and counted from the culture flask. The viability was evaluated using a Trypan Blue exclusion test with a hemocytometer.

Samples with less than 90% viability were discarded prior to staining. Cells were then centrifuged and diluted to 1 million-cell/mL in 1X Phosphate Buffered Saline (PBS) (Sigma-Aldrich, MO, USA). CellTracker Green BOPIDY dye (ThermoFisher Scientific, MA, USA) was added to the cell suspension to bring the suspension to a 25 µM final concentration. Cells were incubated for 45 minutes, and subsequently centrifuged and diluted to 300,000 cells/mL in cell culture medium. Jurkat cells were introduced to the fibronectin coated gradient chambers by micropipetting 3 uL of cell/culture media through the cell introduction port. The final cell seeding density in the flow-free chambers was approximately 160 cells/mm^2.

Image acquisition and cell tracking

Leica Microsystems, Confocal time-lapse sequences at 1-minute intervals were captured 10 minutes after gradient establishment to track cells and observe gradients for 30 minutes (LASAF, Leica Microsystems). Cells were then automatically tracked using the Linear Assignment Problem (LAP) algorithm[62] in the ImageJ plug-in TrackMate[63]. We selected 100 to 200 cell tracks from each chamber; tracks that lasted less than half of the imaging period were not considered (i.e. tracks that lasted less than 15 minutes for 30 minutes of observation) to reduce spurious cells that entered into or exited from the imaging region during the image acquisition. The tracking data was analyzed using the IBIDI Chemotaxis and Migration Tool (IBIDI GmbH, Martinsried, Germany), MATLAB (MathWorks Inc., MA, USA), and Numbers software (Apple Inc., CA, USA). Cells were initially sorted into motile and non-motile categories. Cells were considered non-motile if their accumulated displacement (e.g. path length) was less than 30 µm over 30 minutes of tracking (i.e. 1 µm/min average speed). Motile cells were subsequently analyzed for quantitative cell migration parameters.

The chemotactic motility of Jurkat cells was assayed using: (2) the percentage of motile cells (%); (3) the average migration speed (V) defined by the ratio of the accumulated migration distance (d_{acc}) to the time tracked (Δt); (4) the persistence of the migration track defined by the ratio of the net displacement (d_{net}) to the accumulated migration distance (d_{acc}), and (5) Chemotaxis Index (CI) defined by the ratio of the average distance travelled by the motile cells in the direction of chemokine gradient (d_{dir}) relative to the accumulated distance (d_{acc}) travelled by the motile cells[64].

$$\%motile = \frac{n_{cells\ (V<1\ \mu m/min)}}{n_{cells}} x100 \qquad \text{(eq. 1.2)}$$

$$V = \frac{d_{acc}}{\Delta t} \qquad \text{(eq. 1.3)}$$

$$Persistence = \frac{d_{net}}{d_{acc}} \qquad \text{(eq. 1.4)}$$

$$CI = \frac{d_{dir}}{d_{acc}} \qquad \text{(eq. 1.5)}$$

Each experiment was repeated at least 3 times, and migration parameters were calculated for each experiment independently. Two-tailed unpaired student's *t*-test was applied for statistical comparison of the data between different conditions (*$p < 0.05$; **$p < 0.01$; ***$p < 0.001$). The experiments with more than two conditions were analyzed using one-way ANOVA followed by *post hoc* two-tailed unpaired student's *t*-test with Bonferroni correction for pairwise comparison. The cases where parameters showed $p < 0.05$ were considered significantly different while those cases with $p > 0.05$ were considered not significant (n.s.).

Finite element modeling

Gradient formation in flow-free chambers was simulated using the Transport of Diluted Species Module in COMSOL (Stockholm, Switzerland) to guide the design of the gradient

chamber geometry. First, the flow-free chambers were generated as a rectangular solid with different aspect ratios. Inlet and outlet channels were represented by partitions along both sides of the chamber that defines regions with constant concentration. Boundary conditions were set along the partition surfaces to represent the sink and the source, respectively (C=0 and C=1; **Figure 1.3a**). Chambers were meshed with tetrahedral elements using the same mesh density (the maximum element size was 42 μm). Simulated concentration gradients were obtained along a line that traversed the chamber length on the bottom surface, representing the concentration gradient experienced by cells seeded onto the glass/fibronectin substrate in the flow-free gradient chamber.

Results

Understanding gradient generation in a flow-free microfluidic system through numerical simulation

Simulation of the concentration gradients generated in flow-free chambers revealed the formation of both vertical and horizontal gradients as the source and the sink surfaces were located only at the top of the gradient chambers. Cells seeded on the bottom surface of the gradient chamber are subject to gradients from both vertical and horizontal diffusion. The relative importance of the vertical gradient increased as the aspect ratio of the chambers (i.e. width/height) decreased. Vertical gradients created a decreasing concentration at the source side (C<1), and an increasing concentration at the sink side (C>0) (**Figure 1.3a**). Consequently, as the aspect ratio of the chamber decreases, the concentration gradient on the cells became shallower while maintaining the same average concentration. For example, in the gradient chambers with an aspect ratio of 1, the ideal normalized concentration gradient between C=1 and C=0 at the top surface became flatter, being C=0.59 at the source side and C=0.41 at the

sink side of the bottom surface. An acceptable range of concentration change, where the

gradient does not vary more than 5% from the ideal linear gradient at the bottom surface of the

gradient chamber (e.g. being C=0.96 and C=0.04 at source and sink respectively) was achieved

through an aspect ratio of 5 **(Figure 1.3c)**. Thus, a flow-free chamber, which was able to

produce a narrow gradient over 1500 μm in length, limited the height of the chamber to 300

μm. The concentration of the soluble factors used in the system should not have any effect

neither on the time scale for the gradient generation nor on the steady-state gradient profile

based on equation 1. Therefore, the considerations above expressed in normalized values

would be valid for different experimental conditions.

(a) Uniform Concentration, Horizontal Gradient, Vertical Gradient, x, y, z; C = 0, C = 1, w = 1500 µm, t = 1500 µm, h = variable

(b) Aspect Ratio (AR), Simulation; AR=1, AR=1.5, AR=3, AR=5, AR=10

(c) Steady-State Concentration Gradients on the Bottom Surface; Normalized Concentration vs Distance (µm); AR=1, AR=3/2, AR=3, AR=5, AR=10

(d) 0 min, 10 min, 20 min, 30 min; Experiment — FITC-dextran, Fluoro-Ruby; Simulation; 500 µm

(e) Red Flourescence Gradient Establishment; Green Fluorescence Gradient Establishment; Simulation of Gradient Establishment; Comparison of Experiment and Simulation; Normalized Fluorescence Intensity vs Normalized Distance; 0 min, 10 min, 20 min, 30 min; Simulation, Experiment

(f) Narrow Chamber (w = 1.5 mm); Wide Chamber (w = 2.5 mm); Fluoro-Ruby, FITC-dextran; 5 min, 10 min, 15 min, 20 min, 25 min, 30 min, 35 min, 40 min, 45 min, 50 min, 55 min, 60 min, 65 min, 70 min, 75 min; 500 µm

(g) 0 min, 30 min, 60 min, 90 min, 120 min, 150 min; 300 µm

23

Figure 1. 3. Generation of singular and dual competing concentration gradients in flow-free microfluidic chambers through coupled experimental and computational approaches. **(a)** A 3D model of gradient chamber with its dimensions and the boundary conditions used in simulations. **(b)** Results of simulations for controlling aspect ratios, which influences the gradients in the chambers. As the aspect ratio decreases, vertical concentration gradients begin to dominate the system. **(c)** Concentration gradients measured at the bottom surface of the gradient chambers with controlled aspect ratios. As the aspect ratio decreases, the steepness of the gradients at the bottom surface of the gradient chamber decreases while maintaining the same average concentration. **(d)** Comparison of the experimental gradient generation and the simulation. The narrow gradient chamber was filled with FITC-Dextran (MW: 10,000) in half and Fluoro-ruby (MW: 10,000) in the other half for faster generation of combinatorial gradients. Time-lapse images were captured every 10 minutes from both channels during the experimental gradient generation. **(e)** Comparison of the experiments and the simulations for the generation of transient and steady-state concentration gradient profiles. **(f)** Generation of linear concentration gradients across the flow-free gradient chambers without using the fast gradient generation technique. Unlike Figure 1.3d, here chambers were first filled with Fluoro-ruby and FITC-Dextran was introduced later. The time required for the establishment of steady-state gradients is 4 times longer as the fluorescent reporters should diffuse through the entire gradient chambers. **(g)** Long-term observation of the linear concentration gradients in device with seeded cells. The concentration gradient was continuously monitored during the cell tracking experiments to confirm that the concentration gradients were within the specified range.

Experimental concentration gradient generation

To demonstrate the generation of steady-state combinatorial concentration gradients in our flow-free gradient chambers, we introduced 50 µM of Fluoro-ruby (MW=10,000) to the flow channel on the right-hand side and filled all of the gradient chambers. We then introduced 50 µM of FITC-Dextran (MW=10,000) into the left flow channel and manually increased pressure on the left flow channel until the Fluoro-ruby went back to the middle region of the chamber for equal filling of the two fluorophores in the chambers **(Figure 1.3d, t=0)**. Syringes were then connected to a double syringe pump to deliver both fluorescent reporters at a controlled volumetric flow rate of 0.2 µL/min. This flow rate continuously replenished the solution at the boundary regions as the fluorophores diffused across the flow-free gradient chambers. The time required for the formation of the steady-state gradient is defined as:

$$t = \frac{L^2}{2D}$$

(eq. 1.6)

24

where L is the diffusion length and the D is the diffusion coefficient of the fluorophores. This approach allowed us to create combinatorial gradients and to reduce the time needed to equilibrate the gradient solely from the boundary sources by 75%. By using the diffusion coefficient for the 10 kDA FITC-Dextran of 1.33 x 10^{-6} cm^2/s [65] the time required for the establishment of a linear gradients was calculated to be ~ 35 min for the narrow chamber and ~ 98 min for the wide chamber. The steady-state gradient we found using fluorescent reporters was similar to the simulated gradients **(Figure 1.3d,e,f)**. In the cell migration experiments, we tracked the stability of the chemokine gradient by adding 50 µM Fluoro-ruby to the chemokine solution in each experiment. Tracking cells and observing the chemokine gradient is important since the initial characterization of the gradient does not guarantee that these conditions will be maintained throughout each cell migration experiment.

One challenge with our approach was the bonding of the membrane filter to PDMS layers since non-uniform attachment or partial clogging could cause unstable concentration gradients. We found APTES-mediated membrane integration required a shorter time to fabricate (<30 minutes for complete assembly), had a higher success rate, and generated a stronger bond[66]. We tried another membrane integration technique that uses a thin PDMS prepolymer film as an intermediate adhesive layer[67,68]; however, the functional surface area of the PC membrane filter was frequently reduced, possibly due to the wetting. This approach caused partial clogging of the membrane by the PDMS prepolymer **(Appendix 1.2)**.

Finally, although this study mainly aimed to investigate cell motility at a population level, we confirmed the suitability of our microfluidic flow-free concentration gradient

generation system combined with high resolution confocal microscopy for single cell migration studies **(Appendix 1.3)**.

Jurkat cell chemotaxis

Increasing Substrate Fibronectin Concentrations Promote Random Cell Motility but Not Chemotaxis: We used our microfluidic approach to understand the effects of fibronectin concentration on the Jurkat cell motility. To do this, we coated the microfluidic gradient chambers with 0, 25, 500, and 1000 µg/mL concentration of fibronectin and assessed the effect of substrate fibronectin concentration on random cell migration and chemotaxis. We referred to 25 µg/mL and 1000 µg/mL as low substrate fibronectin concentration and high substrate fibronectin concentration, respectively. For cell migration experiments, we introduced cells labeled with CellTracker Green BODIPY dye to fibronectin-coated gradient chambers at a density of 300,000 cells/mL and placed the microfluidic system in a stage-top environmental chamber immediately after the seeding of cells. To establish the chemokine gradient over Jurkat cells, we introduced 100 nM CXCL12 to the inlet of the flow channels **(Figure 1.3g)**, creating a concentration gradient with the slope of 66.6 nM/mm (plot of stable linear concentration gradient over time shown in **Appendix 1.4**). We first examined the effect of substrate fibronectin concentration on the random migration of Jurkat cells in the absence of a chemokine. As the fibronectin concentration used to coat the gradient chambers was increased from 0 to 1000 µg/mL, the average migration speed as well as the percentage of motile cells increased significantly (p=2.21×10^{-6} for migration speed and p=1.13×10^{-9} for the percent motility) while the overall Jurkat cell motility remained random **(Figure 1.4a-c)**. Coating the microfluidic chambers with high fibronectin concentrations led to 8-fold increase in the

percentage of motile cells compared to the cells migrating in non-coated chambers. In addition, there was 2-fold increase in the average velocity of the motile cells when the substrate was coated at a high fibronectin concentration. Increasing surface fibronectin concentration gradually increased both the percentage of motile cells and their average velocity, however, this trend was disrupted once the chemokine was introduced. On the substrates coated with a low fibronectin concentration (25 µg/mL), addition uniform 100nM CXCL12 background significantly increased the percentage of motile cells compared to the control lacking CXCL12 (p=0.008). We then established a linear CXCL12 concentration gradient ranging from 0 to 100 nM across the microchannel. The presence of a concentration gradient further increased cell motility compared with a uniform CXCL12 concentration (p=0.004) **(Figure 1.4d)**. A statistically significant difference was not found for the percentage of motile cells and their average velocity between low and high fibronectin concentration when a chemokine gradient was present **(Figure 1.4e)**. These results show that neither the fraction of motile cells nor their average migration speed are affected by the fibronectin concentration when CXCL12 chemokine gradient exists. In other words, while increasing fibronectin concentration promotes random cell migration, it does not increase the cell motility during chemotaxis.
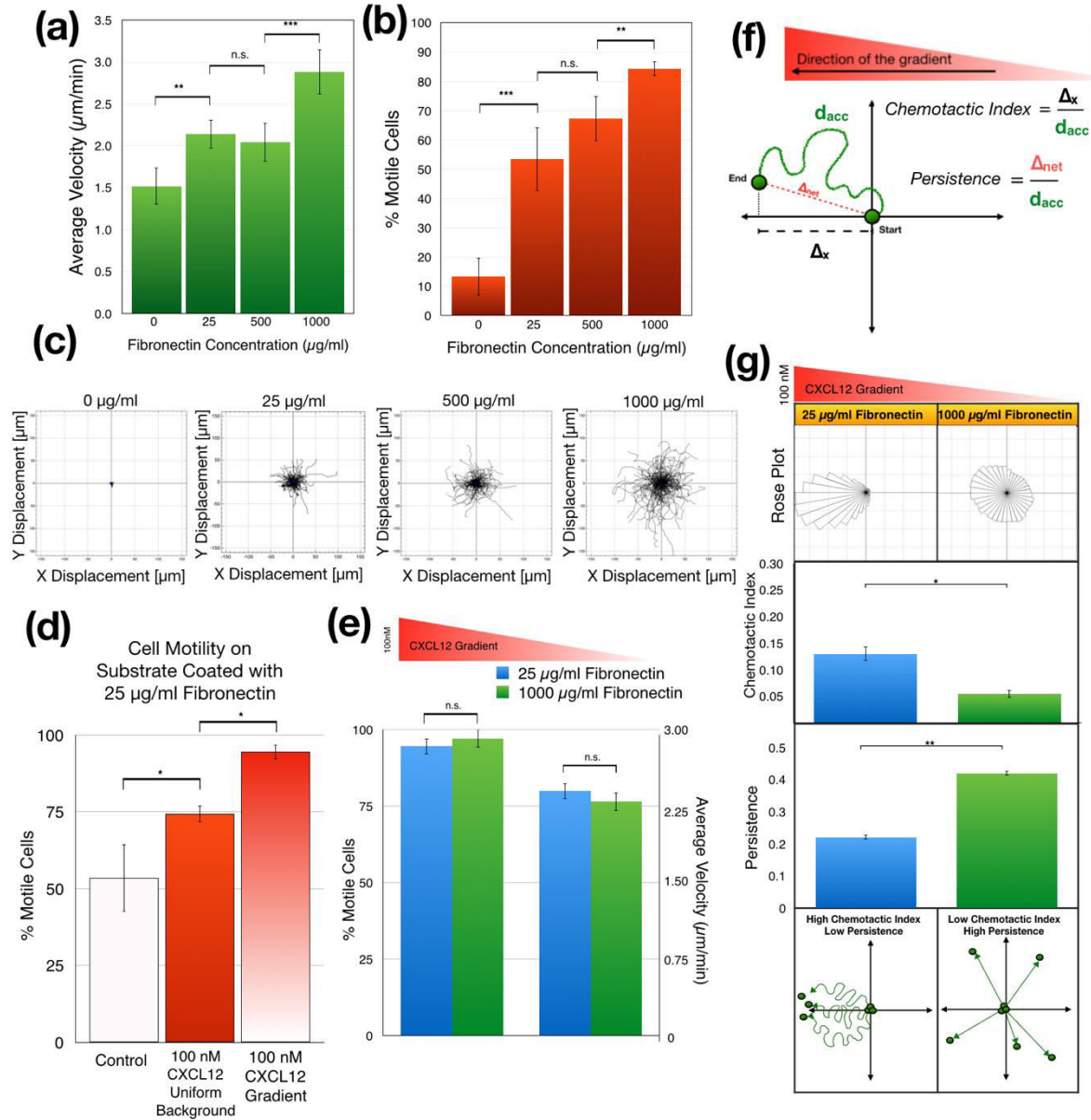
Figure 1. 4. The effect of fibronectin concentration on Jurkat cell chemotaxis. **(a)** During random motion, the average speed of the migrating cells increases as the fibronectin concentration increases ($p<0.0001$ by one-way ANOVA, **$p<0.01$, ***$p<0.001$ by *post hoc* two-tailed unpaired student's *t*-test with Bonferroni correction). **(b)** Also, during random motion, the percentage of motile cells increases as the fibronectin concentration increases ($p<0.0001$ by one-way ANOVA, , **$p<0.01$, ***$p<0.001$ by *post hoc* two-tailed unpaired student's *t*-test with Bonferroni correction). **(c)** Spider motility plots of randomly migrating Jurkat cells in microchambers coated with 0, 25, 500, and 1000 µg/mL of fibronectin, respectively. As the fibronectin concentration increases, cells spread more while maintaining their mass center at the origin (location of final mass center is shown as a blue dot). **(d)** Comparison of the percentage of motile cells in culture medium, in uniform 100 nM CXCL12 background, and in 100 nM CXCL12 gradient in the microfluidic chambers coated with 25 µg/mL of fibronectin. ($p<0.0001$ by one-way ANOVA, *$p<0.05$ by *post hoc* two-tailed unpaired student's *t*-test with Bonferroni correction). **(e)** In CXCL12 gradients, the motility of the cells appears to be independent of fibronectin concentration. Unlike Figure 1.4c and 4d, the change in fibronectin concentrations does not seem to alter the percentage of the motile cells nor the

28

average migration speed when there is a chemokine gradient (p>0.05 by two-tailed unpaired student's *t*-test). **(f)** Schematic indicating our quantitative analysis approach for Jurkat cell motility in CXCL12 concentration gradient. **(g)** Jurkat cell chemotaxis in the gradient chamber coated with 25 µg/mL (referred to here as low concentration) and 1000 µg/mL (referred to here as high concentration) fibronectin. As the fibronectin concentration increases, the chemotactic index decreases (shown in the rose plots at the top) while the persistence increases (shown in the bar graphs at the middle). At high fibronectin concentrations Jurkat cells tend to migrate in a specific direction (high persistence), but this direction becomes independent of the direction of the chemokine gradient (low chemotactic index). This observation has been represented in the bottom schematics (**p<0.01, *p<0.05 by two-tailed unpaired student's *t*-test). Data are presented as mean ± SD.

Increasing Substrate Fibronectin Concentration Creates Random Cell Migration Background during Chemotaxis: To better understand the role of the CXCL12 gradient and substrate fibronectin concentration in regulating chemotaxis, we tracked individual Jurkat cells seeded in microfluidic gradient chambers coated with either high or low fibronectin concentration as they migrated in a CXCL12 gradient, which ranged from 0 to 100 nM across the gradient chamber (gradient slope is 66.6 nM/mm). We calculated the CI and persistence for motile Jurkat cells using the tracking data. We found that the high surface fibronectin concentration significantly reduced the CI of the Jurkat cells (p=0.014), increasing their random motion and decreasing their directedness as measured by CI **(Figure 1.4f)**. At high fibronectin concentrations Jurkat cells migrated more uniformly in all directions regardless of the direction of the chemokine gradient **(Figure 1.4g, top left)**. Interestingly, while the CI of their motion towards the CXCL12 gradient decreased, their persistence significantly increased with increasing fibronectin concentration (p=0.045) **(Figure 1.4g, middle)**. In other words, as the surface fibronectin concentration increased, Jurkat cells migrated more persistently in random directions independent of cues from the chemokine gradient **(Figure 1.4g, bottom)**.

Jurkat Cells Migrate Faster in Shallower CXCL12 Gradient: To assess cellular responses to controlled gradient slopes, we compared chemotactic behaviors of Jurkat cells in narrow and wide chambers where we created 2 independent chemokine gradients with different gradient steepness but with the same average chemokine concentration. As previously described, we filled the source channel with 100 nM CXCL12 diluted in cell culture medium while the culture medium alone was supplied to the sink channel to create gradients of CXCL12 with different slopes simultaneously (66.6 nM/mm in the narrow chamber and 40 nM/mm in the wide chamber). We tracked cells in both gradient chambers in parallel and calculated their migration parameters **(Figure 1.5a)**. We coated gradient chambers with 25 μg/mL fibronectin to enable Jurkat cell migration and allow them to maintain a directional response to a chemokine gradient. The slope of the gradient did not significantly alter the percentage of motile cells as more than 90% of cells were motile in both chambers. As expected, CI was also similar in both chambers. On the other hand, we noted substantial increase in the persistence in a shallow CXCL12 gradient, but this increase was not significant **(Figure 1.5a)**. Surprisingly, we found the average migration speed of the motile Jurkat cells increased significantly when the slope of

CXCL12 gradient was lowered to 40 nM/mm (p=0.008).
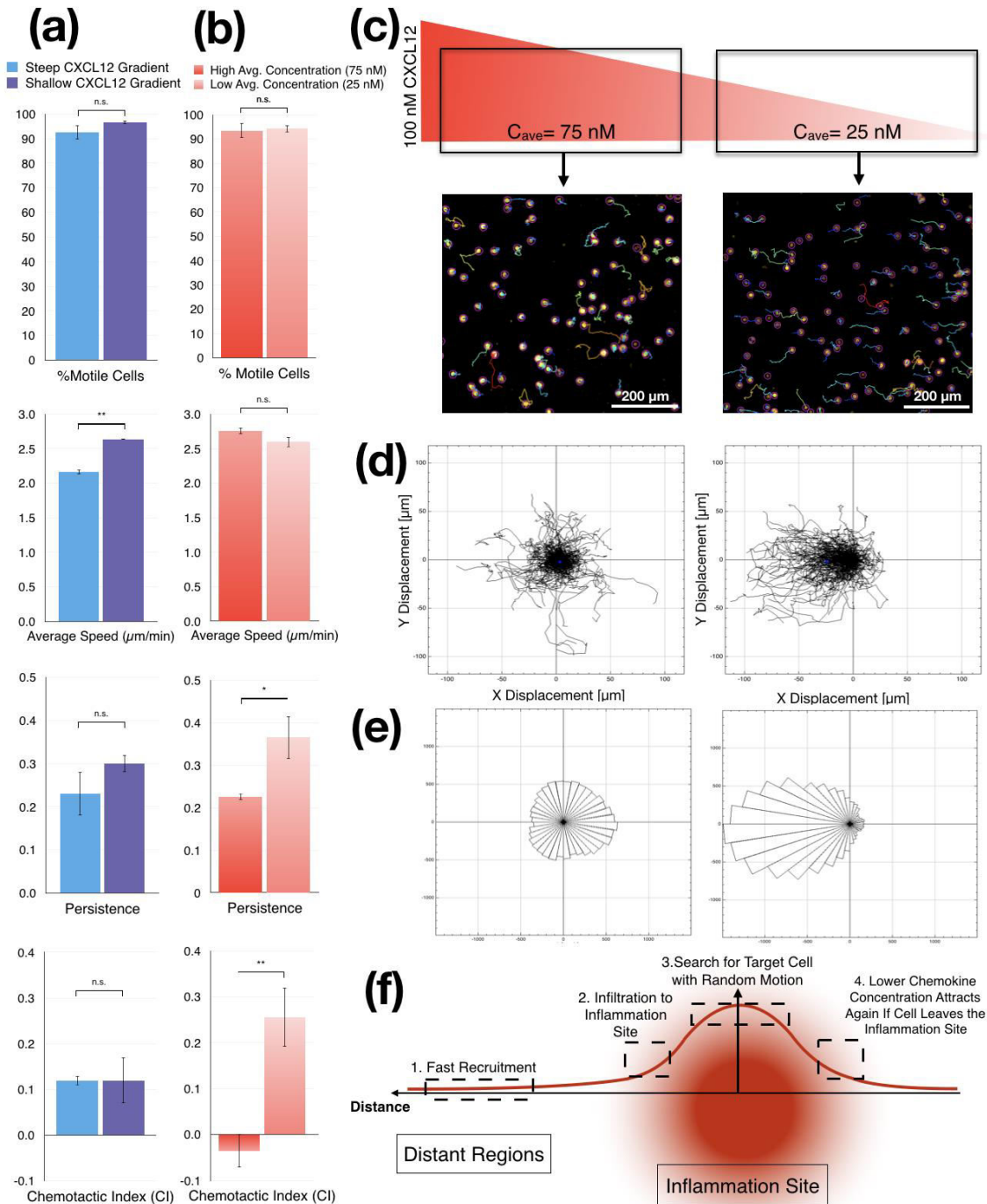
Figure 1. 5. Chemotaxis of Jurkat cells in different CXCL12 gradient modalities (a) Quantitative analysis of cell movement shows differences between migration parameters from cells that migrate in shallow CXCL12 gradient (wide chamber, 40 nM/mm) and steep CXCL12 gradient (narrow chamber, 66 nM/mm). Although the increased steepness does not alter the motile cell ratio and chemotactic index, it slows the average speed and persistence of the migration (**p<0.01 by two-tailed unpaired student's *t*-

test). **(b)** Quantitative analysis shows that average CXCL12 concentration strongly affects the persistence and the chemotactic index of the migrating Jurkat cells, while it does not alter the percentage of motile cells or the average speed of the migrating cells (**p<0.01, *p<0.05 by two-tailed unpaired student's *t*-test). **(c)** We examine our wide gradient chamber by dividing it into two regions with different average chemokine concentrations while maintaining the same gradient steepness. While the region on the left has an average concentration of 75 nM of CXCL12 concentration, the region on the right has an average of 25 nM of CXCL12 concentration. **(d)** Spider motility plots of the Jurkat cell chemotaxis in two sub-regions of the wide gradient chamber. While the cells at the higher average CXCL12 concentration (left) appear to be migrating randomly, the ones in the lower average CXCL12 concentration (right) appear to migrate toward the higher concentration of CXCL12 in the gradient. **(e)** Rose plots show the difference between two subregions of the wide gradient chamber in terms of the spreading of the Jurkat cells. Although, Jurkat cells which are spread equally in all the directions at a high average CXCL12 concentration, show a random migration pattern, they migrated towards the CXCL12 gradient in the right side of the chamber. **(f)** Schematics of a potential description of the accumulation and random motility of immune cells in the inflammation zone related to high chemokine concentrations that may function as a chemical trap. Data are presented as mean ± SD.

Jurkat Cells Migrate Randomly in CXCL12 Gradients with High Average Concentration: To test whether Jurkat cells were responding to cues in the gradient or merely differing amounts of CXCL12, we investigated the migratory response of Jurkat cells in the same chamber but at different average concentrations of CXCL12. In the wide gradient chamber, we tracked the Jurkat cells closer to the source channel and the ones closer to the sink channel separately, based on their initial positions within the chamber. We then compared the migratory behavior of Jurkat cells close to the source channel with cells that were closer to the sink channel. Cells in both subgroups had the same gradient slope (40 nM/mm) as the gradient was linear across the chamber, but the first group was in the region of the chamber where the average CXCL12 concentration was 75 nM (high average concentration), and the other subgroup was in the region of the chamber where the average CXCL12 concentration was 25 nM (low average concentration). The change in the average CXCL12 concentration did not cause a significant alteration in the percentage or the average migration speed of the motile cells **(Figure 1.5b)**. This result was similar to the results presented above with the different surface fibronectin

concentrations **(Figure 1.5b vs. Figure 1.4e)**. However, the chemotactic behaviors of the Jurkat

cells in different subgroups were significantly different **(Figure 1.5c)**. While Jurkat cells in the

low average CXCL12 concentration were migrating towards the CXCL12 gradient with high

persistence and CI, those in the high average CXCL12 concentration migrated away from the

CXCL12 concentration with significantly lower persistence (p=0.014) and CI (0.0018). This

finding suggested a migratory behavior closer to the random motion observed with uniform

CXCL12 background **(Figure 1.5c,d)**. Nonetheless, substantially higher numbers of Jurkat cells

were motile, showing that cells still distinguished between a uniform chemokine background

and a chemokine gradient. This suggests that CXCL12 saturate chemotactic responses of Jurkat

cells at concentrations above 75 nM in a manner similar to the saturation of T cells responses to

CCL19 or CCL21 concentrations above 100 nM[69,70]. On the other end of the spectrum, using a

different microfluidic system, Jurkat cells were shown have significantly reduced chemotactic

response to CCL19 gradient when the CCL19 concentration was reduced from 100 nM to 10 nM

while preserving their average migration speed[71] in a way similar to our chemotaxis data.

Overall, these observations and our results suggest that both the concentration gradient and

the average concentration of the chemokines directs the chemotactic behavior of different

immune cells and that both Jurkat cells and T cells share saturable motility responses to

chemotactic cues albeit to different chemokines.

T cell chemotaxis

MitoFAP CD8+ T cell staining using Hoescht 33342: Hoescht 33342 is a frequently used

fluorescent dye to stain the nucleus of the cells to facilitate cell tracking. Although in the

literature there are plenty of examples of using Hoescht 33342 for the staining of primary

mammalian cells, we realized that this dye was cytotoxic for T cells as a result of the viability experiments we conducted using Trypan blue **(Figure 1.6a)**.

Therefore, we conducted viability experiments using different concentrations of Hoescht 33342 and imaging the cells with different exposure times to optimize the cell staining protocol before conducting the chemotaxis experiments. Our results confirmed that the recommended concentration of Hoescht 33342 (1:2000 dilution which equals to 10 μM) was indeed cytotoxic for the T cells. Therefore, we reduced the concentration of Hoescht 33342 gradually down to 400 nM. Hoescht 33342 staining at such a low concentration was preventing the cells from dying but it was also significantly increasing the exposure time for obtaining fluorescent images. Since this would also increase the time interval between two consecutive images, which, in turn, would make the cell tracking harder, we conducted optimization experiments by staining cells with different Hoescht 33342 concentrations and imaging them approximately 30 minutes after staining. Our results indicated that the 2 μM concentration of Hoescht 33342 (which equals to 1:10,000 dilution) was enough to prevent cell death while maintaining reasonably short exposure time (around 50 ms). For this reason, we used this concentration of Hoescht 33342 in the following chemotaxis experiments that we conducted with T cells **(Figure 1.6b)**.
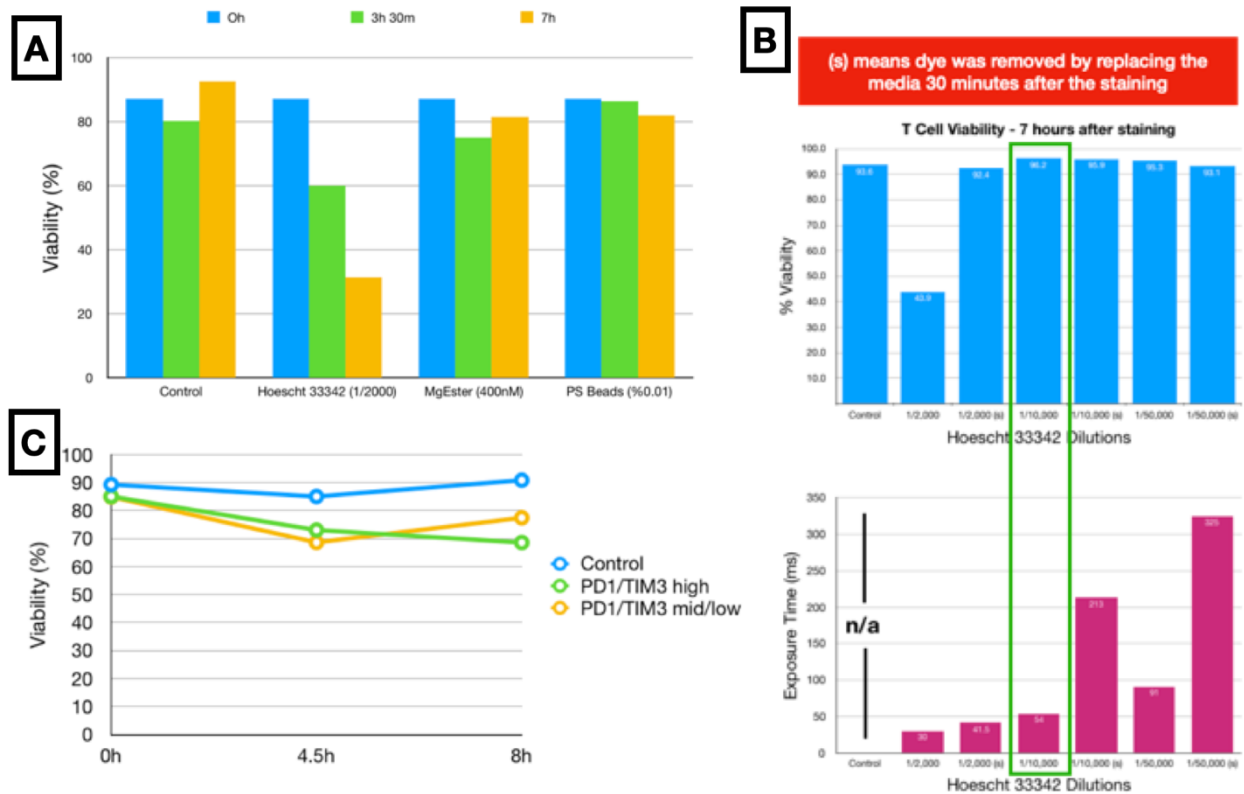
Figure 1. 6. Viability of T cells under experimental conditions. **(a)** Initial viability experiments conducted with murine CD8+ T cells for the assessment of the reason for low viability after 7 hours of in vitro culturing. Results clearly show that the Hoescht 33342 staining as the reason of low viability. **(b)** Staining optimization of murine CD8+ T cells with Hoescht 33342. 1:10,000 dilution of Hoescht 33342 (which corresponds to 2 µM) was found to be the lowest dilution ratio that can be used to stain cells without any cytotoxic effect while allowing the cell tracking with low exposure times. **(c)** The viability of the tumor infiltrating lymphocytes (TILs) during the experimental period determined via trypan blue viability assay. We observed that the viability of the cells is not decreased below 70% throughout the experiment period.

Tumor Infiltrating lymphocytes in vitro viability: In this set of experiments, we used primary

murine CD8+ T cells, also known as tumor infiltrating lymphocytes (TILs), obtained from mice

with B16 melanoma model. Prior to chemotaxis experiments, T cells are sorted based on their

PD1/TIM3 expression using fluorescence-activated cell sorting (FACS). As a control group, we

used in-vitro activated wild type murine CD8+ T cells. Before conducting the chemotaxis

experiments, we first assessed the viability of the cells inside the microfluidic chambers as there

was no previous study in the literature that used these cells in a microfluidic system. After staining cells with Hoescht 33342 with previously optimized concentration for tracking, we conducted cell viability assay using trypan blue. Based on the assay results, we confirmed that cells maintain at least 70% viability over the course of 8 hours after staining and being cultured in vitro **(Figure 1.6c)**. We repeated this assay every time before using the cells with the microfluidic system to ensure that the motility behavior of the cells is not the result of low viability. In the cases where the viability was less then 70%, we did not use the cells in the chemotaxis experiments.

Motility of the MitoFAP CD8+ T cells: In these experiments, we used primary murine CD8+ T cells that contain genetically encoded fluorogen-activating protein (FAP) which targets their mitochondria and specifically damages it upon illumination with infrared light. In order to prevent cell death due to FAP this technique was previously optimized, and it was shown that the illumination of the cells after transduction only gradually decreases the mitochondrial activity without actually killing them. Using this technique, we aimed to investigate the role of mitochondria in T cell motility within chemokine gradients. We conducted these experiments with or without chemokine gradients to observe the base random migration of the cells as well as their chemotactic behavior. We also illuminated the cells for 30 minutes and 1-hour long durations to assess the effects of dose-dependent decrease in mitochondrial function. Our initial results imply that the lower mitochondrial activity does not decrease the percentage of motile cells neither in the random migration nor in the chemotaxis settings. However, the average velocity of the motile cells is decreasing in a dose-dependent manner in both of these conditions **(Figure 1.7)**. Similar to the percentage of the motile cells, the mitochondrial function

also did not affect the persistence of the cell migration neither in the random migration nor in

the chemotaxis within CCL3 gradient. Interestingly, the chemotactic index of the cells increased

in a dose-dependent manner upon the decrease of mitochondrial function, meaning that cells

were following the CCL3 gradient with higher affinity with the lack of mitochondrial function.

This rather surprising result led us to speculate that the main contribution of mitochondrial

activity to the T cell migration was through the promotion of random migration. We are

currently conducting more experiments by using a different chemokine, namely CXCL10, in

order to test if this phenomenon is chemokine dependent or not.
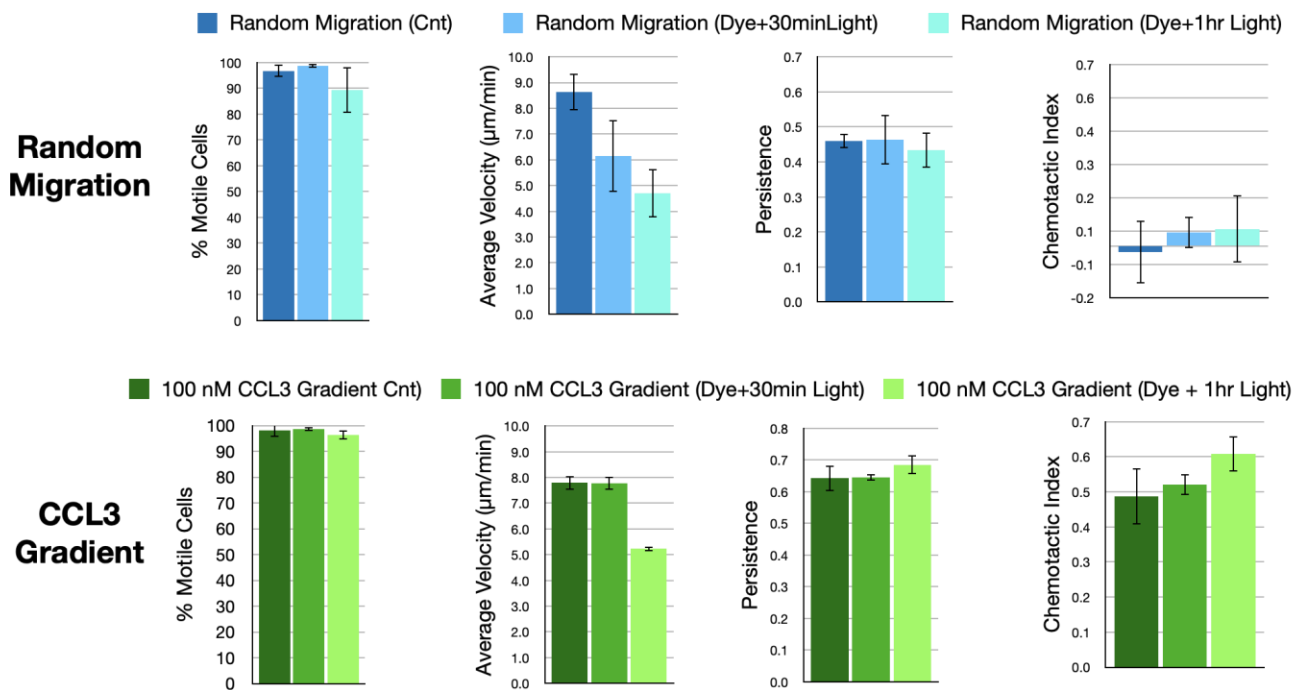
Figure 1. 7. Random migration and chemotaxis of CD8+ MitoFAP murine T cells in the microfluidic chambers. These initial results imply that the mitochondrial activity was essential for high migration velocity of the T cells. On the other hand, it also seems to diminish the ability of the T cells to follow CCL3 gradient, leading to lower chemotactic index.

Motility of the tumor infiltrating lymphocytes (TILs): High PD1 expression in CD8+ T cells are associated with decreased T cell function. In the tumor microenvironment, it was previously reported that the majority of T cells are expressing high levels of PD1. This is thought to be one of the major mechanisms of how the tumor cells evade immune surveillance. In order to test if PD1 expression has any significant role in the T cell motility, we recovered T cells from B16 mouse tumor model and sorted them based on their PD1 expression levels. Then, we conducted random migration and chemotaxis experiments using these cells in our microfluidic system. Our initial results imply that the lower percentage of the T cells are motile if they have high expression of PD1 compared to control T cells and the T cells with lower expression levels of PD1 during both random migration and chemotaxis in CCL3 gradient. Interestingly, the average velocity of the T cells with low PD1 expression is the highest even surpassing the control T cells while the average velocity of the T cells with high PD1 expression has the lowest average migration velocity in both of these conditions **(Figure 1.8)**. On the other hand, we observed that the persistence and chemotactic index of the T cells with high levels of PD1 expression is higher than the cells with low level of PD1 expression in the chemotaxis setting. These results imply that the while PD1 expression is crucial for increased T cell motility it also has negative effects on the chemotactic behavior of T cells. Similar to what we are doing with MitoFAP T cells, we are currently conducting further experiments using CXCL10 chemokine in order assess if these observed motility behaviors are independent of the chemokine type.
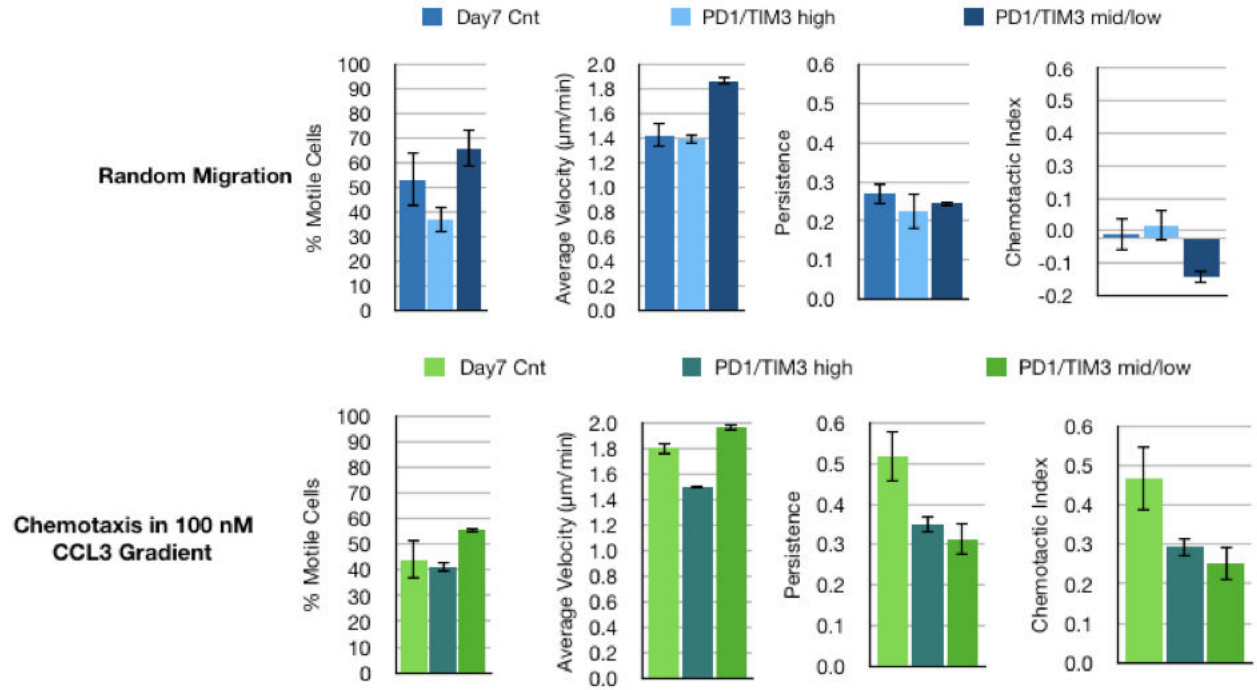
Figure 1. 8. Motility behavior of tumor infiltrating lymphocytes (TILs) within the microfluidic system with and without CCL3 chemokine gradient. TILs with high PD1 expression show lower levels of motility during random migration and chemotaxis. On the other hand, the persistence and the chemotactic index of these cells are relatively higher compared to TILs with low PD1 expression.

Discussion

The profile of the steady-state gradients within the microfluidic flow-free gradient

chambers is highly related to the aspect ratio of the chambers. If the profile is not taken into

account, the actual chemokine gradient presented to the cells in the chambers can be significantly

different from the boundary values defined at the flow channels. We generated steady-state

concentration gradients in these 3D-printed microfluidic chambers within 35 minutes using 10

kDa FITC-Dextran as a fluorescent probe. The diffusion coefficient of FITC-Dextran (D = 1.33 x

10^{-6} cm^2/s) is lower compared to the other fluorescence probes with similar molecular weight

(i.e. D = 4.34 x 10^{-6} cm^2/s for Alexa 488 (MW: 10,000)). Using these fluorescent probes, it is

possible to demonstrate the establishment of gradient in the same microfluidic system 3 to 4 times faster. However, we used a fluorescent probe with a lower diffusion coefficient to be conservative in showing that the steady-state concentration gradient of the actual chemokine was established when we started tracking the cells. It is essential for the functional regions of membrane to remain intact to maintain stable gradients over time. Since diffusion only occurs across a small portion of the membrane surface, partial or complete clogging of the membrane can result in unstable gradients[59,72]. Therefore, membrane clogging can critically limit applications in systems like ours where only a small region of a membrane is effectively used. For this reason, we tested multiple membrane processing techniques and found that APTES-mediated membrane integration was the most effective technique to create a strong bond without clogging **(Appendix 1.2)**.

CXCL12 and fibronectin independently regulate Jurkat cell motility. In a uniform concentration of 100 nM CXCL12 (no gradient) more Jurkat cells showed motility compared to controls lacking CXCL12. Interestingly, even more cells migrated in the gradient of 100 nM CXCL12 **(Figure 1.4d)**. Therefore, CXCL12 appears to have two distinct functions. First, uniform levels of CXCL12 activate cells to became motile. Second, a gradient of CXCL12 provide an additional cue for directional chemotactic response. A very similar gradual increase in the Jurkat motility was shown in the literature with uniform CCL2 background and CCL2 gradient using conventional Boyden chambers[73]. Although, we have shown that the fibronectin concentration can regulate the extent of random motility of the Jurkat cells, we did not see a significant difference in the percentage of motile cells or their average velocities with 100 nM CXCL12 gradient in chambers coated with low (25 µg/mL) or high fibronectin concentrations (1000 µg/mL) **(Figure 1.4a,b vs. Figure 1.4e)**. In a potentially similar manner, neutrophils and

in-vitro activated T cells have also been shown to have constant chemotaxis speeds regardless of the extracellular matrix concentration[74] or the type of chemokine[75] while having as much as two times higher average migration speed than Jurkat cells[76].

The addition to the chemokine gradient, the surface-bound fibronectin concentration also regulates the random motility as well as the chemotactic behavior of Jurkat cells. Jurkat cells within a chemokine gradient migrate in all directions with high persistence regardless of the direction of the chemokine gradient when fibronectin concentration is high, creating a migratory pattern similar to random migration **(Figure 1.4g)**. This finding parallels previous studies where the increased fibronectin concentration has also been reported to increase random migration in chemotactic cells[74,77]. On the other hand, in the very same chemokine gradient, cells that are seeded in gradient chambers coated with low fibronectin concentrations show opposite behavior by migrating in the direction of the chemokine gradient with high CI and low persistence. The decoupling of the Jurkat cell motility and directionality was previously shown as a result of PTEN-modulated actin polymerization[78]. These results suggest that both extracellular matrix (ECM) concentration and chemokine gradients in the cellular microenvironment regulate chemotactic responses of Jurkat cells in an interactive manner.

Distinctive migratory responses in different chemokine gradients suggest that chemokine gradients may regulate the spatial bounds of the immune response. During a local inflammation in a defined region in the body, immune cells are recruited rapidly to the inflammation site through the orchestration of chemokines released from the site of inflammation[79]. Since these chemokines diffuse in all directions in 3D, they create non-linear concentration gradients where the slope gradient is high at the regions proximal to the inflammation site and becomes shallower at the distant regions[80] **(Figure 1.5f)**. Therefore, immune cells that reside at the distant regions of

the body should initially sense these shallow chemokine gradients and respond by moving

rapidly toward the inflammation site[81] **(Figure 1.5f.1)**. Remarkably, first responders of the

immune system are recruited from distant regions to injury sites within hours[82]. Our

experimental data with Jurkat cells as a model cell line also show faster directional migration in

shallower CXCL12 gradient supporting this concept.

The rapid chemotactic response at shallower gradients, where differential receptor

occupancy across the cell membrane[83] would be expected to be less significant, might be

explained by an alternative chemotaxis concept[84]. After recruitment **(Figure 1.5f.2)**, activated

immune cells accumulate at the inflammation site[85] but require cell-cell contact to carry out their

effector function [86]. Thus, immune cells would need both a general attraction to the site of

inflammation but also would require specific cues that allows them to target specific cells within

the infected tissue. The strong chemotactic response that we have observed in this study at low

chemokine concentrations accompanied with a chemokinetic response at high chemokine

concentrations appears to support this two-stage scenario. One way to consider this is in a

"chase" and "search" mode where the response of the cells depends on the average concentration

of the chemoattractant. In "chase" mode, immune cells approach the inflammation site following

long-range directional cues from chemokine gradients. Once in proximity of infected cells,

immune cells respond to high concentrations of chemokines engage in a "search" mode, moving

rapidly but with low persistence, to reach their targets **(Figure 1.5f.3)**. If the immune cell leaves

the infected tissue as a result of this random motion, the average chemokine concentration

decreases again which would again start the migration through the chemokine gradient, resulting

in the cells returning to the inflammation site **(Figure 1.5f.4)**. These dual modes of chemokine

functions would allow immune cells to accumulate within the infected tissues without blocking

them from performing a local search for their infected targets with highly motile random migration. Our experimental data with Jurkat cells as a model for T cells mimics these motility behaviors as shown with quantified live cell tracking analysis.

Conclusion

We developed a flow-free gradient chamber within a microfluidic system that enables the generation and maintenance of single or combinatorial concentration gradients. The wide gradient chamber of our enhanced system allows population-wide cell migration assays with single cell sensitivity using high resolution microscopy. We constructed the system using additive manufacturing and replication molding techniques, demonstrating the feasibility and speed of fabrication, even in the absence of specialized microfabrication equipment and sophisticated facilities. The resulting spatiotemporally controlled fluidic environments were used to induce cellular responses to different gradient profiles in chambers with different aspect ratios. The transient and steady-state gradient profiles obtained in experiments agreed with theoretical predictions and simulation results.

Also, in applying the flow-free gradients of CXCL12, we demonstrated Jurkat cell chemotaxis in response to different concentration gradients and the coupled functionality of these gradients with surface fibronectin concentration. Our analysis of Jurkat cell chemotaxis to CXCL12 gradients in the context of different fibronectin concentrations demonstrated that fibronectin increased the percentage of motile cells and the average speed of random cell motion but did not alter these properties when there was a chemokine gradient. We also found that fibronectin significantly altered the CI and the persistence of the motile cells during chemotaxis. This system also allowed us to show that high concentrations of CXCL12 saturated

the Jurkat cells, resulting in random migration even in the context of a chemokine gradient. The

dual mode of response to chemokines proposed in our microfluidic experiments mimics the

overall immune cell motility *in vivo*. Our novel technique facilitates further studies of the

relationship between different cellular microenvironments and chemotactic responses, which

are relevant to a wide range of applications from immunotherapy to microfluidics technologies.

Chapter 2: High-throughput Mechanostimulation of Drosophila Melanogaster Embryos Using a Novel Microfluidic Device

Introduction

An emerging theory in embryonic development is that gene expression and mechanical

forces coordinate development in a reciprocal interplay.[87-89] It is well established that certain

developmental genes generate mechanical strain that leads to tissue-specific morphogenetic

movement. For example, in *Drosophila*, the transcription factor *twist* controls a sequence of

events that lead to the apical constriction of ventral cells, changing their shape from columnar

to wedge, which collapses the ventral furrow inwards and initiates mesoderm invagination.[90,91]

The ventral furrow does not form properly in embryos mutant in *twist*.[92]

Growing evidence suggests that exogenous mechanical forces can be sufficient to

directly activate certain genes[89,93]. For example, although *twist* is normally expressed

specifically in ventral cells of the *Drosophila* embryo, mechanical compression has been

sufficient to trigger ectopic expression of *twist*.[94] The direct mechanical induction of *twist* has been observed by coverslip actuation with piezoelectrics,[94] femtosecond laser pulses,[95] magnetic tweezers,[96] and needle indentation.[97,98] However, the mechanism of mechanotransduction remains unknown. The *Drosophila twist* pathway could be a powerful system to investigate mechanotransduction, but these approaches are labor-intensive, require manual alignment, and process only a few embryos at a time, precluding many biological assays.

One promising approach for manipulating hundreds of embryos simultaneously is microfluidics. Microfluidic approaches have led to semi-automated tools to sort[99], align,[100,101] immobilize,[102,103] image,[104] and recover processed embryos with minimal intervention. In particular, fabrication using polydimethylsiloxane (PDMS) has many advantages: elasticity and high oxygen-permeability facilitate embryo manipulation; low autofluorescence coupled with transparency in the visible spectrum enable high-resolution fluorescence microscopy. Microfluidic systems have provided spatiotemporal precision for many whole-embryo interventions, including thermal,[105] chemical,[106,107] acoustic,[108-110] geometric shape,[111,112] and RNAi.[113,114] Microfluidics could be a powerful approach to study mechanotransduction at a high throughput scale, but mechanical interventions have been limited to smaller cellular systems.[115-118] Microfluidic mechanical interventions that examine multicellular embryos have limited functionality,[119,120] especially in combining immobilization, alignment, and scalability.[103,121]

Here, we describe a microfluidic device to apply the automation and precision of microfluidics to whole embryo mechanotransduction **(Figure 2.1)**. This device can automatically

align, immobilize, and compress hundreds of *Drosophila* embryos. It precisely applies a controlled uniaxial strain using pneumatically actuated flexible sidewalls. This flexibility compensates for the variation in size among embryos, creating a custom width that applies a strain more consistent than conventional techniques. Fabrication on a coverslip allows for live imaging during and after mechanical stimulation, and embryos can be recovered for post-analysis. We describe a method for ultra-thick photolithography, derive an analytical model that predicts sidewall deflection, and discuss parametric calibration to construct future microfluidic devices. We show this device maintains embryo development, does not induce anoxia, and can apply mechanical stimulation at a high-throughput scale with micrometer accuracy. Using this micromechanics approach, we map and quantify the dose-dependent and duration-dependent mechanical induction of *twist* during early *Drosophila* development.
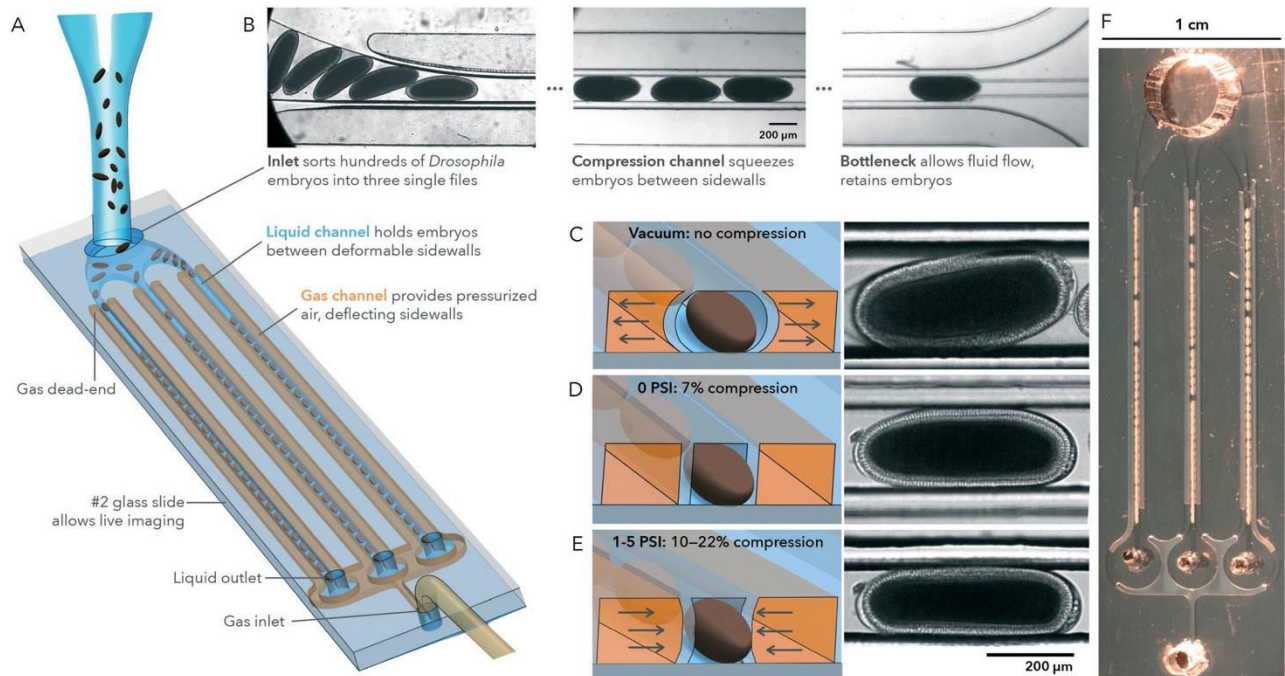
Figure 2. 1. A microfluidic device for high-throughput immobilization, imaging, compression, and recovery of *Drosophila* embryos. **(a)** Illustration of embryos loading into a microfluid device. PDMS channels form two interlaced systems: a liquid channel (blue) carries embryos suspended in buffer. A closed gas channel (orange) carries pressurized air. **(b)** Transmitted light micrographs of embryos in the channel. A narrowing inlet aligns embryos into a single file. The main portion of the channel compresses embryos between two deformable walls. Channels terminate in a bottleneck, allowing fluid flow while retaining embryos. **(c–e)** Illustrations and micrographs of sidewall deflection. **(e)** Under vacuum, channel walls expand to load embryos and function as a control condition. **(d)** At rest, the channel is narrower than the embryo, providing immobilization and compression. **(e)** Pressurizing the surrounding chamber deflects the channel walls inwards, compressing the embryos further. **(f)** Photograph of the device with embryos.

Material and Methods

Microfluidic device fabrication

High aspect-ratio structures remain a fabrication challenge in soft lithography.[122] This challenge is exacerbated for continuous microscale features that cover a mesoscale footprint, such as PDMS sidewalls tens of μm thin, over 200 μm high, and 20 000 μm long. These thin, deep, and trench-like features lead to nonuniform developer exposure across the pattern, and small errors in geometry result in failure of fabrication. We fabricated devices using

photolithography and PDMS replica molding[123] with modifications for thick structures (film height >100 μm) with high aspect ratio (AR >5) features.

Pouring ultra-thick photoresist: Prior to spin coating, silicon wafers (Si) were cleaned with acetone, isopropyl alcohol (IPA), and deionized water (DI), followed by a dehydration bake at 200 °C for 2 hours. Prior to pouring, ultra-thick photoresist (SU8-2100, MicroChem, MA, USA) was preheated to 60 °C to reduce viscosity to cover the entire wafer. After dehydration bake, the silicon wafer was transferred to a 60 °C hot plate. Preheated photoresist (PR) was poured slowly onto the Si wafer to avoid bubble formation. The PR-coated wafer was left on the hot plate for 5 minutes until the PR evenly coated the entire surface.

Spin coating: Excess PR was removed by a spin coater (WS-400B-6NPP/LITE, Laurell, USA). Pre-spin was at 250 RPM for 30 s, followed by 400 RPM for 15 s (acceleration = 85 RPM s^{-1}). PR hanging over the wafer edge was removed with an acetone-soaked cloth. Spin coating was at 500 RPM for 15 s (85 RPM s^{-1}) followed by 1250 RPM for 30 s (340 RPM s^{-1}).

Acetone dispersion: Surface flaws are common after spin coating a thick layer of highly viscous PR. Surface flaws create uneven contact with the transparency mask during exposure, creating inconsistent features, and small variations in height create large variations in deflection. To homogenize the PR layer, we sprayed acetone on the PR-coated wafer preheated to 50 °C on a leveled hotplate. The sprayed wafer was covered for about 15 minutes until the acetone evaporated. Acetone dispersion lowers the viscosity of PR, removes tiny bubbles and surface divots, increases the uniformity of the PR film, and eliminates the edge bead to provide even contact with the pattern mask. This provides the same benefits of overnight edge bead remover[124] in a few minutes.

Soft bake: The wafer was heated to 95 °C (3 °C min^{-1}) on a hot plate and baked for 60 minutes. Then the hotplate was turned off and the wafer slowly cooled down to room temperature.

Exposure: The wafer was exposed to 365 nm ultraviolet light (5 mW cm^{-2}) for 75 seconds in mask aligner (MA65, Karl Suss, Germany) through a 20 000 DPI (dots per inch) transparency mask (CAD/Art, CA, USA).

Post-exposure bake: The exposed wafer was heated to 80 °C (3 °C min^{-1}) on a hot plate and baked for 20 minutes, followed by a slow cool down for 15 minutes. This longer post-exposure bake at a lower temperature reduces the thermal stress and risk of delamination for thick PR.

Development: The wafer was developed in SU-8 developer (MicroChem, MA, USA) for 20 minutes, then rinsed with fresh developer, IPA, and dried under nitrogen gas. To minimize thermal stress, no further hard bake was applied.

PDMS replica molding: Replica molding followed standard procedures.[125] The patterned wafer was coated with tridecafluoro-1,1,2,2-tetrahydrooctyl-1-trichlorosilane (TFOCS T2492, United Chemical Technology, PA, USA) for 2 hours in a desiccator. Sylgard 184 PDMS (Dow Corning, Midland, Michigan, USA), was mixed with curing agent at a 10:1 mass ratio and degassed. Degassed PDMS was poured onto the silicon wafer mold and degassed again, then baked in a convection oven at 60 °C for 90 minutes. Cured PDMS was cooled, separated from the mold, and cut to size. Holes were punched for the embryo inlet (4 mm diameter biopsy punch, Integra Miltex, Pennsylvania, PSA), gas inlet (14G blunt needle), and liquid outlets (19G). The patterned surface was cleaned with Scotch tape. The channel was covalently bonded to a 24 × 60 mm #2 glass slide (Warner Instruments, Cincinnati, USA) using oxygen plasma (Harrick Plasma Cleaner, 1 min, 18 W). The assembled device was sandwiched between two thick glass slides separated from the microfluidic system with thin polycarbonate film (McMaster-Carr, Illinois,

USA) using a binder clamp to ensure physical contact throughout the PDMS-glass interface during covalent bond development **(Appendix 2.2A)**. To fine-tune the rigidity of the PDMS sidewalls, the sandwiched device was post baked in a pre-heated oven at 150 °C (Isotemp Oven, Fischer Scientific, New Hampshire, USA).

Animal studies

Twist:eGFP flies (w[1118]; Dr[Mio]/TM3, Pw[+mC] = GAL4-twi. G2.3, PUAS-2xEGFPAH2.3, Sb[1] Ser[1]) were a gift from Emily Furbee, University of Pittsburgh. Oregon-R and H2A-RFP; moeGFP/TM6Tb flies were a gift from Brooke McCartney, Carnegie Mellon University. Flies were kept at room temperature in plastic bottles filled with standard *Drosophila* breeding medium. For embryo collection, flies were transferred to 100 mL tri-corner beakers and capped with 60 mm Petri dishes (Fisher Scientific, Pittsburgh, USA) partially filled with a solution containing 1.5% agarose, 2.5% sucrose, 25% apple juice, and 0.15% *p*-hydroxybenzoic acid methyl ester (methyl paraben to inhibit mold growth) and allowed to gel. A dab of yeast paste (1:2 parts dry yeast to water) was added to each plate. Embryos were collected for three hours, dechorionated for 90 seconds in fresh 50% bleach, washed with distilled water, collected with a cell strainer (Bellco glass), and suspended in egg wash (0.7% NaCl and 0.4% Triton-X 100 in distilled water, 0.2 μm-filtered, light-protected). Embryos were selected under stereoscope to collect those at early cellularization (stage 5, 2–3 hours after laying)[126] so compression would occur before gastrulation.

Analytical model for wall deflection

We developed an analytical model to describe the deflection of two sidewalls under pressure **(Appendix 2.1)**. The deflection of a beam of uniform thickness and loading fixed at both ends is described by the Euler–Bernoulli beam equation:

$$u(x) = \frac{w}{24EI}(x^4 - 2hx^3 + h^2x^2) \qquad \text{(eq. 2.1)}$$

where ω is the force per unit length (N/m), E is the Young's modulus (N/m^2), I is the second

moment of area (m^4), and h is the height of the sidewall (m). For further definitions and

nomenclature, see Appendix 2.1. If the aspect ratio of the sidewall (h/t) is less than 10, the

contribution of shear deformation should also be taken into account. Timoshenko's beam

theory[127] includes a secondary term for the contribution of shear deformation:

$$u(x) = \frac{w}{24EI}(x^4 - 2hx^3 + h^2x^2) + \frac{w}{2\kappa GA}(hx - x^2) \qquad \text{(eq. 2.2)}$$

where A is the cross-section area of the beam, and κ is Timoshenko's shear coefficient, which is

defined for beams with rectangular cross-section as:[128]

$$\kappa = \frac{10(1+v)}{12+11v} \qquad \text{(eq. 2.3)}$$

G is the shear modulus, which can be written in terms of Young's modulus and Poisson's ratio

(v) assuming PDMS is fully elastic and isotropic:

$$G = \frac{E}{2(1+v)} \qquad \text{(eq. 2.4)}$$

Relatively wide beams behave more rigidly because they resist lateral deformation from fiber

stresses.[129] This stiffening can be considered with a corrected term for the elastic modulus of

the beam, which approaches $E/(1 - v^2)$ as width approaches infinity.[130] In our system, sidewalls

are modeled as vertical beams **(Appendix 2.1)**, so beam width corresponds to microchannel

length L, and the width-to-thickness ratio (L/t) is large. Therefore, the limit value is more

accurate for approximating the effective elastic modulus,[130,131] yielding the final equation for

deflection:

$$u_{max} = \frac{Ph^4(1-v^2)}{32Et^3} \cdot \left(1 + \frac{4t^2(12+11v)}{5h^2}\right) \qquad \text{(eq. 2.5)}$$

Where P is the pressure applied to the sidewall (N/m^2). This can be expressed in terms of the effective channel width:

$$W' = W - \frac{Ph^4(1-v^2)}{16Et^3} \cdot \left(1 + \frac{4t^2(12+11v)}{5h^2}\right) \qquad \text{(eq. 2.6)}$$

where W is the initial channel width and W' is the effective channel width after applying pressure to deflect two sidewalls.

Numerical simulation

To predict the shape of the channel wrapping around an embryo, we constructed a 3D CAD model of thin PDMS sidewalls and an embryo in SolidWorks 2016 (Dassault Systèmes, Vélizy-Villacoublay, France), and modeled them in Abaqus (Dassault Systèmes, Vélizy-Villacoublay, France) as fully elastic and isotropic materials with quadratic tetrahedral elements. First, the elastic sidewall deflection was simulated without embryos. Parametric studies determined the Young's modulus of PDMS sidewalls based on experimental results. Then, *Drosophila* embryos were added to the simulation. A similar parametric study used the known Young's modulus of PDMS sidewalls to estimate the Young's modulus of *Drosophila* embryos. Simulations of embryo compression proceeded in two steps. First, embryos received passive compression by a microchannel with a smaller width, which was simulated by displacing the wall towards the fixed embryo. In the second step, embryos received active compression, which was simulated by applying pressure to the deformable PDMS sidewall. Poisson's ratio for PDMS[132] and *Drosophila* was set to 0.4999 to avoid numerical divergence.

Experimental setup

Pneumatic connections were made with Tygon 3350 Silicone tubing with 1/32" inner diameter (Saint-Gobain, France) and fittings of the appropriate size. Consistent pressure was applied by outfitting a compressed air tank with a custom-made fine Bourdon tube pressure gauge with 0.1 PSI resolution. Consistent vacuum was applied either by running water through a Venturi trap or by using the building vacuum. Embryo wash solution was passed through 0.2 μm syringe filters to avoid clogging the microchannels. As a control for manipulation in the chamber, embryos were mounted on a coverslip glass fixed to the bottom of a plastic Petri dish. Embryos were adhered to the coverslip with a thin layer of glue prepared by dissolving the adhesive from double-sided Scotch tape in heptane. Adhered embryos were covered with a drop of halocarbon oil (series 700; Halocarbon Products, Hackensack, NJ). To apply 50% hypoxia (10% oxygen), the dish setup was placed into a stage-top environmental chamber (LiveCell; Pathology Devices, Westminster, MD) connected to an equal-pressure mixture of argon and air using a T-fitting. To apply anoxia, the dish setup was evacuated for 10 minutes, then placed into the environmental chamber connected only to argon.

Image acquisition and processing

Compressed embryos were imaged inside the microfluidic device. Images were acquired on a spinning disk confocal microscope (Nikon Eclipse Ti, running Andor iQ 3.5 software and fitted with an iXon X3 camera). 3D-image stacks were acquired with a 10× objective at 10 μm optical sections for a total depth of 200 μm. The liquid inlet of the microfluidic device was sealed with a coverslip to prevent evaporation during extended imaging. Time-lapse images were acquired in differential interference contrast (DIC) and fluorescence with a 250 mW 488 nm laser with identical settings for power, exposure, and gain. Each time-lapse session

comprised multi-position recordings of 60–120 embryos with 3Dimage stacks were acquired

every hour for 4 hours. The resulting hyperstacks were manually marked with an elliptical

region of interest (ROI), and a custom macro recorded mean pixel values for each slice and

frame in Fiji.[133]

Results and Discussion

Design and operation of the microfluidic device

Our microfluidic device compresses hundreds of *Drosophila* embryos by aligning them

between two sidewalls and deflecting those walls with pressure **(Figure 2.1)**. The device consists

of two interlaced compartments: a liquid compartment introduces and aligns embryos **(Figure

2.1)**. A gas compartment uses microchannels with a closed end to create pneumatic actuation on

either side of the liquid compartment, which controls the effective width of the liquid channels to

load or compress embryos **(Figure 2.1e)**. This configuration was parallelized into three

compression channels to triple the throughput of the system. When pressurization bends the

sidewalls, it also creates a normal force on the roof of the gas channels, which pushes the thin

sidewalls away from the glass slide, which can create leaks. To prevent such leaks, each parallel

configuration was separated by a 1.5 mm region of PDMS which provides a large surface area of

contact with the glass slide, functioning as a buttress. The channels were constructed entirely

from PDMS, which is optically transparent and oxygen-permeant.[134] The PDMS structure was

bonded to a #2 coverglass, enabling high resolution fluorescence microscopy.

Embryos were loaded into the device by pipetting them into the large inlet of the liquid

compartment **(Figure 2.1a)**. A narrowing atrium aligned embryos into a single file **(Figure

2.1b)**. The section with deformable sidewalls was designed with a narrower width than the

embryos **(Figure 2.2b)**, preventing embryo entry. When vacuum was applied, the PDMS

sidewalls deflected outwards **(Figure 2.1c)**, increasing the effective width of the channels, allowing embryo entry. Tilting the device caused embryos to sediment into three parallel compression channels **(Figure 2.1f)**. Compression channels terminated in a bottleneck 90 μm wide **(Figure 2.1b)**, which allowed fluid flow while retaining embryos.

After the embryos were loaded into the compression channel, the vacuum was removed and the sidewalls recoiled, immobilizing the embryos due to PDMS elasticity **(Figure 2.1d)**. Compression focuses embryos to the vertical center of the channel where wall resistance is lowest **(eq. 2.1, Figure 2.2e)**. Higher compression was achieved by applying pressure to the gas compartment, which deformed the sidewalls inwards **(Figure 2.1e)**. Therefore, this system operates in two modes: without external pressure (0 PSI), for immobilization and mild passive compression, and with external pressure (1–5 PSI), to apply an active compressive strain. For post-analysis, embryos were recovered by opening the sidewalls under vacuum, tilting the channel, and collecting embryos from the inlet. Each microfluidic device accommodated up to 120 embryos in a single run: compression channels were 20 mm long, *Drosophila* embryos were $\approx$ 500 μm long, and the device operated three channels in parallel. For larger sample size, we developed 40 mm channels that can accommodate up to 240 embryos.
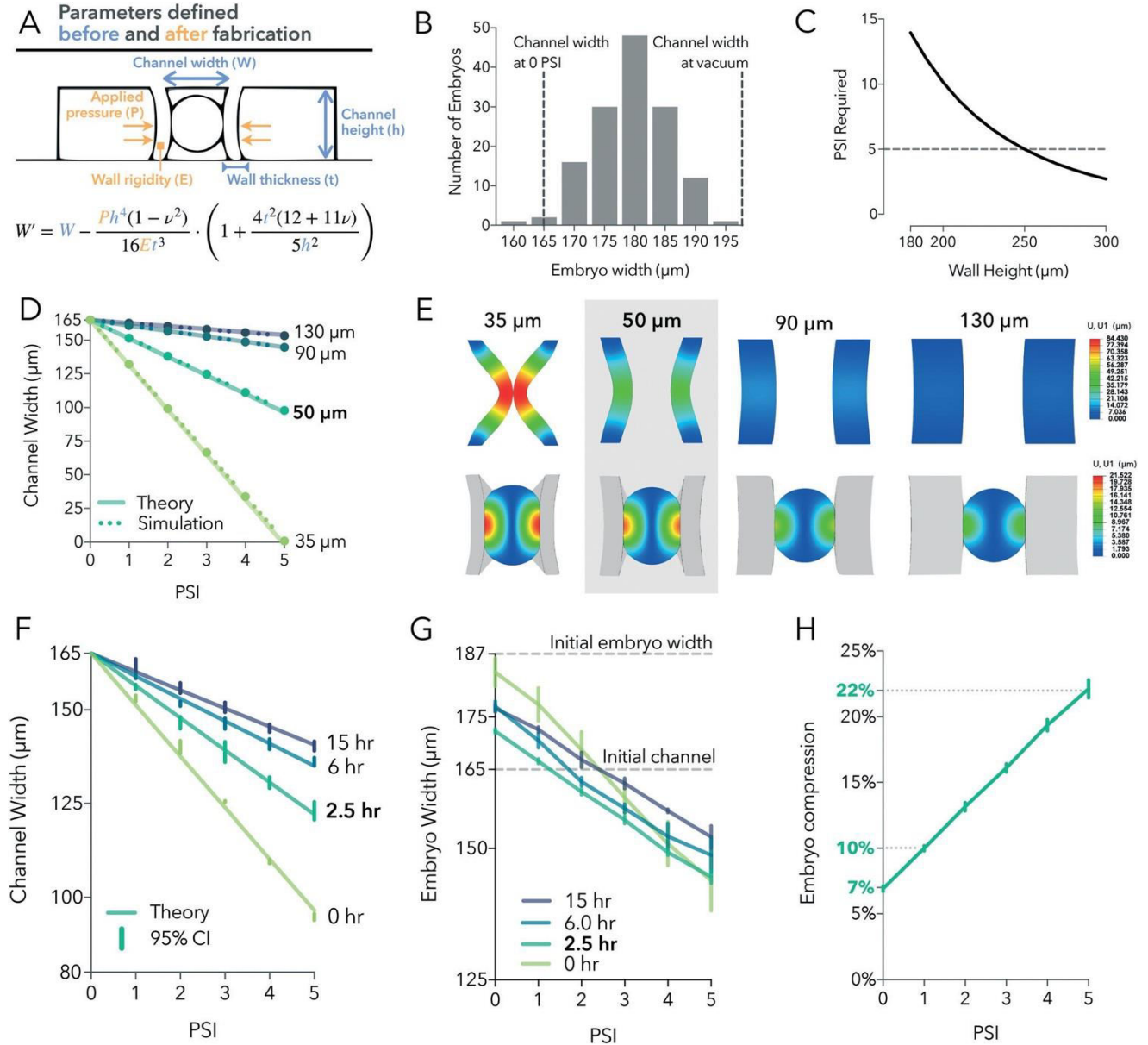
Figure 2. 2. Defining five parameters for a microfluidic device: **(a)** overview: the effective width of a channel under pressure (*W'*) is described by eq. 6 with five parameters. Three were defined before fabrication (blue) and two were determined afterwards (orange). The goal was to maximize compression while limiting pressure to 5 PSI for reliable function. **(b)** Initial channel width was determined by measuring the width distribution of stage-5 Oregon R embryos (*n* = 140). A channel width of 165 μm immobilizes >99% of embryos at rest (0 PSI) while expanding under vacuum to accommodate the widest embryo. **(c)** Channel height: theoretical prediction of PSI required to sufficiently deflect a wall of varying height. Height was maximized at 250 μm to enable compression at 5 PSI. Wall height has the greatest influence over deflection, as indicated by the polynomial degree of the governing equation. **(d)** Wall thickness: deflection under pressure was calculated theoretically (solid line) and by numerical simulation (dotted line). Simulation agrees with analytical eq. 2.6 **(e)** Simulated deflection of sidewalls at 5 PSI in a range of thickness with and without embryos (side view cross-section). 50 μm walls (shaded) were selected for the greatest range of compression with the least wrapping around the embryo. **(f)** Wall rigidity: longer post-cure baking results in more rigid walls (higher Young's Modulus) that deflect less under pressure. Continuous theoretical results with the discrete experimental measurements from 1 PSI increments (95% CI bars). **(g)** Embryo width between side- walls with a range of rigidity (95% CI bars). 2.5 hours post-cure bake showed the greatest range of compression with minimal wrapping. **(h)** Uniaxial compressive strain (normalized change in embryo width) in the final channel after design optimization (95% CI bars).

Design calibration for *Drosophila* embryo compression

Compression can be precisely regulated by calibrating five parameters: the width and height of the compression channel, the thickness and the rigidity of the deformable sidewalls, and the applied pressure **(Figure 2.2a)**. The final design calibrated for *Drosophila* compression had a channel width of 165 μm **(Figure 2.2b)**, channel height of 251.8 μm **(Figure 2.2c and Appendix 2.2B)**, wall thickness of 50 μm **(Figure 2.2d and e and Appendix 2.3)**, and a post-bake of 2.5 hours at 150 °C **(Figure 2.2f and g and Appendix 2.4)**. This resulted in a compression that could be tuned between 0–22% **(Figure 2.2h)** with a standard deviation less than 2.4% **(Appendix 2.6)**. Omitting the post-bake, the softer channel walls apply <1% compression at 0 PSI to immobilize samples for timelapse imaging **(Figure 2.2g)**.

Channel width: We want a compression channel that is narrower than embryo width to immobilize them passively. However, the channel must also be wide enough under vacuum to allow the biggest embryo to enter without clogging the channel. We measured the width of 140 stage-5 Oregon-R embryos and found a normal distribution with a mean of 179.6 ± 1 μm (95% confidence interval, σ = 6 μm, SEM = 0.5 μm, max = 194.7 μm, Figure 2B). Based on this distribution, a channel width of 165 μm can immobilize >99% of embryos passively. When vacuum is applied, the sidewalls deflected outwards to create an effective width of about 205 μm, allowing the widest embryo to enter **(Figure 2.2b)**.

Applied pressure: Pressure is limited by the bond strength between the thin PDMS sidewalls and the glass slide. Any point-sized separation across any 20 mm sidewall causes a leak and failure of the entire channel. Although high pressure increases sample compression range, we found that increasing the pressure past 5 PSI led to unreliable function, and therefore used 5 PSI as an upper limit throughout this study.

Channel height: A key challenge in adapting microfluidics to micromechanics is maximizing height, which has the strongest influence over deflection **(eq. 2.5)**. Maximizing height creates a fabrication challenge in photolithography because the maximum aspect ratio is limited due to diffraction,[135] absorption of light,[136] and chemical diffusion of crosslinking agents,[137] which deform the final geometry and increase the risk of photoresist delaminating from the silicon wafer during curing.[138] Height must be at least greater than the largest embryo (195 μm) to prevent clogging, with some additional allowance for vertical expansion during lateral compression. Height must be at least 250 μm to reasonably deflect at 5 PSI, based on theoretical calculations to deform a 50 μm PDMS wall by 15 μm **(Figure 2.2c)**. Based on this target height, we used our modifications on ultra-thick photolithography to fabricate SU-8 molds with an average height of 251.8 μm with uniformity >95% **(Appendix 2.2B)** as measured by Zygo NewView 7200 3D optical surface profiler (Zygo Corporation, Middlefield, Connecticut, USA).

Wall thickness: To maximize deflection under limited pressure, we also want to minimize wall thickness, which has an inverse-cube influence over deflection **(eq. 2. 5)**. However, reducing wall thickness reduces their surface area contact with the glass slide, which increases the chance of leaking under pressure. To optimize wall thickness, we used finite element analysis to simulate the deflection of PDMS sidewalls of 35, 50, 90, and 130 μm thickness from 0 to 5 PSI, first by themselves and then with an embryo between them **(Figure 2.2E and Appendix 2.3)**. Simulation results were compared to analytical predictions from equation 5 **(Figure 2.2d)**. Although maximal displacement occurred with 35 μm side walls, such thin walls wrap around the embryo **(Appendix 2.2e and 2.3)**, which decreased the surface area exposed to media and could increase the risk of hypoxia. Additionally, these high aspect ratio sidewalls create significant difficulty in fabrication for a modest gain in displacement. Walls 90 and 130 μm thick

are too stiff to provide adequate compression range **(Figure 2.2e, Appendix 2.3)** so we chose 50 μm for the thickness of the deformable sidewalls. At 5 PSI, 50 μm walls decrease the effective width of the channel by 57%, creating a 22.4% compressive strain on embryos. Over 0–5 PSI, this provides a large dynamic range of embryo compression **(Figure 2.2h)** within a tractable aspect ratio for fabrication.

Sidewall rigidity: Rigid walls deflect less under pressure but compress the embryo to a greater extent of that deflection. Conversely, soft walls deflect more, but are less compressive, as they wrap around the embryo **(Appendix 2.3)**. To optimize rigidity, we added a bake step for 0, 2.5, 6, or 15 hours at 150 °C after plasma bonding to increase the rigidity (Young's modulus) of crosslinked PDMS[139] **(Appendix 2.2 and 2.4)**. These differentially baked channels were simulated numerically **(Appendix 2.4)** and measured experimentally **(Figure 2.2f and g)**. As expected, longer baking time resulted in walls with an increased Young's modulus **(Appendix 2.2C)** that deflected less under pressure **(Figure 2.2f)**. To quantify sidewall wrapping, we calculated the ratio of embryo deflection to wall deflection which we call "compression efficiency" **(Appendix 2.2D)**. The most rigid walls showed the greatest compression efficiency but traveled less distance; this resulted in a lower overall compression. The optimal rigidity was the 2.5-hour bake, which showed linear compression up to 22% at 5 PSI with minimal wrapping **(Figure 2.2h)**.

Determining Young's modulus of PDMS and *Drosophila*

The Young's modulus of cross-linked PDMS is highly variable, ranging 3 kPa to 3.7 MPa[140] depending on curing agent ratio, curing temperature, duration, size,[141] and age.[142] The analytical model was used to estimate the Young's modulus of PDMS to be 1.88 MPa, comparable to values found by similar fabrication parameters.[139] Based on this value, simulations of embryo compression determined the Young's Modulus of *Drosophila* embryos to be 160 kPa,

which is comparable to results from alternative approaches.[143] To determine simulation error, the experimentally observed deflection was used to calculate Young's modulus with equation 6, which was then used to run a simulation of deflection. The resulting simulated displacement was compared to the experimentally observed displacement. This process showed the simulation and analytical model to describe deflection within 0.3% error across all sidewall rigidities. Although we model embryo behavior as purely elastic, it is actually viscoelastic,[144] transitioning from viscous to elastic[145] as described by the Kelvin–Voigt model.[146] During this transition, applying a constant force creates a time-dependent strain called viscoelastic creep.[147] To test whether viscoelastic creep affected our setup, we measured the width of compressed embryos over four hours and observed no decrease in embryo width. This is consistent with reports of other embryonic tissue transitioning to a purely elastic response within several minutes.[146,148] This suggests that viscoelastic creep is not significant in this setup, and the amount of compression applied to embryos can be modeled based on its steady-state elastic response.

Embryo survival and development

To test whether PDMS channels and compression affect viability, Oregon-R embryos were compressed by 7% or 22% for either 10 minutes ($n = 34$, 64 respectively) or 4 hours ($n = 38$, 100, **Figure 2.3**). As a control for compression, embryos were loaded into the PDMS channel and never compressed; the walls were held open under vacuum ("vacuum control," $n = 68$). As a control for exposure to the device, embryos were cultured in a glass dish ($n = 111$). Embryos were recovered from the device to glass dishes and observed under a brightfield stereoscope at 24 and 48 hours, and scored as first-instar larvae, dead, or developing according to morphological features.[126] Two-tailed chi-square test compared observed distribution to expected distribution from dish control.

Vacuum controls showed no developmental difference from dish controls, with 75% reaching larval stage by 48 hours (**Figure 2.3a *vs.* b**) suggesting that exposure to PDMS channels alone does not affect development or survival. Surprisingly, 7% compression for 10 minutes and 4 hours showed greater survival rates compared to dish controls (**Figure 2.3c and e *vs.* a**). One explanation is that the stiff chorion membrane mechanically constrains *Drosophila* embryos, and the standard practice of removing it decreases survival, which is recovered by mild compression. Embryos compressed by 22% for 10 minutes initially showed developmental delay at 24 hours, but ultimately reached first instar by 48 hours at rates greater than dish controls (**Figure 2.3a *vs.* d**). Extending 22% compression to 4 hours reduced survival to 37%; embryos that appeared alive and delayed at 24 hours did not recover by 48 hours (**Figure 2.3f**).

To examine early development in greater detail, we took DIC images of embryos in the channel every hour for 4 hours. Embryos can be seen at stage 5 inside the channel (top row). Embryos compressed by 7% appear to proceed through germ-band extension, similar to uncompressed embryos. A minority of embryos compressed by 22% for 4 hours appeared to show no movement for one hour, but then proceeded through germ-band extension. These results contradict reports of a ventralized phenotype that fails to extend the germ band after compression.[94] This difference in developmental milestones could be from several factors: (1) previously, embryos were observed up to 50 minutes before concluding the phenotype was stable; observing over 4 hours shows recovery is possible; (2) there might be effects from the differences in genetic background in fly stocks used in these experiments; (3) there might be effects that stem from different methods of compression that result in variations in strain magnitude and consistency.
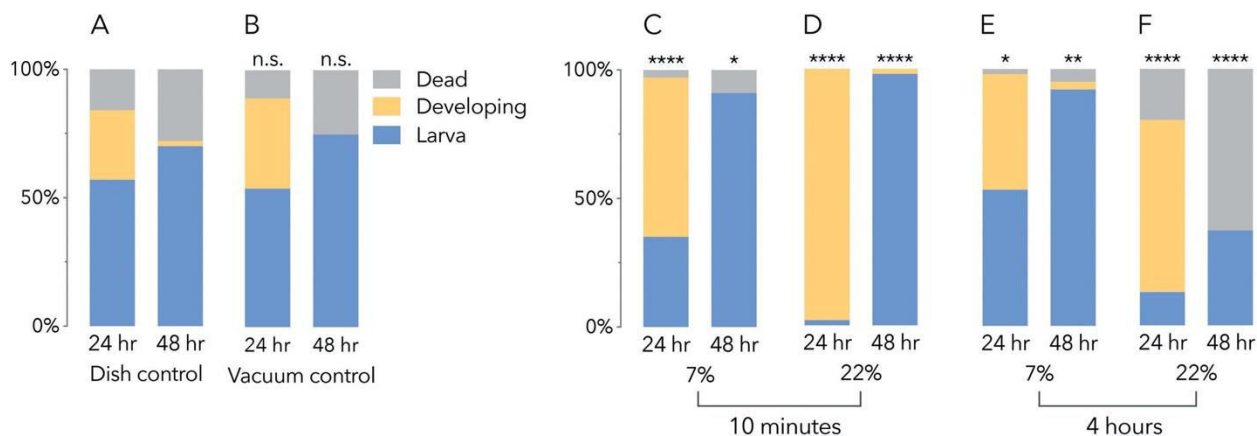
Figure 2. 3. Survival in the channel. **(a)** Percentage of wildtype embryos that reached larval stage, were still developing, or dead, 24 and 48 hours after compression ($n = 111$). **(b)** Vacuum controls ($n = 68$) were loaded into the channel but never compressed. **(c and e)** Embryos compressed at 7% ($n = 34, 38$) showed greater survival rates than controls. **(d)** 22% compression for 10 minutes ($n = 64$) led to developmental delays but greater overall survival; **(f)** 22% compression for 4 hours ($n = 100$) led to death. Statistics compare observed distribution to dish control.

Comparison of compression methods: To compare our compression to previous work, we numerically simulated the approach of Farge 2003.[94] Specifically, Farge's compression was (1) applied vertically and observed indirectly by 10% lateral expansion, orthogonal to the direction of compression; applied by rigid glass. We simulated embryo deformation by a rigid plate sufficient to create a 10% lateral expansion **(Appendix 2.5)**. The resulting inferred compression was 25–34%. This inferred uniaxial compression is larger because shape change begins vertically; height decreases substantially before significant lateral expansion occurs. This greater compression may explain observed differences in developmental arrest.

Based on numerical simulations, compression by glass is more variable than compression by PDMS. When compressing walls are rigid, channel width is strict, resulting in greater compression for wider embryos **(Appendix 2.6A)**. In contrast, when compressing walls are flexible, wider embryos can resist wall displacement, creating an effective channel width unique to each embryo **(Appendix 2.6B)**. As a result, compressive strain is more variable under stiff walls than flexible walls. This variation can be quantified by simulating compression of embryos

63

with mean width (180 μm), maximum width (195 μm), and minimum width (160 μm) in the same channel **(Appendix 2.6)**. In lateral compression by glass, embryo strain shows a standard deviation that is 39% of the mean (CoV). In lateral compression by PDMS, strain was most consistent at 11% CoV. In vertical compression by glass sufficient to obtain 10% lateral expansion, the uniaxial compressive strain ranges from 25% to 34% with CoV of 16%.

Overall, the channel itself neither delays nor destroys *Drosophila* embryos. Compression appears to switch from beneficial to harmful above a threshold of magnitude and time. These observations highlight the importance of long-term analysis, as developmental outcomes can drastically diverge days after mechanostimulation. Flexible PDMS sidewalls apply compression that is more consistent and directly measurable, which helps compare results across multiple studies.

Anoxia: The gas permeability of PDMS is well established for cell culture,[134] but not for whole-organism *Drosophila*. Anoxia produces a rapid developmental arrest during which interphase chromosomes prematurely condense.[149] Chromatin condensation can be visualized by fusing histone H2A to a red fluorescent protein (H2A-RFP). As a positive control, anoxia was induced by placing H2ARFP embryos in a coverslip dish and evacuating for 10 minutes, then under a continuous flow of argon in a stage-top environmental chamber. As expected, nuclei remained developmentally arrested **(Figure 2.4a)** and chromatin condensation was observed as fluorescent puncta **(Figure 2.4c)**. In contrast, embryos in the microfluidic device proceeded through nuclear division with typical timing **(Figure 2.4b)**, showed decondensed chromatin, and large-scale morphogenetic movement **(Figure 2.4d)** even at 5 PSI (22% compression). These results confirm that the microfluidic device provides sufficient oxygen to prevent anoxia.
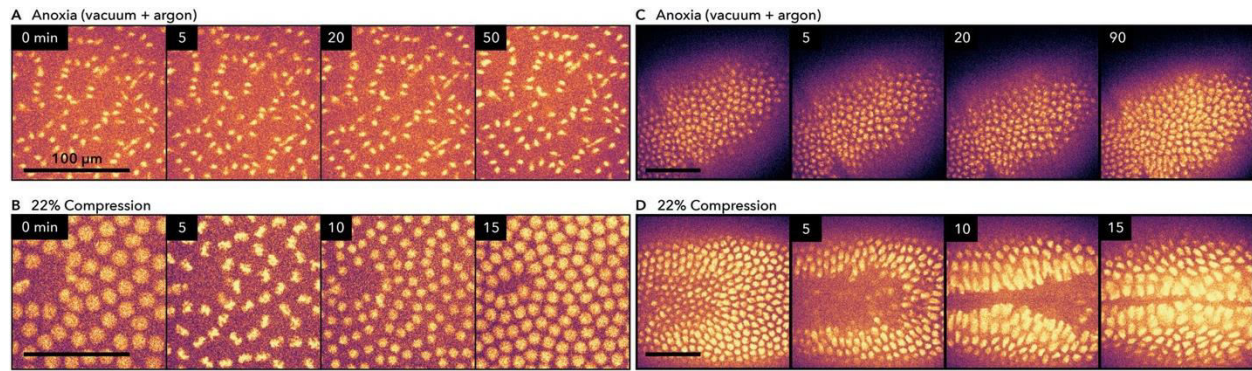
Figure 2. 4. Channel compression does not induce anoxic arrest. Developmental arrest can be visualized by chromatin condensation, seen in embryos expressing H2A-RFP (color by Matplotlib inferno LUT, all scale bars 100 μm). **(a)** Embryos kept anoxic by 10 minutes of vacuum followed by continuous argon show morphogenic freezing; nuclei in anaphase stay arrested for over 50 minutes. **(b)** Compressed embryos pass through anaphase normally, doubling nuclei over 10 minutes. **(c)** Anoxic embryos also show chromatin condensation, visible as puncta in nuclei that fail to divide over 90 minutes. **(d)** Compressed embryos show diffuse fluorescence indicating decondensed chromatin, and continue development.

Mechanical induction of twist

Mechanical induction of *twist* was first described by Farge in 2003.[94] To examine whether microfluidic compression also induces *twist* expression, we monitored fluorescence from the *twist* promotor driving eGFP, measured every hour for 4 hours **(Figure 2.5)**. In unconstrained embryos, *twist*:eGFP localized to a stripe of ventral furrow cells, indicating normal expression **(Figure 2.5a)**. Constrained embryos showed widespread expression that was brighter and ectopic **(Figure 2.5b–e)**. This is consistent with the hypothesis that *twist* expression is coordinated by mechanical force; during normal development, *twist* is selectively expressed in ventral furrow cells that experience internal mechanical forces due to morphogenetic movement. When the entire embryo is compressed, the whole organism experiences mechanical stimulation, which is sufficient to induce ectopic expression of *twist*.

To quantify the increase in *twist*:eGFP fluorescence, we measured mean fluorescence pixel intensity. As a control for compression, embryos were introduced into the chamber with the walls held open by vacuum, and all significance tests were made relative to this vacuum control. As a control for handling embryos in the channel, embryos were observed under halocarbon oil on a coverslip (dish control). Four hours after compression, all embryos showed an increase in *twist*: eGFP fluorescence **(Figure 2.6a)**. Embryos compressed for 10 minutes showed a significant dose-dependent increase in *twist*:eGFP when compressed by 7% ($p < 0.01$) and 22% ($p < 0.0001$; ordinary one-way ANOVA to vacuum control, Figure 6). Embryos also showed a duration-dependent increase in *twist*: eGFP when 7% compression was extended to 4 hours ($p < 0.0001$, **Figure 2.6b**). In the 22% 4 hour condition, *twist*:eGFP fluorescence was not significantly different from vacuum controls in magnitude. Yet the distribution of that expression remained ectopic **(Figure 2.5 inset, e *vs.* a)**. This is consistent with the idea that both the dose and the duration of compression are biologically relevant. One explanation for the lower
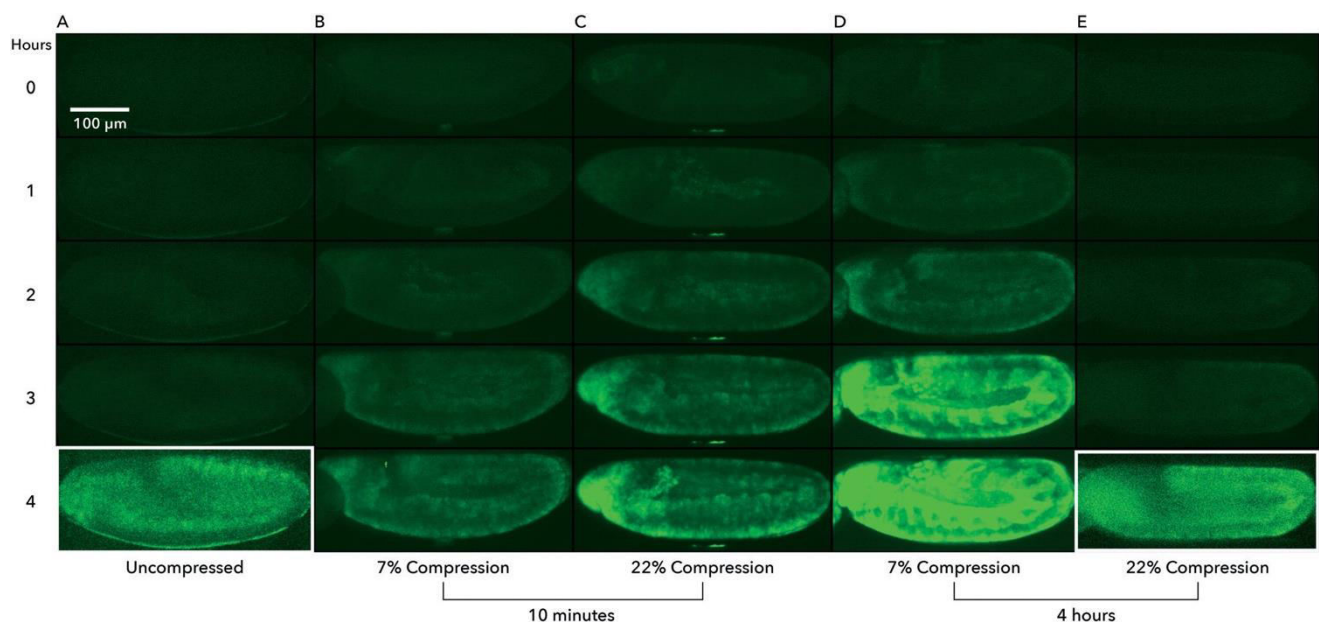
Figure 2. 5. Ectopic distribution of *twist*:eGFP in compressed embryos. *Twist*:eGFP fluorescence was measured every hour over 4 hours. Pixel value settings are the same for all images, except for A4 and E4 (white border) to show patterning. **(a)** Uncompressed embryos show a ventral stripe of *twist*:eGFP expression. **(b and c)** Embryos compressed for 10 minutes show an increase in *twist*:eGFP over 4 hours. **(d)** Embryos compressed by 7% for 4 hours show substantial increase in fluorescence. **(e)** Embryos compressed by 22% for 4 hours show low but ectopic fluorescence.

fluorescence magnitude is that embryos in this condition are already committed to die within 48 hours **(Figure 2.3f)**, perhaps because this amount of compression disrupts the integrity of the embryo.

Hypoxia: The microfluidic device provides sufficient oxygen to avoid full anoxia, but also confines embryos to a small volume of media and applies vacuum during loading, which could induce partial hypoxia. Hypoxia is a confounding explanation for the increase in *twist*:eGFP after compression: hypoxia-inducible factor (HIF-1α) may upregulate *twist* mRNA by binding to a hypoxia-responsive element in the proximal promoter.[150,151] This pathway was demonstrated in tumor cell lines and in *C. elegans* mutant for the *twist* homolog (hlh-8), but remains unconfirmed in *Drosophila*.[151]

To investigate whether hypoxia could explain the increase in *twist*:eGFP after compression, we intentionally induced a 50% oxygen shortage by flowing equal pressures of compressed atmospheric air and argon through a stage-top environmental chamber. Embryos continued to develop, and the resulting *twist*:eGFP fluorescence after 4 hours was reduced compared to normoxia controls ($p < 0.0001$, **Figure 2.6**), likely due to interference with eGFP folding.[152] This suggests that hypoxia cannot explain the increase in *twist*:eGFP after compression.

The increase in fluorescence in vacuum controls compared to dish controls **(Figure 2.6)** was unexpected. One explanation is that in a dish, when sample size is sufficiently large, standard techniques introduce clusters of embryos that compete for oxygen, which inhibits eGFP. The microfluidic device may provide better access to oxygen than dish controls by maintaining consistent density and surrounding embryos with a thin wall of oxygen-permeant PDMS.

Another explanation is that the increase in fluorescence in vacuum controls is an artifact of handling. While switching tubing for microscopy, the vacuum was discontinuous for approximately one minute, causing a brief flexing of the sidewalls, which could trigger an intermediate *twist* response. Consistent with this hypothesis, vacuum controls in survival experiments that did not require switching tubing also did not show an intermediate response between dish control and compression **(Figure 2.3a *vs.* b)**. Taken together, the potential for rapid induction of *twist* expression highlights the need for precise temporal control when studying mechanotransduction.
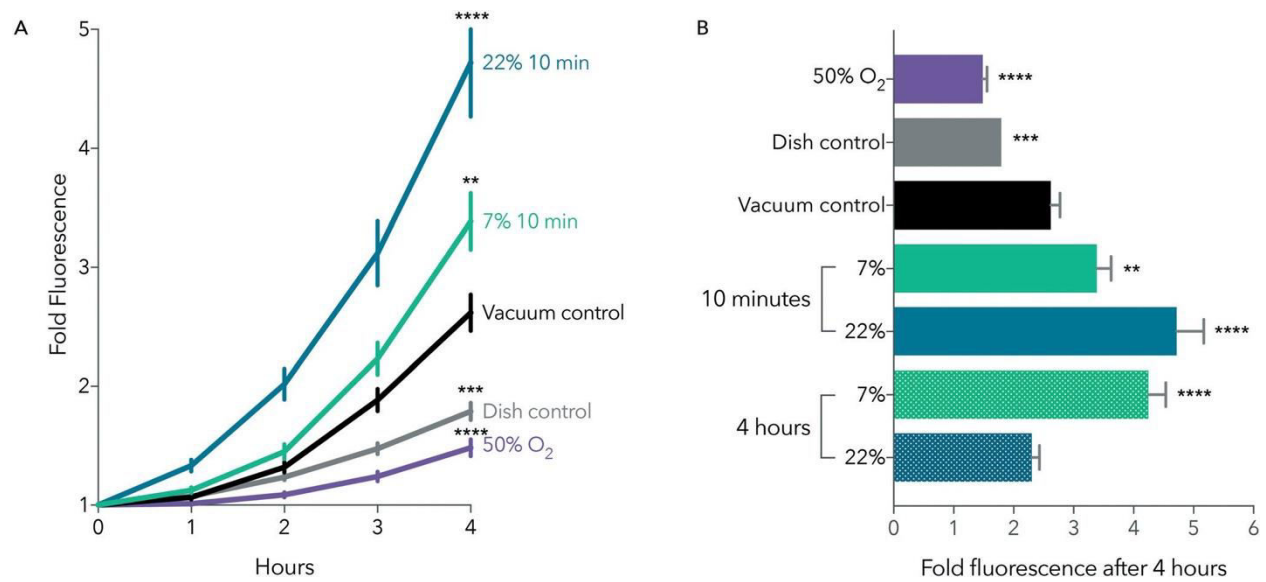
Figure 2. 6. Mechanical induction of *twist* expression. **(a)** *Twist*:eGFP fluorescence was measured every hour over 4 hours after compression. Embryos show a significant increase in mean fluorescence when compressed for 10 minutes by 7% (0 PSI, $p < 0.01$) and 22% (5 PSI, $p < 0.0001$; ordinary one-way ANOVA to vacuum control, SEM bars). Vacuum controls were introduced into the channel with the walls held open; dish controls remained outside the channel. Hypoxia (50% O_2) decreased *twist*:eGFP expression ($p < 0.0001$). **(b)** Summary of *twist*:eGFP fluorescence after 4 hours (SEM bars, ordinary one-way ANOVA to vacuum control).

Conclusion

We developed a novel microfluidic device that automatically aligns and immobilizes hundreds of *Drosophila* embryos without external force. This device precisely compresses

hundreds of embryos using deformable pressure-actuated sidewalls, allows for live imaging, and retrieval of live embryos for post-analysis. We describe a method for consistent ultrathick photolithography, derive an analytical model that describes sidewall deflection, and discuss the calibration of five parameters critical to designing microfluidic devices. The device itself does not affect survival or development and does not induce anoxic arrest. Using this device, we measure the Young's modulus of PDMS sidewalls and *Drosophila* embryos and observe that compressing embryos is sufficient to trigger the mechanical induction of *twist* that is dose- and duration-dependent.

Chapter 3: Endothelial Cell Polarization and Orientation to Flow in a Novel Microfluidic Multimodal Shear Stress Generator

Introduction

Fluid shear stress, which arises from the intermolecular friction between differentially moving fluid layers, is an important hemodynamic factor that orchestrates the form and function of the blood vasculature through mechanosensitive signaling pathways. The inner lining of the vasculature is a single-layered squamous epithelium composed of endothelial cells (EC). Shear stress experienced by ECs at the vessel walls—known as wall shear stress (WSS)—has a profound influence on EC gene expression and behavior, with laminar shear stress inducing quiescence and disturbed (low or oscillatory) shear stress driving an inflammatory state [153]. Additionally, laminar but not disturbed shear stress promotes EC elongation and cytoskeletal alignment parallel to the flow axis. Furthermore, in response to flow, ECs polarize, defined here as a distinct separation of the Golgi apparatus or microtubule organizing center (MTOC) and the nucleus. Polarized ECs generally orient against the direction of flow, with the Golgi or MTOC located upstream of the nucleus [154-156].

Although EC upstream orientation in response to flow is well documented, how this orientation affects EC function is not entirely clear. A lack of EC upstream orientation may be necessary but not sufficient for a pathological inflammatory response [156], and there is continuing debate regarding the correlation between Golgi-nucleus orientation and the direction of cell migration. Generally, in migrating single cells, the Golgi is positioned toward the leading edge, ahead of the nucleus [157]. However, in ECs under flow, there are reports of correlation [158,159] and lack of correlation [155,160,161] between the orientation of the Golgi-nuclear vector and the direction

of migration. Regardless, it is clear that Golgi-nucleus polarization and orientation are reproducible and sensitive EC responses to uniform laminar shear stress in vitro and in vivo [156].

There is also mounting evidence that ECs are not only sensitive to the WSS magnitude but also to the WSS gradient (WSSG) [162-165]. During development, WSSGs help to shape the vasculature, with EC Golgi-nucleus orientation and migration toward regions of higher shear stress during vascular remodeling [166,167]. Moreover, high WSSGs are associated with intracranial aneurysm development and atherosclerotic plaque instability [168-171]. However, how WSSGs are sensed is poorly understood.

In vivo assays preserve the physiological complexity of the dynamic mechanical environment in the vasculature [172] but cannot decouple the role of shear stress from circulating factors. Furthermore, in vivo assays limit access to high-content imaging needed for mechanical characterization of blood flow and analysis of EC behavior. Moreover, natural variations in cardiovascular physiology limit reproducibility, hindering the establishment of precisely defined mechanistic relations between shear stress and EC biology. By contrast, microfluidic systems allow the generation of precisely controlled shear stress modalities in highly controlled microenvironments, and the effects of shear stress on pathologically-relevant EC phenotypes—such as cell alignment, polarization, intracellular organization, cytoskeletal rearrangement, apoptosis, and permeability—can be comprehensively investigated [173].

Despite the advantages of microfluidic devices, their full potential is rarely realized, as most systems fail to reproduce a broad spectrum of physiologically relevant shear stress magnitudes and gradients. Within the human blood vasculature, shear stress magnitudes range between 5 to 60 dyne.cm^{-2} [174], and spatial shear stress gradients are predicted to be as high as 3 dyn.cm^{-2}/mm [175]. Yet, many microfluidic platforms limit experiments to a single shear stress

condition and therefore require numerous repetitions with different flow rates to encompass physiologically-relevant shear stress modalities [176-183]. Other microfluidic systems can simultaneously generate multiplexed shear stress regions within the same device [184-190]. However, these systems are limited to a single mode of shear stress, with either shear stress gradient regions or uniform shear stress regions. Moreover, because these devices typically rely on parallel microchannels that branch from a common inlet channel via hydraulic resistance channels [185,191], they suffer from numerous limitations, including non-uniform cell seeding density that significantly affects the local flow fields [192], and localized flow perturbations affecting all microchannels [193]. Additionally, each of the devices above require increased complexity of the flow circuit due to the need for an independent outlet for each perfusion channel.

To our knowledge, there is currently no microfluidic system that is capable of generating shear stress gradients in conjunction with different uniform shear stress regions for systematic analysis of shear stress-dependent cellular responses. Given that EC responses to flow may depend on the direction (i.e. sign), steepness (i.e., slope), and the average shear stress magnitude of the shear stress gradient [163], an ideal microfluidic system would allow simultaneous interrogation of EC behaviors in response to all these parameters. To address this need, we used 3D-printed molds to rapidly fabricate a novel microfluidic device that can simultaneously generate multiple shear stress modalities, allowing systematic mechanical screening and profiling of cells in physiologically relevant dynamic flow conditions. Our microfluidic system is composed of microchannels with a constant height but variable widths, connected to each other in serial and parallel fashion. These microchannels comprise multiple shear stress regions, including three different magnitudes of uniform WSS and six different WSSGs (three positive,

72

three negative). We characterized this system using analytical models and numerical simulations together with experimental validation.

To highlight the utility of this device, we quantitatively analyzed Golgi-nucleus relative position in human umbilical vein endothelial cell (HUVEC) monolayers using both endpoint and time lapse imaging. We found that flow-induced Golgi-nuclear polarization increased immediately after the onset of flow, concomitant with decreased Golgi and nuclear areas and increased Golgi-nuclear separation. However, while the frequency of polarized ECs was similar across all shear stress modalities, the frequency of ECs with Golgi-nucleus upstream orientation increased as WSS magnitude increased. Upstream orientation was also enhanced in regions of negative shear stress gradients and inhibited in regions of positive shear stress gradients.

Materials and Methods
Microchannel fabrication
Microfluidic channels were fabricated out of Polydimethylsiloxane (Sylgard 184 PDMS; Dow Corning, USA) using replica molding technique with 3D-printed molds. First, negatives of the microchannel geometries were modelled in SolidWorks 2016 (Dassault Systèmes, Vélizy-Villacoublay, France). The molds were manufactured using VIPER si2T Stereolithography System (3D Systems, Rock Hill, South Carolina, USA) in high quality mode with Accura SI 10 Polymer as the photocurable resin. Fabricated molds were post-cured with UV and their functional surfaces were coated with Tridecafluoro-1,1,2,2-tetrahydrooctyl-1-trichlorosilane (Cat: T2492, United Chemical Technologies, USA). PDMS was mixed with its curing agent at a 5:1 mass ratio and the mixture was degassed. The pre-cured PDMS was then poured on the molds slowly and degassed again to remove the air bubbles trapped between the mold and the pre-cured PDMS. Molds were then placed in a 60°C convection oven for 90 minutes. After curing, PDMS was removed from the mold and holes were punched with a 16-gauge blunt tip

needle (Cat: 5FVG5, Grainger, USA) for inlet and outlet connections. Later, patterned surface of PDMS was cleaned with tape and irreversibly bonded to a 24 mm x 60 mm #2 pre-cleaned cover glass (Warner Instruments, USA) by oxygen plasma bonding (Harrick Plasma Cleaner, 30 seconds, 18 W). The assembly was placed in a convection oven at 90°C for 2 hours to facilitate covalent bonding between the glass and PDMS. Microchannels were stored at room temperature overnight before use and discarded after the experiment.

Scanning electron microscopy (SEM)

Prior to SEM imaging, PDMS parts were cleaned with tape and filtered nitrogen stream. For the cross-section imaging, the PDMS was gently cut using a double edge carbon steel razor blade (Cat: 71933-50, Electron Microscopy Sciences, USA), placed onto double-sided tape that had been adhered to a glass slide, and sputter coated with an approximately 50 Å gold layer. SEM images were acquired using a Jeol JSM 6400 scanning electron microscope, with accelerating voltages ranging from 10 kV to 25 kV and magnification ranging from 40x to 4000x.

Numerical flow characterization

Computational Fluid Dynamics (CFD) simulations were performed using 3D COMSOL (Comsol Inc., Sweden) model to numerically predict the wall shear stress magnitudes at every location within the microfluidic device. Using the laminar flow assumption with Newtonian perfusion media and no-slip condition at the microchannel walls, the Navier-Stokes equation was solved for 2,431,573 elements that were created on the 3D microchannel model with physics-controlled fine-meshing (average mesh size: 20.19 µm). As a result, 3D velocity profiles were obtained across the microchannel and shear rate was calculated. The experimentally measured dynamic viscosity value of the medium at 37°C was used in the simulation, and shear stress

values for each element were calculated by multiplying viscosity and the shear rate using the linear proportionality property of Newtonian fluids.

Microfluidic perfusion setup

All parts used in flow experiments that were in contact with the perfusion medium were autoclaved (121°C, 15 PSI, 30 minutes) and the flow circuit was assembled in a sterile cell culture hood. First, peristaltic pump tubing with stoppers (Cat: EW-06447-13, Cole Parmer, USA) was installed in a peristaltic pump (7524-50 Master flex L/S with 7518-10 pump head, Cole Parmer, USA) and connected to the 1/32" ID 3350 Tygon tubing (Cat: 025871A, Fisher Scientific, USA) with a 1/16" straight polypropylene barbed fitting (Cat: 5121K191, McMaster-Carr, USA) at both ends. The upstream flow tubing was connected to a 50-mL media reservoir and the downstream flow tubing was connected to a custom flow dampener. The outlet of the flow dampener was then connected to the inlet of the bubble trap (Diba Omnifit PEEK with 10 µm PTFE filter, Cole Parmer, USA) using Tygon tubing and quick-turn polypropylene tube couplings (Cats: 51525K291; 51525K141, McMaster-Carr, USA). After these connections were made, the flow circuit was primed with culture media at 3.6 mL/min. The perfusion circuit was visually inspected for trapped air bubbles before connecting the microfluidic device. Finally, the outlet of the bubble trap was connected to the inlet of the microfluidic system by rigid polytetrafluoroethylene (PTFE) tubing (Cat: 5239K23, McMaster-Carr, USA) with a flow rate of 0.2 mL/min. The outlet of the microfluidic device was connected back to the reservoir unit using PTFE tubing and Tygon tubing to complete the assembly of the closed-circuit perfusion system. The assembled perfusion setup was placed in an incubator and the flow rate of the pump was increased to the desired flow rate after 30 minutes.

For live imaging, the perfusion system was set up in the same way but instead of placing the entire system in a cell culture incubator, the microfluidic device was placed in a stage top

environmental chamber (STXF-WSKMX-SET, Tokai Hit, Japan) at 37°C and 5% CO_2. The flow

reservoir and pulsation dampener were kept at 37°C near the microscope stage. For the control

experiments with live imaging, the cell culture media in the microchannels was slowly

replenished using a syringe pump at the flow rate of 0.4 µL/min such that the maximum shear

stress in the microchannels would not exceed 0.1 dyne/cm^2.

Perfusion media viscosity measurement

The dynamic viscosity of the cell culture media was measured with AR2000 plate-cone

rheometer (TA Instruments, USA). An 80 mm diameter cone with the cone angle of 1° was set to

50 µm away from the plate, and data were collected at different steady state shear rate values

ranging from 500 to 2500 s^{-1}. In this way, the Newtonian behavior of the cell culture medium

was confirmed and the average dynamic viscosity values across a large shear rate range were

calculated. All measurements were taken at 37°C ($\pm$ 0.1°C). As a control, viscosity of filtered

deionized (DI) water was measured with the same settings.

Experimental flow characterization

The flow system was set up as described above (without cells), with the microfluidic

device placed on the stage of a spinning disk confocal (Yokagawa CSU-X1, Hamamatsu X2

EMCCD mounted on a Leica DMI6000) and perfused with fluorescent beads (0.2 µm in

diameter, Cat: F8811, Thermo Fisher Scientific, USA) in phosphate-buffered saline (PBS,

Thermo Fisher Scientific, USA) at 0.5 mL/min. After 15 minutes, images were collected with an

exposure time of 30 milliseconds. In the low uniform shear stress region, the entire Z stack was

collected and analyzed to plot the flow profile across the microchannel height. For the flow

visualization experiments, polystyrene green fluorescence beads (1 µm in diameter, Thermo

Fisher Scientific, USA) at 1% w/v were perfused into the microfluidic device and the videos of

the streaklines of the particles were acquired using an Olympus IX83 inverted fluorescence microscope.

Primary endothelial cell culture

Pooled HUVECs (C-12203, Promocell, Heidelberg, Germany) were cultured at 37°C under 5% CO_2 in a sterile humidified incubator in complete growth medium (Endothelial Cell Basal Medium-2 C-22211, supplemented with Endothelial Cell Growth Medium 2 Supplement Pack C-39211, Promocell) and 1X Antibiotic-Antimycotic (Cat: 15240112, Thermo Fisher Scientific, USA). Upon confluency, HUVECs were rinsed with PBS, treated with 0.05% trypsin-EDTA (Cat: 25300062, Thermo Fisher Scientific, USA) for 5 minutes at room temperature, centrifuged at 300 x g for 4 minutes, and gently resuspended in fresh culture medium for a maximum of six passages.

Microfluidic cell seeding and culture

Microfluidic channels were autoclaved (121°C, 15 PSI, 30 minutes) and filled with sterile ethanol. Then, ethanol was replaced with sterile DI water and channels were coated with 50 µg/mL fibronectin (Cat: 10838039001, Sigma Aldrich, USA) at 37°C for 1 hour in a cell culture incubator. HUVECs were suspended at 3 million cells per mL in complete growth media, and 40 µl of this suspension was slowly injected into the fibronectin-coated microfluidic device from the inlet hole using a P200 micropipettor. The excess media around the outlet was immediately cleaned with sterile wipes and the device was placed in a petri dish and kept in the incubator for 30 minutes. Once HUVECs began to adhere to the fibronectin-coated glass slide, 1 mL culture media was added on top of the inlet and outlet ports for overnight culture. Cells were cultured in microchannels for at least 16 hours to confluency to ensure that a uniform HUVEC monolayer was established **(Appendix 3.6)** before using them in the flow experiments. For static control experiments, the same seeding procedure was performed, and the media was replaced daily.

Cell fixing, staining, and endpoint imaging

For all cell fixing and staining procedures, reagents were pipetted into microfluidic channels three times to ensure equal reagent delivery to all cells in different regions of the device. Immediately after the perfusion experiments, cells were fixed with 4% pre-heated paraformaldehyde (PFA) for 15 minutes in the 37°C incubator and stored in PBS at 4°C until immunofluorescence (IF) staining. For IF, all steps were performed at room temperature, within the microchannel. Cells were permeabilized with 0.1% (v/v) Triton X-100 (Cat: T8787, Sigma Aldrich, USA) in PBS (PBST) for 15 minutes and blocked with 10% (v/v) goat serum (Cat: G9023, Sigma Aldrich, USA) in PBST for 30 minutes. Golgi were labeled using mouse anti-GM130 (1:200 dilution, Cat: 610823, BD Biosciences, USA) and goat anti-mouse IgG-rhodamine RedX (1:500 dilution, Cat: 115-295-003, Jackson ImmunoResearch Laboratories, USA). All antibodies were incubated for 1 hour at room temperature. Samples were then rinsed with PBST and nuclei were stained for 10 minutes with 5 µg/mL Hoescht 33342 (Cat: H3570, Thermo Fisher, USA). Imaging was performed using a Nikon A1 confocal microscope on an inverted Nikon TiE platform (Nikon Instruments, Japan).

Live imaging

HUVECs at ~50% confluency were transduced with CellLight Golgi-GFP (BacMam 2.0, Thermo Fisher, USA), 2 µl per 10,000 cells, resulting in 70% transduction efficiency when assayed at 16 hours. Transduced cells were then seeded into the microchannels as described above and the nuclei were stained with 1 µg/mL Hoescht 33342 for 20 minutes before applying flow. Fluorescent and DIC images were acquired every 15 minutes for 6 hours. A modified Nikon Ti-E (Nikon instruments, Japan) was used for these studies. The brightfield illumination system used differential interference contrast with 505 nm transmitted light illumination from a diode illuminator (ScopeLED, USA) at 15 ms exposure time. The fluorescence images used a

Lumencor Spectra X light source (Lumencor, USA). Images were collected with a Teledyne-Photometrics 95B camera (Teledyne-Photometrics, USA). Each image was composed of a field of 28 x 7 3-color images (GFP, Hoescht, DIC) collected sequentially and montaged to create the overview of the entire microfluidic chip. To maximize speed the images were collected using a high speed 5 position dichroic changer (50 ms change time) and high-speed filter wheel (10 ms change time) (FLI instruments, USA). Focus across the entire field was maintained using the Nikon perfect focus mechanism. Images were collected with a 10x 0.5NA plan apochromatic objective and montaged using Nikon NIS Elements software (5.1.01).

Automated analysis of Golgi and nucleus

Analysis of the Golgi and nucleus morphology from fluorescence endpoint images was automated using a custom-written macro for Fiji [133]. Nuclei and Golgi were segmented independently and paired based on the distance between them. Among these pairs, if the center of the Golgi was within the nucleus region, the cell was designated as unpolarized. If the center of the Golgi was outside the nucleus region, the cell was designated as polarized and further characterized according to its orientation with respect to the flow direction. Cells were binned into four categories: upstream-oriented (Golgi-nucleus vector aligned against the direction of flow), downstream-oriented (Golgi-nucleus vector aligned with the direction of flow), right-oriented, or left-oriented. The macro returned the number of cells analyzed, percentage of the cells in each polarization category, the average distance between the centers of the Golgi and nucleus, the average area of the Golgi and nucleus, as well as parameters needed for subsequent statistical analyses. This macro allowed objective analysis of thousands of cells within a set of images in a few minutes. A flow chart detailing this macro can be found in **Appendix 3.7**.

Statistical methods

Every experiment was repeated at least 3 times and the quantitative parameters were calculated for each experiment independently. A two-tailed unpaired student's *t*-test was applied for statistical comparison of the data from two different conditions. The cases where p > 0.05 were considered not significant (ns). Experiments with more than two conditions were analyzed using one-way ANOVA followed by *post hoc* two-tailed unpaired student's *t*-test with Bonferroni correction for pairwise comparison. Categorical data were analyzed by chi-square independence test followed by post hoc adjusted residual test with Bonferroni correction for pairwise comparison.

Results

Overview of the microfluidic device design

To study effects of different flow conditions on EC biology, we designed a microfluidic chip to meet several key performance and manufacturing criteria. (1) The chip allows generation of a wide range of WSS magnitudes and gradients. (2) The flow regimes are stable and robust such that external or internal disturbances do not interfere with the operation of the device. (3) The chip is compatible with high numerical aperture objectives for high content imaging. (4) Chip fabrication does not require the use of sophisticated equipment or specialized facilities.

To generate multiple flow regimes in a single device, our chip contains contiguous microchannel regions with different widths **(Figure 3.1)**. The chip inlet leads to a narrow microchannel with constant width for high uniform WSS, which is followed by an expansion channel **(Figure 3.1a; region 2)** that generates a high-to-medium negative WSSG (i.e., WSS magnitude decreases in the direction of the flow). The next region is constant width for medium uniform WSS **(Figure 3.1a; region 3)** and is followed by an expansion channel **(Figure 3.1a; region 4)** that generates a medium-to-low negative WSSG. We designed these negative WSSG

regions to allow comparison of different average WSS magnitudes within similar WSSGs. The medium-to-low WSSG region is followed by a constant-width region for low uniform WSS (**Figure 3.1a; region 5**), which then leads to two narrow constriction channels (**Figure 3.1a; regions 6 and 7**) that generate a very steep low-to high positive WSSG.

The microfluidic chip is symmetrical, with low (**Figure 3.1a; region 10**), medium (**Figure 3.1a; region 12**), and high (**Figure 3.1a; region 14**) uniform WSS regions in the outlet side of the microfluidic chip functioning as internal controls for their counterparts located on the inlet side of the chip. This duplication allows one to determine whether pressure drop across the microfluidic chip or factors secreted by cells in the upstream regions influences observed phenomena. Moreover, the microchannels with changing width in the outlet side of the chip (**Figure 3.1a; regions 8, 9, 11 and 13**) generate the same magnitude of WSSG as the microchannels in the inlet side of the chip (**Figure 3.1a; regions 2, 4, 6, 7**), but with the opposite sign. Altogether, our design enables a decoupling of effects of WSS magnitudes and gradients through 14 physiologically relevant flow regions.

Region	1	2	3	4	5	6-7	8-9	10	11	12	13	14
Wall Shear Stress Magnitude	High	High-Medium	Medium	Medium-Low	Low	Low-High	High-Low	Low	Low-Medium	Medium	Medium-High	High
Wall Shear Stress Gradient	0	-ve	0	-ve	0	++	- -	0	+	0	+	0
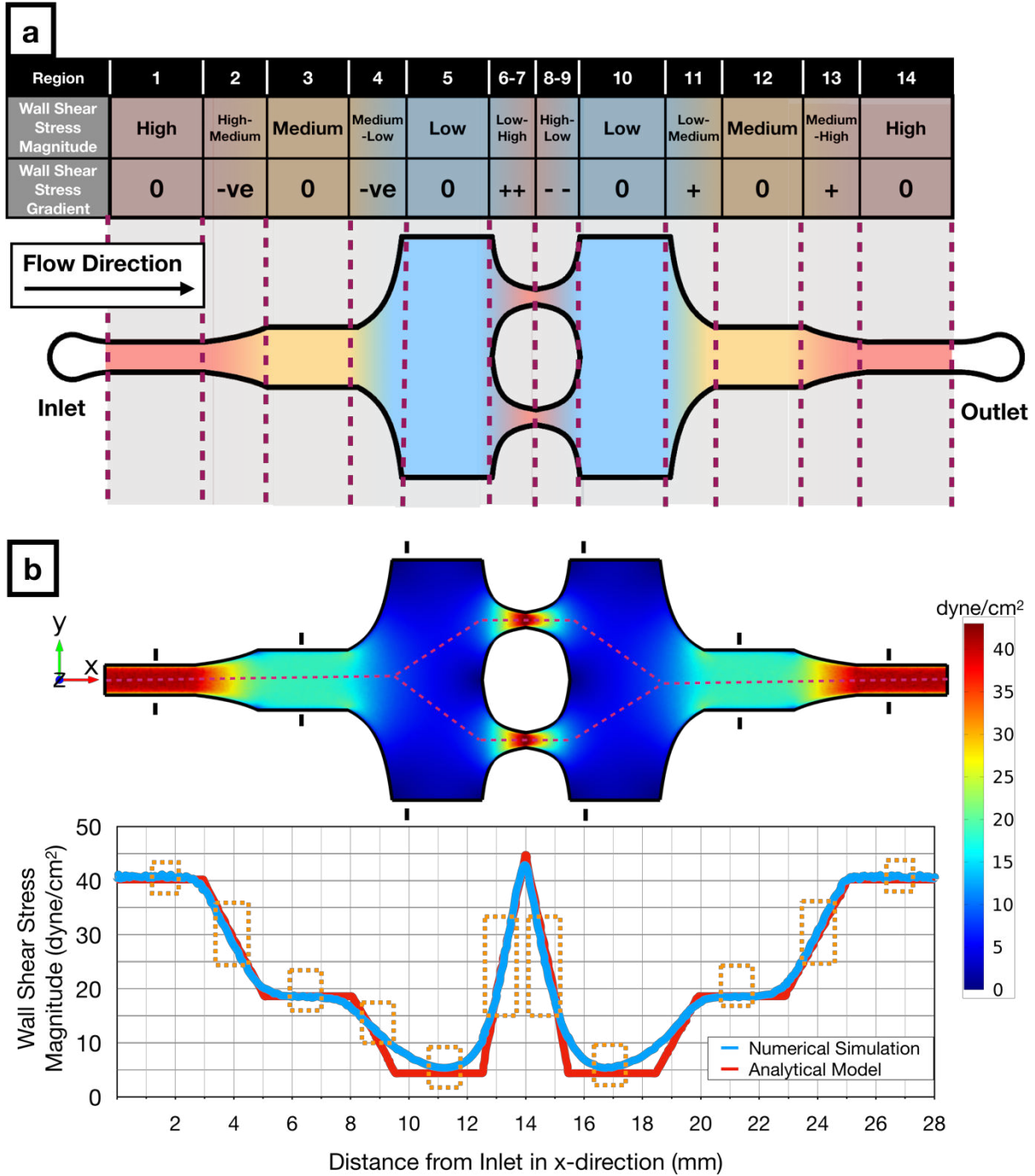
Figure 3. 1. Design and numerical simulation of the novel microfluidic multimodal shear stress generator. **(a)** Schematic of the microfluidic multimodal shear stress generator, indicating 14 regions with different shear stress modalities. **(b)** Computational fluid dynamics simulations (Top) show the distribution of the shear stress across the microfluidic system. The black markers in each uniform shear stress region denote the hydraulic entrance length for those regions. Graph (Bottom) shows both the numerical (blue) and analytical (red) solutions for the magnitude of wall shear stress along the red dashed line (Top). Orange boxes (Bottom) indicate regions that offer predictable flow conditions where analytical and numerical solutions converge to similar results.

82

Analytical and numerical characterizations of the microfluidic device

We designed and fabricated our microfluidic chip according to the following physical criteria. (1) The minimum microchannel width must be at least 200 µm since ECs auto-align in narrower microchannels in response to spatial confinement [194]. (2) Uniform shear stress regions must be longer than hydrodynamic entrance length to ensure fully developed flow (i.e., $\frac{\partial(\cdot)}{\partial x} = 0$). The hydrodynamic entrance length is calculated by

$$L_e = ah \cdot Re \qquad \text{(eq. 3.1)}$$

where a is an empirical proportionality constant equal to 0.08 for microchannels with rectangular cross-section, h is the height of the microchannel, and Re is the Reynolds number. (3) The thickness of the ceiling above the microchannels must be defined to minimize microchannel deformation under pressure-driven flow, based on published design suggestions [195,196]. (4) Abrupt changes in the microchannel width must be avoided to prevent the generation of unwanted recirculation zones and vortices.

To characterize the effectiveness of our design, we performed both theoretical and computational analyses and measured flow velocity profiles in the microfluidic chip. In the microchannel regions with uniform width, the solution of the Navier-Stokes equations for the steady-state laminar flow approximates to Hele-Shaw flow, where the WSS acting on the cells can be calculated as

$$\tau_w = \frac{6\mu Q}{wh^2} \qquad \text{(eq. 3.2)}$$

where μ is the dynamic viscosity of the fluid, Q is the volumetric flow rate, and w is the width of the microchannel. However, especially in high WSS regions where the aspect ratio (h/w) can be as high as 0.2, the sidewalls also contribute to the WSS acting upon the cells. This

sidewall effect can be taken into account by using the empirically-corrected version of the WSS

formula above, which is valid for aspect ratios up to 0.3 [197]. This corrected formula is

$$\tau_w = \frac{2\mu Q}{wh^2}\left(\frac{m+1}{m}\right)(n+1) \qquad \text{(eq. 3.3)}$$

where $n = 2$ and m is defined as

$$m = 1.7 + 0.5\left(\frac{h}{w}\right)^{-1.4} \qquad \text{(eq. 3.4)}$$

On the other hand, microchannel regions with changing width must have linear

streamwise (i.e., along the x axis) WSSGs so that cells in a given region are exposed to the same

gradient slope. The WSS formula for the WSSG can be written as

$$\tau_w(x) = \frac{6\mu Q}{h^2}\frac{(w_i-w_f)}{Lw_iw_f}x + \frac{6\mu Q}{w_ih^2} \qquad \text{(eq. 3.5)}$$

where w_i and w_f are the width of the microchannel at the beginning and the end of the

WSSG region, respectively, while L is the axial length of the WSSG region (**Appendix 3.1**). The

curved microchannel sidewall formula needed to obtain this WSSG can also be written as

$$c(x) = \frac{Lw_iw_f}{2((w_i-w_f)x+Lw_f)} \qquad \text{(eq. 3.6)}$$

Using these formulae, we generated the microchannel sidewall profiles with respect to

the initial and final microchannel widths for the desired WSSG slope. (**See Appendix 3.2 for the**

derivation of these formulae).

Dynamic viscosity (μ) in the WSS formulae above is a material property and its value is

specific to the perfusion medium and its temperature. However, in the literature, it is common to

assume the dynamic viscosity of the perfusion medium is equal to that of water at room

temperature [187,198], whereas other studies have assumed a much higher viscosity [199]. To ensure

our WSS calculations were correct, we measured the dynamic viscosity of the complete EC

growth media that we used in this study and found its value as 0.87 mPa.s at 37 °C **(Appendix 3.3)**.

Using the analytical model and the measured dynamic viscosity, we defined the exact dimensions of each microchannel region **(Appendix 3.4)** which resulted in uniform WSS magnitudes of 40.2 dyne.cm^{-2}, 18.6 dyne.cm^{-2}, and 4.4 dyne.cm^{-2} for high (regions 1 and 14), medium (regions 2 and 13), and low (regions 5 and 10) uniform WSS regions, respectively, at the flow rate of 1.6 mL.min^{-1}. Slopes of the linear WSSGs between these regions had absolute magnitudes of 8.5 dyne.cm^{-2}.mm^{-1} (regions 2,4,11,13) and 17.4 dyne.cm^{-2}.mm^{-1} (regions 6,7,8,9). Numerical simulations yielded similar results across the microfluidic chip **(Figure 3.1b)** with 659 Pa pressure drop across the entire microchannel. Numerical simulations also revealed how far the wall effects [200] propagated into the middle of the microchannel from the sidewalls. For subsequent cellular analysis, we only included the microchannel portions sufficiently far from to the sidewalls where the consistent shear stress values were predicted from analytical flow analysis **(Appendix 3.5)**. Lastly, we marked the hydrodynamic entrance length for each uniform shear stress region **(Figure 3.1b; black markings)** and did not analyze the cells in microchannel regions with potentially undeveloped flow. These data demonstrate that our microfluidic system design can span a 10-fold wall shear stress range and the spatial gradients within this range, covering a majority of physiologically-relevant flow modalities observed in vascular networks[201].

Fabrication and experimental validation of the microfluidic device

Our design flexibly connects all shear stress regions in a single layer with only one inlet and one outlet, facilitating fabrication, operation, and imaging. Using stereolithographic additive manufacturing technology [202], we fabricated the molds for our microfluidic device in less than 4 hours in a fully-automated manner without the need for cleanroom facilities. We used these

molds to rapidly prototype the PDMS (polydimethylsiloxane)-based microfluidic chips that we used throughout this study **(Figure 3.2a)**. However, additive manufacturing can introduce higher levels of surface roughness than photolithographic microfabrication, which might result in fluctuations in WSS. To assess surface roughness, we imaged the microchannels using scanning electron microscopy (SEM). Images revealed surface roughness only at a submicron level **(Figure 3.2b)**, which is less than 0.5% of the microchannel height, introducing variation that would not likely impact the flow perceived by cultured cells. In support of this assumption, micro-particle image velocimetry (μPIV) measurements with fluorescent beads showed parabolic velocity profiles across the height of the microchannels **(Figure 3.2c)**, as predicted by the Hele-Shaw flow model. Therefore, we conclude that stereolithography is a valid rapid fabrication technique able to meet the geometrical requirements of our microfluidic chip designs.

We designed our microfluidic chip to ensure laminar flow, free from flow separation and consequent vortices as well as inertial drag forces. To confirm laminar flow conditions within the microfluidic chip, we used fluorescent beads in the perfusion medium to experimentally visualize the streaklines throughout the microchannels. In these experiments, we observed no flow recirculation or vortex generation, validating our flow model. Furthermore, beads were randomly distributed across the channel width even in high WSS regions, confirming the lack of inertial drag forces. These observations confirm that flow regimes within our device maintain smooth WSS transitions with predictable WSSGs. Altogether, these characterization studies show that our novel microfluidic chip can stably generate different physiologically relevant shear stress modalities in a single device, as predicted by our design calculations.
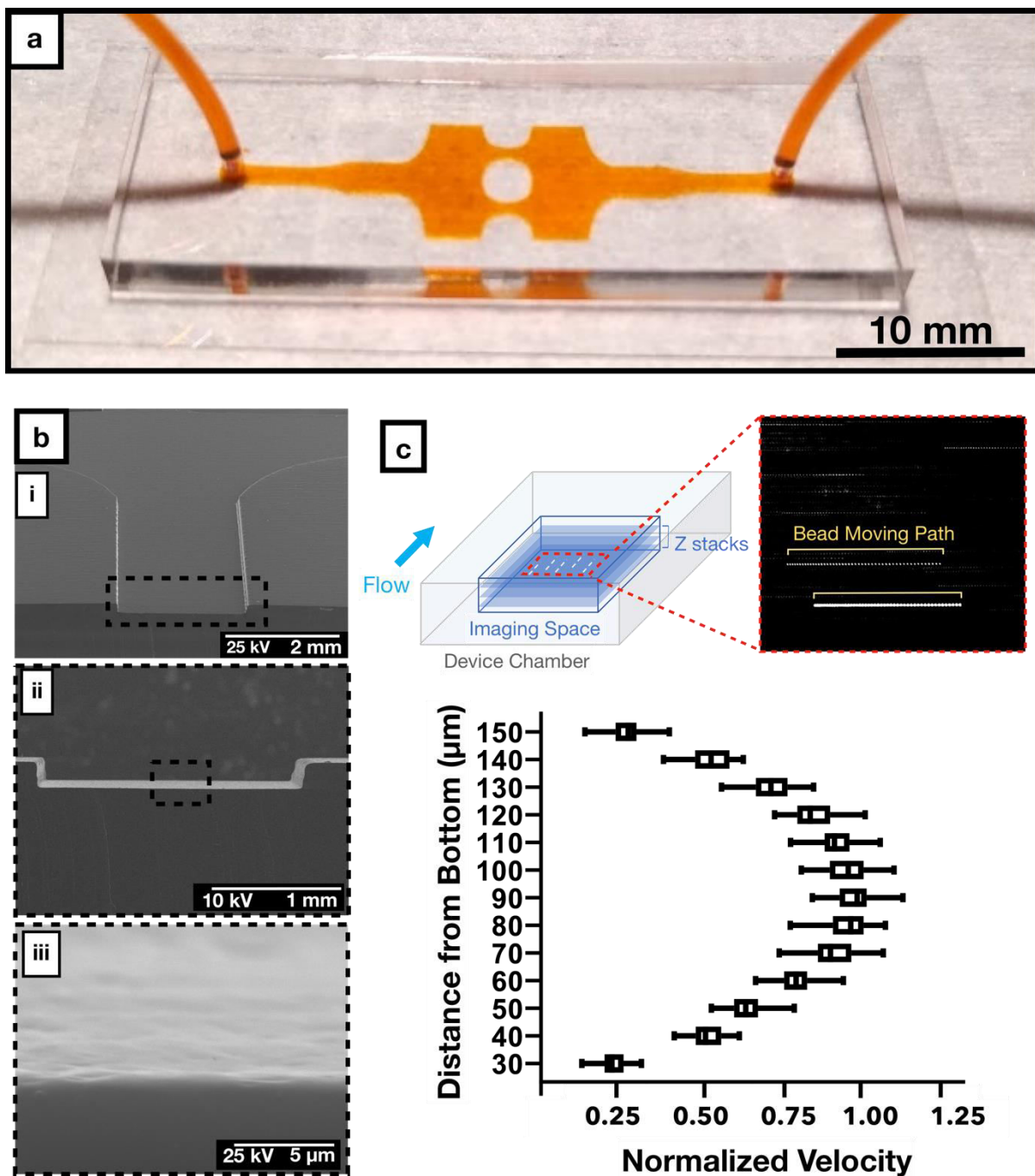
Figure 3. 2. Fabrication and experimental characterization of the microfluidic chip. (**a**) Representative sample of our PDMS-glass microfluidic chip with the inlet and outlet tubing connected. Microchannels were filled with orange dye to facilitate visualization. (**b**) Scanning electron micrograph of the PDMS microchannel with increasing magnification, displaying the surface roughness of the microchannel. (**c**) Flow profile at the cross section of the microfluidic device plotted from micro-particle image velocimetry analysis at 0.5 mL/min. Each dashed line in the inset represents the path for each fluorescence bead in the field.

Perfusion setup and automated analysis of Golgi and nucleus

To assess effects of WSS on EC biology, we created a sterile flow circuit in which a peristaltic pump drew medium from a heated reservoir and passed it through a pulse dampener and bubble filter before entering the microfluidic chip **(Figure 3.3a)**. After seeding HUVECs into the chip, we cultured them in static conditions for the establishment a uniform monolayer across the chip **(Appendix 3.6)** prior to application of different modalities of physiological flows for 24 hours **(Figure 3.3b)**. We then fixed and stained cells for Golgi and nucleus. For all morphological analyses, we only imaged regions of the microfluidic channel where simulation and analytic solutions maintained concordance and where the cells were buffered from gradients due to wall effects. From these images, we quantitatively characterized HUVEC polarity responses to flow using a custom-written macro. This macro **(Appendix 3.7)** automatically paired nuclei and Golgi and measured Golgi-nucleus polarization and orientation of thousands of cells **(Figure 3.3c)** for subsequent statistical analysis.

a Mammalian Cell Culture Incubator

Bubble Filter

37 °C, 5% CO_2, 90% RH

Flow

Stage-top Environmental Chamber

Reservoir

Block Heater

Pulsation Dampener

Peristaltic Pump

Tygon Tubing

Block Heater

Only for Live Imaging   Only for Endpoint Analysis

b
Microchannel Fabrication
Autoclave
Fibronectin Coating
Cell Seeding
Static Culture
Start Flow ⟶ End Flow
Fix and Stain
Imaging

Day 0   Day 1   Day 2   Day 3   Day 4

c
Raw Images   Segmentation   Golgi-Nucleus Pairing   Polarization Map

Nucleus

Golgi

Flow   Right (R)

Upstream (US)   (NP)   Downstream (DS)

(L) Left

Figure 3. 3. Workflow for cell culture experiments and image analysis. **(a)** Schematic of the sterile flow circuit used with the microfluidic chip. The flow circuit can be set up on a microscope stage for live imaging under flow or it can be placed in a cell culture incubator for endpoint analysis. **(b)** Experimental

89

timeline for Golgi-nucleus morphology studies. Human umbilical vein endothelial cells (HUVECs) were seeded inside the microfluidic chip 16 hours before initiating flow and fixed after 24 hours of flow. **(c)** Fluorescent images of nuclei and Golgi were analyzed automatically using a custom-written macro to define and pair each nucleus and Golgi as well as to categorize each cell as nonpolarized (gray) or polarized. Polarized cells were binned into one of four Golgi-nucleus orientation categories: upstream (red), downstream (blue), right (dark green), left (light green), with respect to the direction of flow. Orientation maps outline Golgi (cyan) and nucleus, with nucleus color indicating the orientation of the cell.

Golgi-nucleus polarization is more sensitive than Golgi-nucleus orientation to uniform WSS

The separation of the Golgi and nucleus in the plane of the EC sheet (i.e., Golgi-nucleus polarization) and their alignment with respect to the direction of fluid flow (e.g., Golgi-nucleus orientation) are robust responses to shear stress [156]. In our microfluidic chip under static conditions, approximately 50% of HUVECs were unpolarized and 50% were polarized but not oriented towards a particular direction **(Figure 3.4a, b-i)**. All microchannel regions showed similar results in static conditions, indicating that the microchannel geometries did not alter either the polarization or the orientation of ECs. When we exposed HUVECs to laminar flow for 24 hours, approximately 95% of cells became polarized in all uniform WSS regions, regardless of the WSS magnitude **(Figure 3.4a, b-ii)**. Similar to the static conditions, HUVECs oriented randomly in response to low uniform WSS (4 dyne.cm^{-2}). By contrast, HUVECs oriented upstream in a shear stress magnitude dependent manner at 19 and 40 dyne.cm^{-2}. We obtained similar results from both inlet and outlet sides, indicating that the pressure drop across the microchannels did not influence Golgi-nucleus polarization or orientation. These results suggested that even at 4 dyne.cm^{-2}, which is considered to be the very lowest end of the physiological shear stress range for vascular ECs [203], WSS was sufficient to induce Golgi-nucleus polarization but not Golgi-nucleus upstream orientation.
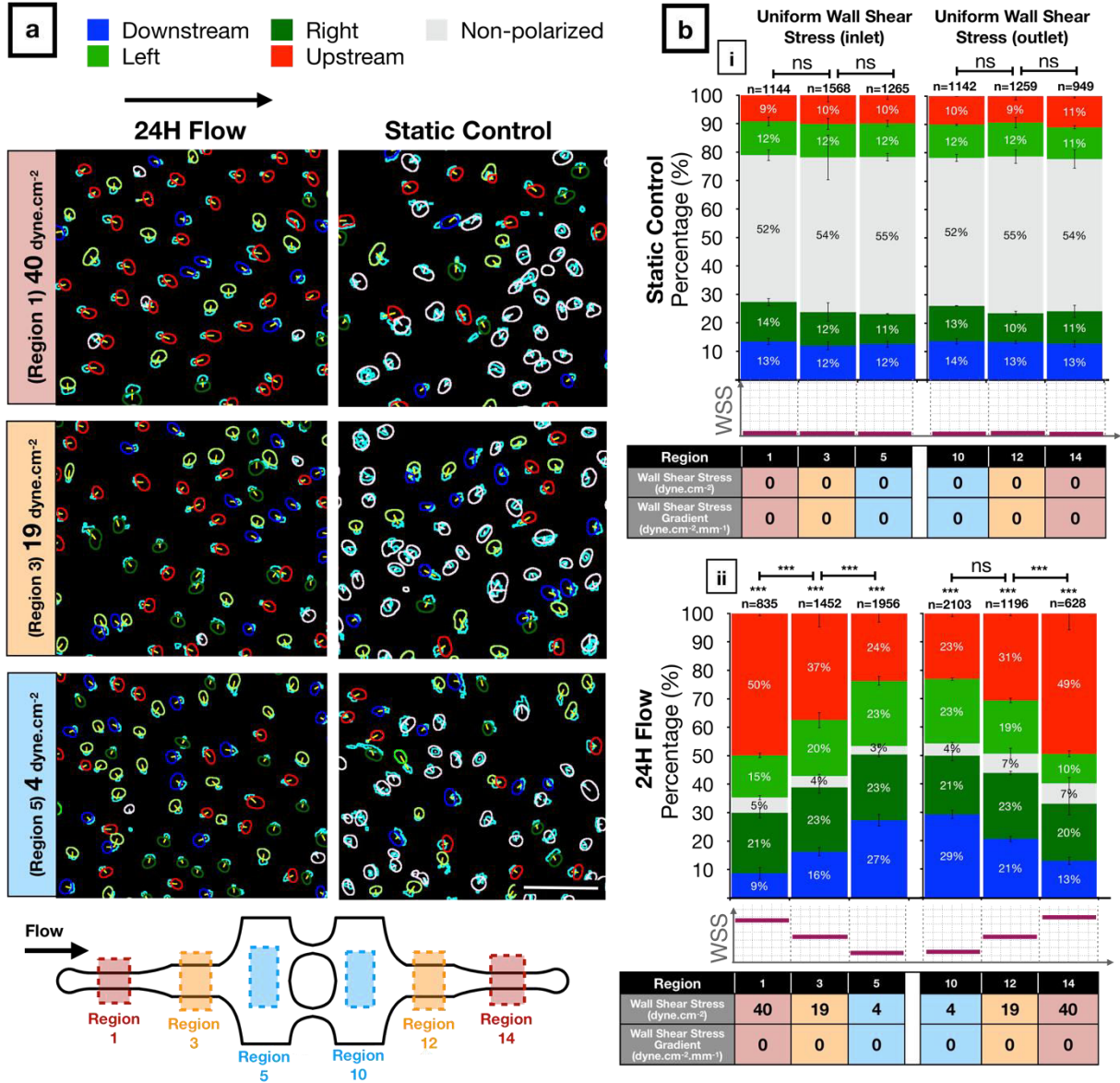
Figure 3. 4. Golgi-nucleus polarization and orientation in response to uniform wall shear stress (WSS). **(a)** Golgi-nucleus polarization and orientation maps from a representative 24-hour experiment, showing HUVECs exposed to high (40 dyne.cm^{-2}; region 1), medium (19 dyne.cm^{-2}; region 3), and low (4 dyne.cm^{-2}; region 5) uniform WSS magnitudes, together with the static controls from the respective microchannel regions. Golgi are outlined in cyan. To indicate Golgi-nucleus orientation, nuclei are outlined in red (upstream), blue (downstream), dark green (right), light green (left), or white (nonpolarized). Scale bar, 100 µm. **(b)** Quantitative analysis of the polarization and orientation responses in (i) static control and (ii) uniform WSS of indicated magnitudes (table below bar graphs), with colors corresponding to orientation category. n = number of cells analyzed in each region, combined over 3 independent experiments. Data are mean ± SEM. Chi-square independence test followed by post-hoc adjusted residual test with Bonferroni correction. ***p<0.0005; ns, not significant at p > 0.01 after Bonferroni correction.

Negative WSSGs promote and positive WSSGs inhibit Golgi-nucleus upstream orientation

Next, we assessed Golgi-nucleus orientation in WSSG regions. In these regions, the percentage of polarized cells increased from ~50% in static controls to ~95% with flow (**Figure 3.5**), similar to results in uniform WSS regions. However, the Golgi-nucleus orientation differed based on the sign and the steepness of the WSSG. More HUVECs were oriented upstream in response to a negative WSSG compared to a positive WSSG of the same slope and average WSS magnitude (**Figure 3.5b**). The difference between numbers of upstream and downstream oriented ECs increased as the negative WSSG steepened (**Figure 3.5b-iii, iv**). For example, in response to a steep negative WSSG (-17 $dyn.cm^{-2}.mm^{-1}$) with average WSS magnitude of 24.5 $dyn.cm^{-2}$, cells oriented upstream similarly to cells exposed to uniform WSS magnitude of 40 $dyn.cm^{-2}$ (**Figure 3.5b, Regions 8 & 9 vs. Figure 3.4c, Regions 1 & 14**). By contrast, positive WSSG had the opposite effect, reducing numbers of upstream oriented ECs. For example, in response to a shallow positive WSSG (8 $dyn.cm^{-2}.mm^{-1}$) with average WSS magnitude of 11.5 $dyn.cm^{-2}$, cells oriented randomly, similarly to cells in uniform WSS magnitude of 4 dyn.cm-2. (**Figure 3.5b, Region 11 vs. Figure 3.4b-ii, Regions 5 & 10**).

To confirm that our observations regarding effects of WSS and WSSGs did not depend on the specific geometry of our microfluidic chip, we modified the width and the length of the device following the design guidelines described above to generate higher WSS magnitudes with steeper WSSGs. HUVECs exposed to WSS magnitudes of up to 60 $dyne.cm^{-2}$ and gradients up to 40 $dyne.cm^{-2}.mm^{-1}$ showed very similar polarization and orientation to cells in microchannels with standard geometry (**Appendix 3.8**). Thus, the effects of WSS and WSSG on Golgi-nucleus polarization and orientation did not depend on the specific microfluidic device design.

Figure legend: %Downstream (blue), %Right (dark green), %Non-Polarized (grey), %Left (light green), %Upstream (red)

a Static Control — Percentage (%)

Region	2	13		4	11		8	6		9	7
Average Wall Shear Stress (dyne.cm⁻²)	0	0		0	0		0	0		0	0
Wall Shear Stress Gradient (dyne.cm⁻².mm⁻¹)	0	0		0	0		0	0		0	0

b 24H Flow — Percentage (%)

Region	2	13		4	11		8	6		9	7
Average Wall Shear Stress (dyne.cm⁻²)	29	29		12	12		25	25		25	25
Wall Shear Stress Gradient (dyne.cm⁻².mm⁻¹)	-9	9		-9	9		-17	17		-17	17

93
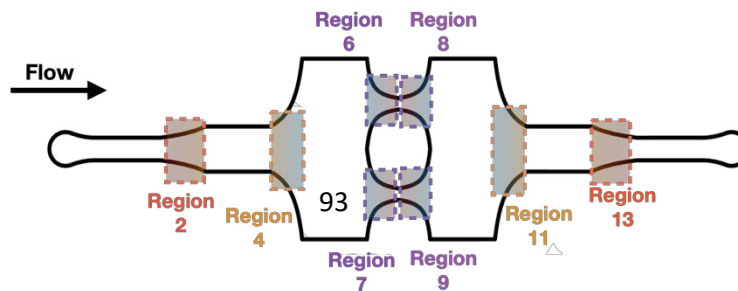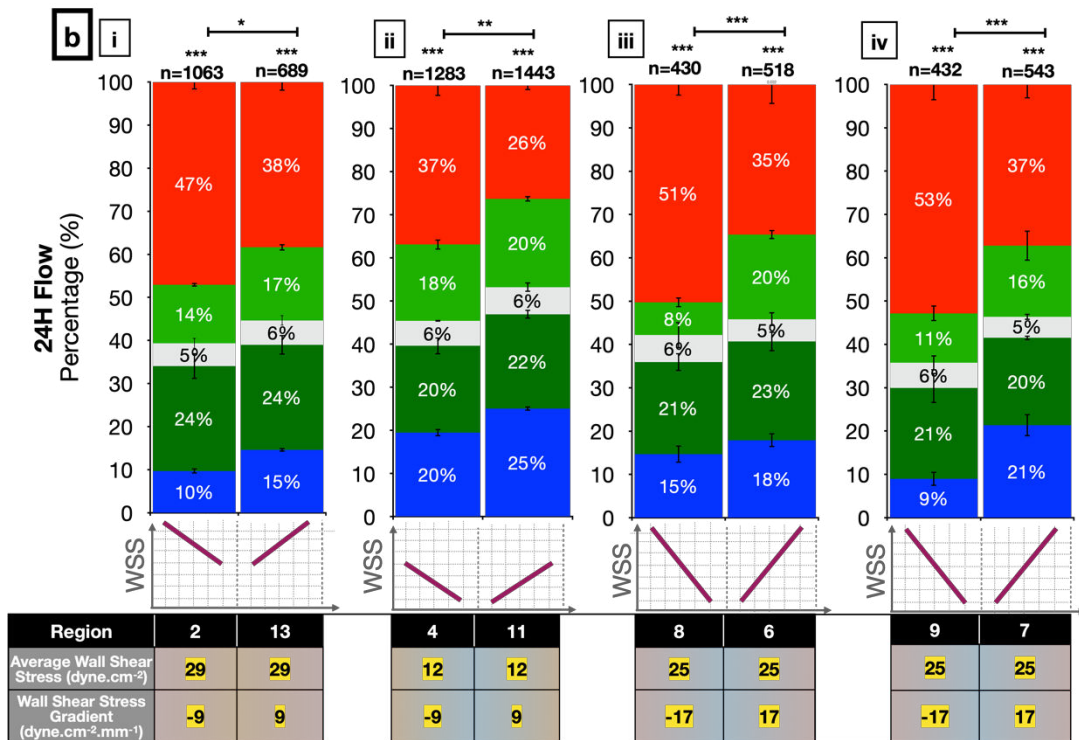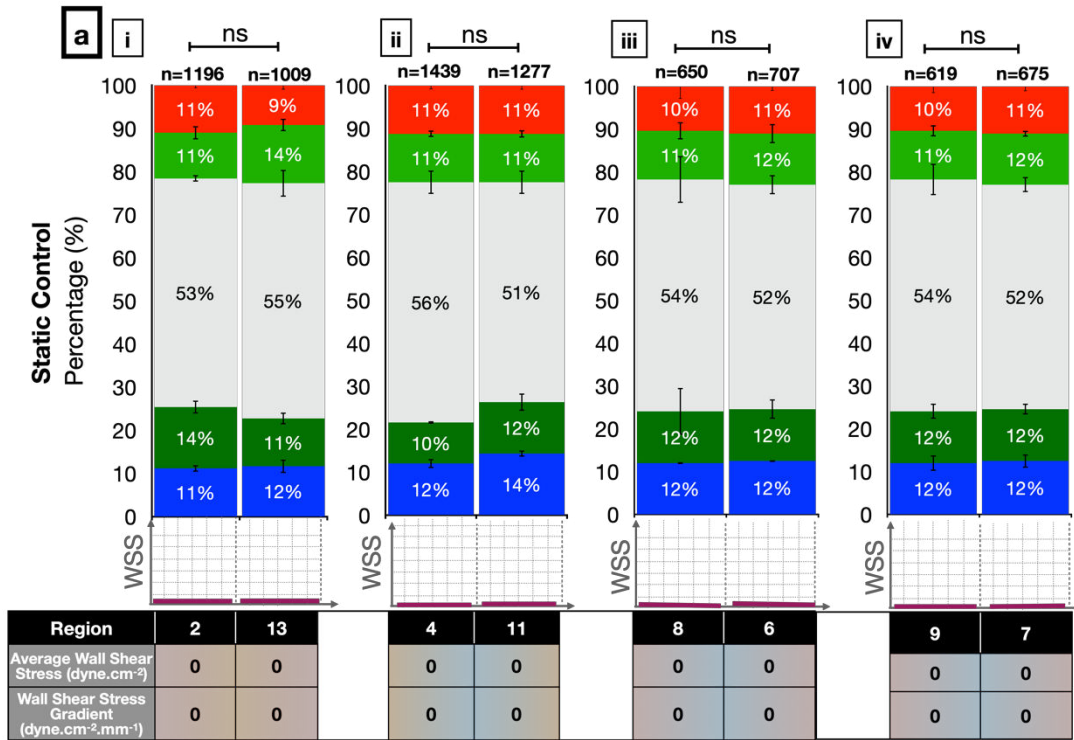
Figure 3. 5. Golgi-nucleus polarization and orientation in response to wall shear stress gradients (WSSG). Quantitative analysis of the polarization and orientation responses in **(a)** static control and **(b)** WSSGs, comparing regions of oppositely orientated WSSGs of low steepness and high average WSS (b-i), low steepness and low average WSS (b-ii), and high steepness and medium average WSS (b-iii, iv), with average WSS and WSSG as indicated the table below the bar graphs. Golgi-nucleus orientation is indicated as upstream (red), downstream (blue), right (dark green), left (light green), or nonpolarized (gray). n = number of cells analyzed in each region, combined over 3 independent experiments. Data are mean ± SEM. Chi-square independence test followed by post-hoc adjusted residual test with Bonferroni correction. ***p<0.0005; **p<0.005; *p<0.01; ns, not significant at p > 0.01.

Golgi-nucleus upstream orientation develops quickly after the onset of the flow

To understand the dynamics of EC responses to WSS, we live-imaged HUVECs in our microfluidic device, with a similar set-up to that described above, but with the microfluidic chip housed in a stage-top environmental chamber **(Figure 3.3a)**. We used Hoescht 3342 dye to label nuclei and baculoviral-transfected GFP-tagged N-acetylgalactosaminyltransferase to label Golgi and imaged across the entire chamber at 15-minute intervals over a 6-hour period. In the static controls, approximately half of the cells were unpolarized while the rest were randomly oriented at all time points **(Figure 3.6a)**. Although individual cells were constantly changing their state of polarization and direction of orientation, the population level response remained the same over time **(Figure 3.6a)**. Upon exposure to flow, the number of upstream oriented cells increased while the number of downstream oriented cells decreased **(Figure 3.6a)**. The ratio of upstream oriented cells to downstream oriented cells (orientation index) increased over time, with the greatest rate of change in the first 3 hours, regardless of shear stress modality **(Figure 3.6b)**. The orientation index increased more rapidly in response to higher WSS magnitude **(Figure 3.6b-i)**, and negative WSSGs resulted in higher orientation index compared to positive WSSGs with the same average WSS magnitude **(Figure 3.6b-ii, iii)**. Overall, results from live imaging experiments supported observations of the Golgi-nucleus polarization and orientation in response

to different physiological WSS modalities after 24 hours of flow and demonstrated that the

Golgi-nucleus polarization and orientation response develops quickly after the onset of the flow.
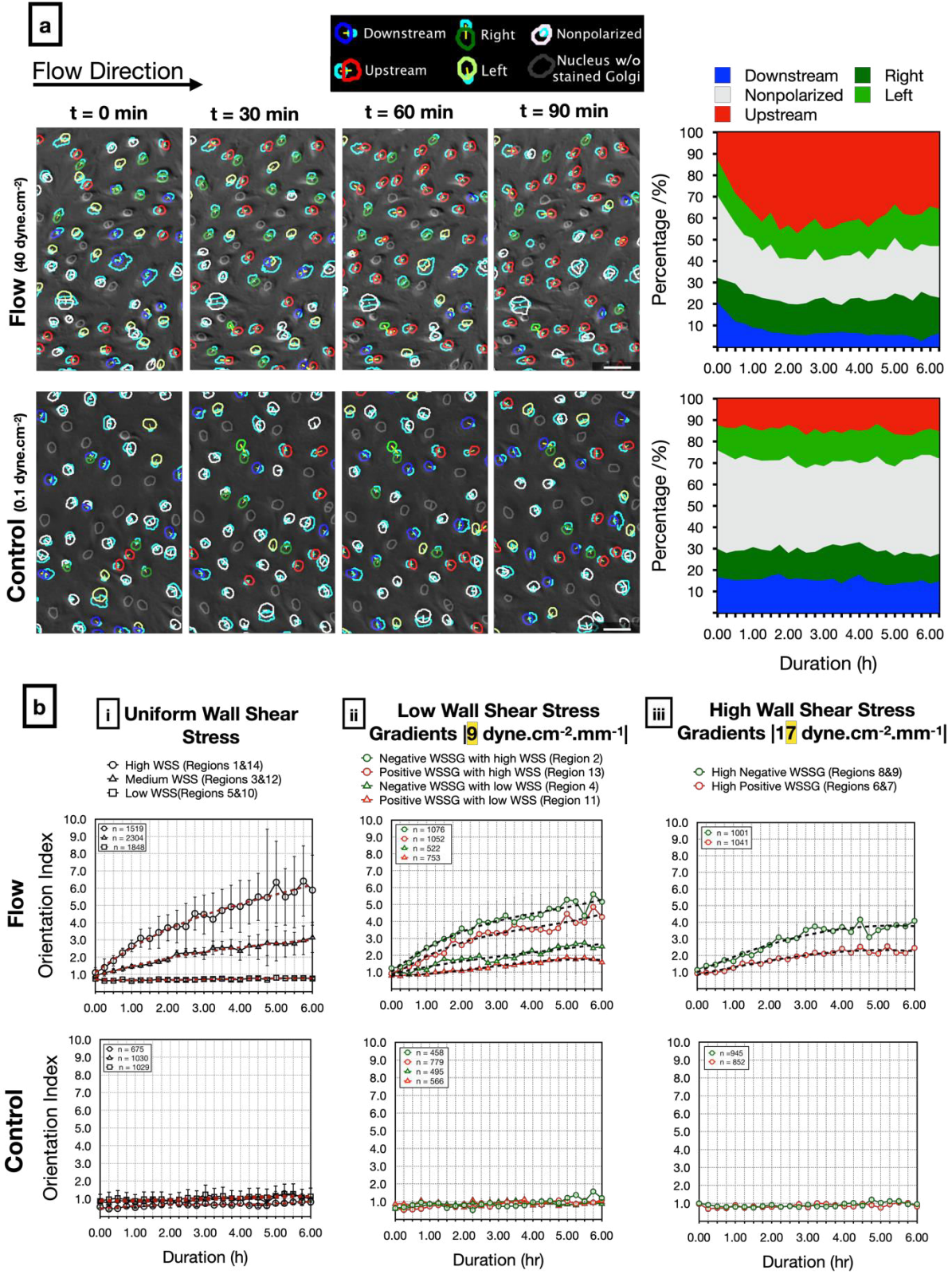
Figure 3. 6. Live analysis of Golgi-nucleus polarity and orientation in response to shear stress. **(a)** Representative images (left) from a time-lapse series of live-stained HUVECs (Golgi, nucleus) exposed to

high uniform WSS (top; 40 dyne.cm^{-2}) or quasi-static conditions (bottom; 0.1 dyne.cm^{-2}). Overlays show Golgi-nucleus orientation maps merged with DIC images. Golgi are outlined in light blue. To indicate Golgi-nucleus orientation, nuclei are outlined in red (upstream), blue (downstream), dark green (right), light green (left), white (nonpolarized), or gray (Golgi not visible). Stacked area plots (right) demonstrate dynamic Golgi-nuclear orientation map over 6 hours of live imaging. Scale bars, 50 µm. **(b)** Orientation index (ratio of upstream oriented cells to downstream oriented cells) of HUVECs exposed to flow (Top) or static (Bottom) conditions over 6 hours, in uniform WSS regions (i), low WSSG regions (ii), and high WSSG regions (iii). n = number of cells analyzed in each group, combined over 4 independent experiments for flow and 3 independent experiments for control. Data are mean ± SEM

ECs respond to flow by altering Golgi and nucleus sizes and Golgi-nucleus distance but these changes are independent of WSS magnitude or gradient

Although we found that the Golgi-nucleus orientation was regulated by WSS magnitude and gradient, the flow-dependent transition from a nonpolarized state to a polarized state did not depend on WSS magnitude or gradient. To investigate EC morphological response to flow, we measured the projected area of the nucleus and Golgi, and the distance between their centers after 24 hours of flow **(Figure 3.7)**. We found that the nucleus and Golgi areas were significantly decreased under flow by 20% and 51%, respectively, compared to static controls **(Figure 3.7a, b)**. On the other hand, the average distance between the Golgi and nucleus centers significantly increased by 34%, from 6.6 µm in static conditions to 8.9 µm under flow **(Figure 3.7c)**. All of these changes were independent of WSS magnitude and gradient.

To evaluate the dynamics of observed increases in Golgi-nucleus distance, we measured the change in this distance over 6-hours from time lapse sequences **(Figure 3.8a)**. Golgi-nucleus distance increased immediately after the onset of flow, reached a peak value within 3 hours, then remained stable and at a similar level regardless of WSS modality **(Figure 3.8b)**. By contrast, in the static control experiments, the Golgi-nucleus distance did not increase, although distances fluctuated over time. Together, these data suggest that Golgi-nucleus polarization is an early and uniform response to WSS. Both the decrease in the Golgi and nucleus areas as well as the

increase in the distance between them contribute to polarization by decreasing their overlap and rendering them as two distinct entities. On the other hand, Golgi-nucleus upstream orientation in response to flow occurs within a similar timeframe in all tested flow modalities, but the extent of this response depends on the magnitude of the WSS and the sign of the WSSG.
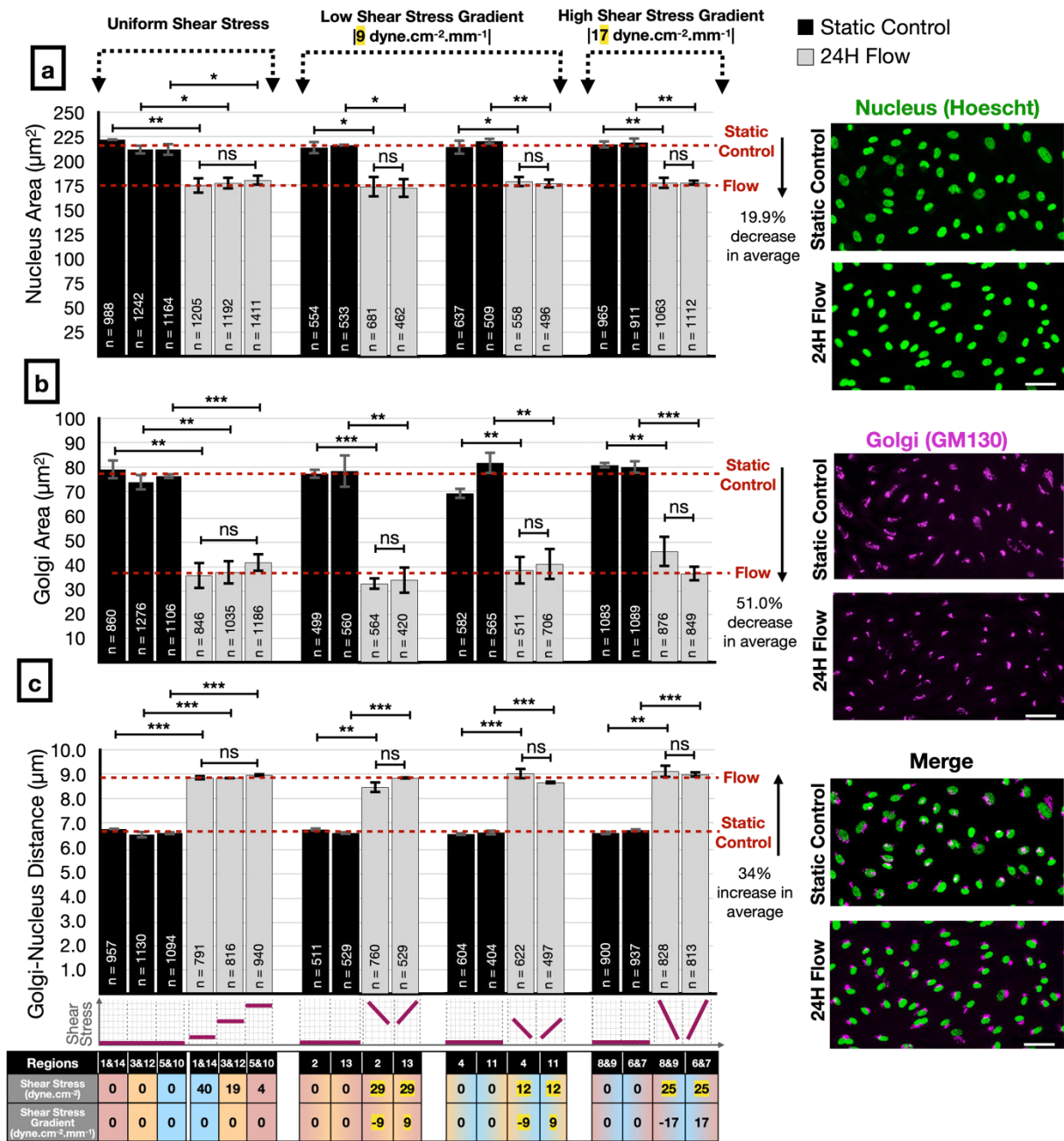
Figure 3. 7. Analysis of Golgi and nucleus sizes and the distance between them in response to different modalities of shear stress. Human umbilical vein endothelial cell (HUVEC) nuclear projected area **(a)**, Golgi projected area **(b)**, and Golgi-nucleus distance **(c)** assayed after 24 hours of static (black bars) or flow (gray bars) conditions, in uniform WSS regions (left), low WSSG regions (center), and high WSSG regions (right) of the microfluidic device. Representative images of Golgi stain (GM130) and nuclear stain (Hoescht 33342) at far right are from region 1. Scale bars, 50 µm. n = number of cells analyzed in each group, combined over 3 independent experiments. Data are presented as mean ± SEM. ANOVA followed by post-hoc two-tailed unpaired student's t-test with Bonferroni correction for pairwise comparison. ***p<0.001; **p<0.01; *p<0.05; ns, not significant at p > 0.05.

Discussion and Conclusion

Our microfluidic chip allows interrogation of effects of a wide range of physiologically relevant shear stress magnitudes and shear stress gradients on EC morphology and behavior in a single experiment. The design strategy generates three different magnitudes of uniform shear stress and six different spatial shear stress gradients in a single unit with a closed-loop flow circuit that has only one inlet and one outlet. With the experimental flow rate of 1.6 mL.min^{-1}, we achieved laminar flow; the maximum Reynolds number inside the chip was ~51, which was more than an order of magnitude lower than the threshold value of ~2300 for turbulent transition. Furthermore, characterization of this chip demonstrated flow stability and validated the analytical and numerical models used to design the system. Importantly, our chip allowed application of a wide range of shear stress without progressive deviation from target magnitudes, demonstrating improved performance compared to other designs [190].

For most microfabrication techniques, fine control of microchannel width is easier than fine control of microchannel height. Moreover, because WSS scales with h^{-2} and w^{-1}, small deviations in microchannel height cause more pronounced deviations in shear stress than small deviations in channel width. Therefore, using varying microchannel widths to generate multiple shear stress modalities both simplifies microfabrication and improves accuracy.

The design of our microfluidic system allowed for long-term cell culture and minimal reagent use. The 200 µm microchannel height kept HUVECs viable for 24 hours in static culture while requiring only ~30 mL perfusion media for application of shear stress. Moreover, the microchannel height was considerably larger than the thickness of the EC monolayer [204], allowing us to ignore effects of dynamic EC height changes in response to shear stress [205].

One of the biggest obstacles to widespread adoption of "lab-on-a-chip" technologies is the complexity of integrating microfluidic chips with bulky fluid handling systems, e.g. the "lab-around-the-chip." [206]. Such obstacles can be removed by miniaturization and on-chip integration of the equipment required to run the microfluidic systems. To this end, we propose future designs that integrate a continuous bubble filter [207] using the multilayer microfabrication capability of stereolithography-based 3D printing **(see Appendix 3.9 for the addition of reservoir and discharge channel)**. Further integration of bulk fluid handling devices with the chip could render this microfluidic system even more accessible to most laboratories.

Results from our microfluidic device are concordant with published findings that ECs adopt upstream orientation after 3 hours exposure to shear stresses above 7.2 dyne.cm^{-2} [154]. With a more detailed analysis of cell polarity and orientation, we found that shear stress as low as 4 dynes.cm^{-2} led to a rapid and dramatic increase in numbers of polarized HUVECs compared to static controls, independent of shear stress magnitude. Analysis of nuclear and Golgi size and position suggested that this increase was likely due to both nuclear and Golgi compaction combined with increased Golgi-nucleus distance, which were similar across all shear stress modalities. Based on reports of compact organellar morphologies in G1-phase hTert-RPE1 cells [208] and reports that flow leads to cell cycle arrest at G1/S transition in HUVECs [209], we speculate that increased polarization reflects flow-mediated cell cycle arrest. However, our current findings are purely correlative; we do not know whether cell cycle arrest is necessary or sufficient for the Golgi-nuclear changes observed here. Future work with our device would allow a more detailed dissection of these processes.

The effect of shear stress gradients on EC morphology and function is not well understood. ECs surrounding a stenosis or atherosclerotic plaque, which are subjected to spatial

WSSGs, adopt a cobblestone as opposed to an elongated morphology [210], and associated EC dysfunction may contribute to plaque rupture [211]. The inhibition of EC alignment, e.g. cell shape change, with positive WSSG and its promotion with negative WSSG have been demonstrated in macroscale flow chambers and T-shaped perfusion channels at supraphysiological shear stress levels [212,213]. Here, we extend these observations on whole cell morphology, demonstrating that a physiologically relevant positive WSSG inhibits Golgi-nucleus upstream orientation whereas a negative WSSG enhances upstream orientation. Whether these changes in Golgi-nuclear polarization and orientation correlate with changes in directional migration or EC function remain to be determined.

Whether Golgi-nucleus polarization and orientation reflect simple mechanical responses to flow, e.g. displacement of the nucleus under a load, as opposed to mechanotransduction-mediated responses, remains unclear. The mechanical hypothesis suggests that the nucleus is dragged by the flow to downstream regions of the cytoplasm [154]. Additionally, the tensile and compressive forces generated along the direction of the flow by the positive and negative WSSGs, respectively, may contribute to the extent of upstream orientation [162,169]. Together, our results suggest that polarization and orientation may be governed by different mechanisms. For instance, polarization may result from mechanotransduction leading to flow-dependent cell cycle arrest, whereas upstream orientation may result from integrating both the physical and biochemical responses to shear stress magnitude and gradient. Further research will be required to systematically test the roles of different flow modalities in triggering mechanosensitive cell polarity signaling pathways such as NOTCH1 [214], PAR-3 [156], and APLNR [158] in shear stress-mediated Golgi-nucleus polarization and orientation.

Chapter 4: Towards High-throughput Microfabrication Without Using Silicon Wafers: Polycarbonate Heat Molding Technique

Introduction

Soft lithography is a prominent technique for rapidly fabricating miniaturized devices with elastomeric materials for a variety of fields including chemistry, material science, and biology[215-217]. Fabrication of these devices conventionally requires casting of pre-cured

elastomers on rigid Silicon-Photoresist (Si-Pr) composite master molds in order to replicate the microfeatures on the Si-PR master mold. This strategy then is frequently used with polydimethylsiloxane (PDMS) for implementing different microfabrication techniques such as replica molding and microcontact printing. Although this fabrication approach has been extremely useful over the last twenty years, challenges associated with master mold fabrication inhibited many groups from pursuing novel microtechnological innovations[218]. Si-Pr composite master molds are conventionally fabricated through photolithography in a cleanroom environment using the SU-8 family of negative photoresists on silicon wafers. This type of fabrication requires user expertise to be successful as most of the steps are manual, are associated with high material and equipment costs, demand specialized facilities that may not be available to everyone, and are challenging for mass fabrication. This creates a barrier for the utilization and adaptation of this technology especially for non-experts and also can cause issues for the commercialization of the products fabricated through this approach[219].

Furthermore, soft lithography has also been challenging because of problems related to the properties of the master molds. The composite nature of Si-Pr master molds results in limited casting lifetime. The differences between the thermal expansion coefficient of the photoresist and the silicon layers result in thermal stress and consequent delamination after a number of heating-cooling cycles[220]. This issue becomes more prominent when thicker photoresist layers with high-aspect-ratio features are present in the master mold. Fabrication of Si-Pr master molds with high-aspect-ratio features also poses additional problems such as the repeatability of the uniformity of spin-coating thickness, challenges associated with developing high-aspect ratio indentations (e.g., trenches), and poor adhesion between crosslinked photoresist and silicon wafers. Furthermore, damage can occur in high-aspect ratio features during the manual peeling

of the cured PDMS from the mold, which is frequently experienced during the PDMS replica molding process. Such issues render Si-Pr master molds fragile and not particularly robust.

To overcome the issues associated with Si-Pr master molds, several other master mold fabrication techniques have been used including mechanical micromilling and 3D-printing. Mechanical micromilling allows for fabrication of high-resolution master molds on a diversity of substrates automatically through Computer Aided Manufacturing (CAM) software and automated stages[221]. However, mechanical micromilling also requires sophisticated tools and expensive equipment, cannot be scaled up for mass production easily, and fabrication parameters are needed to be optimized for each substrate type and geometry. Also, the aspect-ratio of the trenches and microwells are limited due to micro end mill failure[222] along with the inability of the milling process to produce sharp inner corners[221]. Another approach is 3D printing in the additive manufacturing domain, which has been improving its ability to create more complex master mold geometries with automation in shorter time periods[202,223]. However, this approach is limited in its feature resolution, which is far less than photolithography, has surface roughness challenges, and can inhibit the curing of PDMS on 3D printed molds due to residual compounds remaining in the mold structure during the fabrication. In addition, vertical sidewalls with sharp edges cannot be produced by 3D printing due to a scalloping effect[224]. Although the recent advances in additive manufacturing techniques such as the implementation of two-photon polymerization (2PP)[225] for rapid prototyping of microdevices can overcome some issues related to resolution[226], fabrication of large high-aspect-ratio structures still are challenging due to delamination and deformation related to the shrinkage of negative photoresists[227].

Therefore, several techniques have been proposed to copy the existing master molds instead of using time consuming, expensive, and cumbersome master mold fabrication methods

to re-fabricate the damaged master molds or to scale up the fabrication. These copying techniques use PDMS elastomers that have been fabricated through the master molds as elastomeric molds to fabricate rigid copy molds through an additional replica molding process. These approaches include using UV-curable epoxies[228,229], polyurethane (PU)[230], polystyrene (PS)[231,232], and polyvinylsiloxane (PVS)[233] as copy mold materials. Beside the need for specialized equipment and reagent preparation, all of these techniques require the pouring of the pre-cured mold material on the elastomeric PDMS mold, degassing, and curing. The pouring of the mold material and removing the trapped bubbles can distort the features on the non-rigid PDMS mold by applying instantaneous drag force on them especially if the PDMS mold has high-aspect-ratio protrusions such as thin sidewalls and microposts. On the other hand, more conventional techniques such as hot embossing or injection molding, can fabricate very high-aspect-ratio microstructures[234-236]. These processes though require rigid molds to be used and they would not be compatible with elastomeric PDMS molds due to the significant forces that are needed, which would again deform features on the PDMS mold. Instead, rigid Si-Pr master molds are generally directly used in these techniques; however, any issue that may occur during the mold copying process can irreversibly damage the existing Si-Pr master mold[237]. Since master molds are challenging and expensive to fabricate, risking them often would not be preferable to many researchers.

This study introduces a new approach that combines the benefits of these two groups of approaches in order to clone master molds for soft lithography. We used solid polycarbonate (PC) thermoplastic sheets as a starting material and melted them on PDMS molds by heating them above the glass transition temperature (T_g) without applying any external force; this allowed us to avoid distortion of the microfeatures on the deformable PDMS molds. As the PC

melt slowly filled the gap between the PC and the PDMS surfaces, the microfeatures of the master mold transferred to the PC sheet. We applied this polycarbonate heat molding (PCH molding) technique to copy various types of master molds that were fabricated through photolithography, mechanical micromilling, and 3D printing to obtain a variety of microstructures at multiple scales in monolithic PC copy molds. Difficult geometries such as high-aspect-ratio protrusions, holes, and trenches as well as unconventional geometries such as undulated structures with continuously-changing height were successfully fabricated using our technique. The geometries that we fabricated through our PC copy molds were compared to the geometries fabricated through the master molds and they also were tested for their structural integrity. Furthermore, this technique has been used to combine master molds fabricated through different methods into a single monolithic PC copy mold for the fabrication of multilayered complex micro-devices. Here, we describe the details of this method together with a quantitative characterization of the fabricated microsystems, which will enable others to use this technique for their own microfabrication needs.

Experimental Methods
Fabrication of master molds

Three different commonly used microfabrication techniques were used to fabricate master molds with different geometrical features at different scales: Conventional photolithography, mechanical micromilling, and 3D printing. Conventional photolithography techniques were used to fabricate high-resolution silicon-photoresist composite molds using previously established photolithography protocols[238]. Briefly, 3" or 4" test grade Si wafers were spincoated using different negative tone SU8 family photoresists (MicroChem, MA, USA) depending on the height of the features. Photoresist-coated wafers were exposed to 365nm

UV-light through a chrome photolithography mask and uncrosslinked photoresist was removed with SU-8 developer (MicroChem, MA, USA). For the fabrication of high-aspect-ratio features additional steps[8] were used with the conventional protocol to minimize non-uniform coating, delamination, and underdevelopment challenges[221]. Also, mechanical micromilling was used to fabricate microfeatures on a blank PMMA workpiece (McMaster Carr, IL, USA) using tungsten carbide micro end mills[239]. The microtopology geometries were created in SolidWorks 2016 (Dassault Systèmes, Vélizy-Villacoublay, France) and tool paths were generated using Master CAM X7 software in g-code language. In addition, 3D printing was used to fabricate multi-step low resolution master mold geometries through stereolithography. Accura SI 10 Polymer was used in VIPER si2T Stereolithography System (3D Systems, Rock Hill, South California, USA) as a photocurable resin. 3D Computer-aided design (CAD) geometries were sliced into 25µm thick layers and each layer was photo-crosslinked in a high-quality mode setting. Fabricated molds were post-cured with UV to increase their mechanical strength. For all approaches, the master molds were coated with TFOCS for 2 hours in a desiccator prior to PDMS replica molding to prevent adhesion.

PDMS mold fabrication from master molds

Sylgard 184 PDMS (Dow Corning, Midland, Michigan, USA), was mixed with a curing agent at a 5:1 mass ratio in a test tube and degassed with a centrifuge (2000 rpm, 5 minutes). Degassed PDMS was poured onto the master mold and degassed again in a desiccator. PDMS-covered master molds were then baked in a convection oven at 60 °C for 90 minutes so that the curing temperature would not exceed the HDT of the master mold materials. Crosslinked PDMS was allowed to cool to room temperature, separated from the master molds, and trimmed. The

patterned surface of the cured PDMS was cleaned with tape prior to usage. The PDMS parts were then placed in a brass substrate that was covered with an aluminum sheet and coated with TFOCS for 2 hours in a desiccator similar to the master molds to ease the peeling of the PDMS after PCH molding. PDMS parts were then dried in a convection oven at 80 °C overnight until they were used in the PCH molding process.

Polycarbonate sheet separation

Polycarbonate sheets (McMaster-Carr, IL, USA) were cut to a size slightly smaller than the size of the O-ring seals used in the process. Sheet metal snips were used to cut the PC sheets thinner than 3/32" while the thicker sheets were cut using a benchtop drill press followed by sanding. Laser cutting PC sheets was found to be challenging as it had issues with the quality of the cut, fume issues during the process, and even ignition of the material. The cut PC sheets were then baked in a convection oven at 120 °C for 24 hours with their protective films to dehydrate them in preparation for use in the PCH molding process. The protective film was removed from the PC sheet just before using them to ensure that the PC surface was dust-free.

Pneumatic actuation experiments

To run high pressure pneumatic actuation tests on flexible high-aspect-ratio PDMS sidewall structures, gas inlet holes were punched into cured PDMS parts using blunt needles and the device was sealed by covalently bonding it to a pre-cleaned 24 × 60 mm #2 glass slide (Warner Instruments, Cincinnati, USA) using air plasma (Harrick Plasma Cleaner, 30 seconds, 18 W). The assembled device was baked at 80 ^{o}C in a convection oven for 1 hour and left at room temperature for 1 day to establish Si-O-Si covalent bonds between the glass slide and the patterned surface of PDMS. Tygon 3350 Silicone tubing (1/32" inner diameter, Saint-Gobain,

France) with fittings was used to connect the microfluidic device to a high pressure compressed air tank. A digital diaphragm pressure gauge (Cole Parmer Instrument Co., IL, USA) was added to the gas circuit next to the microfluidic channel to determine the pneumatic pressure. The deflection of deformable PDMS sidewalls were imaged under different levels of pneumatic actuation using a microscope (Zeiss Axiovert 200) equipped with 20x objective and Differential Interference Contrast (DIC).

Scanning electron microscopy (SEM)

SEM images were acquired for qualitative and quantitative assessment of the PDMS parts fabricated with the master mold approach as well as the PCH molding approach using Jeol JSM 6400 scanning electron microscope. Prior to SEM imaging, PDMS parts were cleaned with tape and filtered nitrogen stream. For the cross-section imaging, the PDMS parts were gently cut using double edge carbon steel razor blades (Electron Microscopy Sciences, PA, USA). PDMS parts were then placed onto double-sided tape, which was adhered to a glass slide and sputter coated with an approximately 50 Å gold layer. Acceleration ranging from 10 kV to 25 kV was used to acquire SEM images with magnifications ranging from 40x to 4000x. Quantitative analyses of SEM images were conducted using ImageJ.

Atomic force microscopy (AFM)

Sub-micron standing-sinusoidal wave patterns fabricated from PC copy molds and holographic diffraction gratings (Edmund Optics, NJ, USA) were quantitatively characterized by AFM using the Asylum Research MFP-3D Infinity system. Standard tapping AFM tips for surface characterization had a full cone angle of 40° and tip radius of < 8 nm. The AFM cantilever had a force constant of 40 $N.m^{-1}$ and resonance frequency of 325 kHz (NanoAndMore, CA, USA). Each sample was scanned in 5 different locations where each location spanned 25 μm^2 area with 256

x 256 resolution. Gwyddion software was used for the quantitative analysis and the visualization of the AFM data.

Results

Developing the polycarbonate heat molding (PCH molding) approach

The PCH molding process described here involved using PDMS elastomers fabricated through various master molds as an elastomeric mold to copy the master mold geometry into a PC copy mold **(Figure 4.1a)**. We accomplished this by first placing the PDMS elastomers on a brass plate that was covered with an aluminum sheet together with a rectangular cross-section O-ring. We coated the entire system with tridecafluoro-1,1,2,2-tetrahydrooctyl-1-trichlorosilane (TFOCS, T2492, United Chemical Technology, PA, USA) followed by drying in a convection oven. Similar to many polymers, PC is hygroscopic and it absorbs moisture from atmosphere[240]. This absorbed moisture is likely to cause the formation of bubbles throughout the PC sheet when it is heated above the boiling temperature of water. Therefore, the PC sheets were dried below their T_g prior to using them in the PC heat molding process. Since PC absorbs moisture very quickly[241] they were used in the PCH molding process immediately after drying. The dried PC sheet was placed on top of the PDMS mold and then heated above the T_g of PC until the melted PC filled all of the microfeatures on the PDMS mold **(Figure 4.1b)**.

PC sheets used in the fabrication were greater than the thickness of the PDMS mold to ensure that the PC covered the entire PDMS elastomeric mold once it melted. The T_g of PC is 147 ^{o}C and the viscosity of PC decreases rapidly as the temperature exceeds T_g. Therefore, it was desirable to set the process temperature as high as possible to more easily fill the PDMS molds with a less viscous PC melt. However, there is a limit to this. The thermal degradation

temperature of the PDMS, which is ~280 $^{\circ}$C[242], creates an upper limit for the process

temperature. For this reason, the process temperature was set to 230 $^{\circ}$C since further increases

in temperature will not substantially decrease the viscosity of the PC[243] and the risk for PDMS

thermal degradation is very low relative to its reported thermal degradation temperature

(Figure 4.1c). Under these conditions, 4 hours of baking was sufficient to copy any geometry we

tested into a PC sheet although lower baking durations were sufficient for simple low-aspect-

ratio geometries. After the baking, the samples naturally cooled down to room temperature for

1 hour, allowing the PC sheet to re-solidify. The O-ring and the brass plate were removed

followed by peeling off the aluminum sheet and PDMS part. The remaining PC copy mold then

had the same surface topology as the original master mold as well as the same thickness as the

PDMS part used process. Thus, it could be used as a copy mold to produce more PDMS

microsystems through replica molding **(Figure 4.1d)**. The PC copy mold was coated with TFOCS

similar to the master molds to ease the peeling especially for high-aspect-ratio geometries.

However, PC molds with most of the geometries do not need TFOCS as PC does not adhere to

cured PDMS thanks to the significantly lower surface energy of PC[244] compared to

monocrystalline silicon[245]. The pre-cured PDMS can be baked in PC copy molds up to the heat

deflection temperature (HDT) of PC which is 130 $^{\circ}$C without warping. For a better comparison

of the PDMS parts fabricated through master molds and PC copy molds, we cured PDMS in the

PC copy molds with the same process as in the master molds.
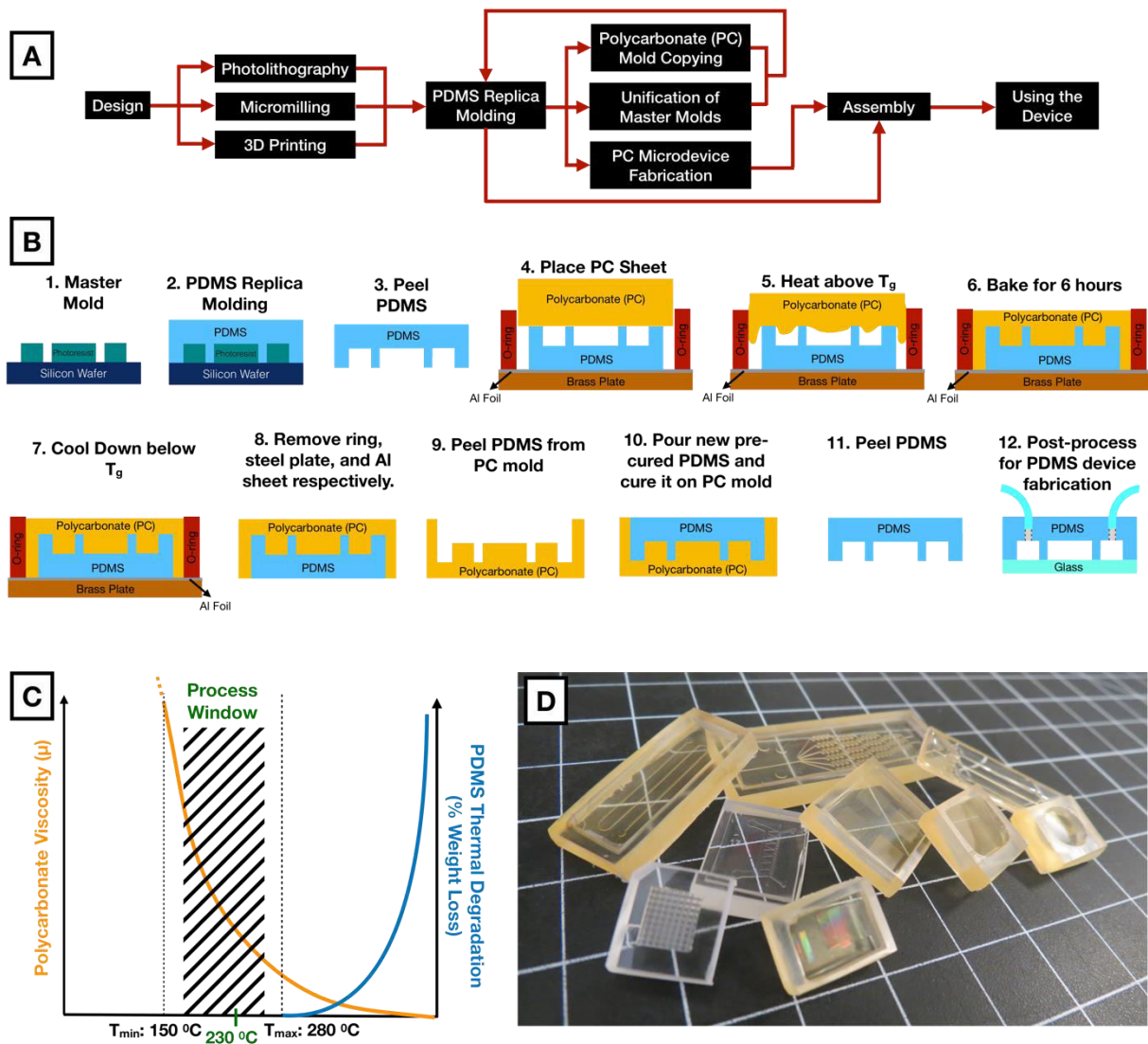
Figure 4. 1. Polycarbonate (PC) copy mold fabrication. **(a)** Microfabrication flow chart. Polycarbonate heat molding can be used after PDMS replica molding to copy the master molds without any risk of damaging them, for further soft lithographic fabrication. Alternatively, the PC parts can be used as thermoplastic devices, directly. **(b)** Schematics of the polycarbonate heat molding process for copying master molds. PDMS microsystems fabricated through master mold (#1) were used as a mold to copy the master mold geometry into PC copy mold (#9). A Si-PR master mold is shown as an example in the schematic; however, other master mold types were also used similarly. **(c)** PC heat molding process temperature selection criteria: Temperatures high enough to render PC viscous enough but low enough to not to cause PDMS to thermally degrade. Therefore, 230 ^{0}C was selected as the process temperature. **(d)** Examples of the fabricated PC copy molds with various geometries at different scales where the mold sizes can be tens of centimeters with sub-micron features (grids are 0.5 inch x 0.5 inch).

Polycarbonate heat molding of common microfeatures

To the test the copying capabilities of sharp-edged geometries, vertical sidewalls, and the filling efficiency of small holes, Si-Pr master molds with low-aspect-ratio common geometries were copied at different scales using our PCH molding approach. SEM images acquired from the PDMS microdevices fabricated through the PC copy molds show that the standard geometries such as triangles and circles at the millimeter scale were successfully copied into PC molds by maintaining the vertical sidewalls and the sharp edges both for the indentations and protrusions **(Figure 4.2a, b)**. Furthermore, smaller 100 μm wide microchannels with serpentine configurations, which have been used in micromixer applications[246], were copied with high fidelity **(Figure 4.2c)**. Then, various geometries at smaller scale were used with PCH molding technique. Arrays of 40 μm diameter low-aspect-ratio microposts that are commonly employed for circulating cancer cell isolation and enrichment[247,248] were successfully copied into PC copy molds from Si-Pr composite master molds **(Figure 4.2d)**.

A more challenging task for the PCH molding technique was copying microscale indentations into PC copy molds. The low viscosity of pre-cured Sylgard 184 PDMS (3.5 Pa.sec) is helpful for replicating microwell geometries during the PDMS replica molding process. However, copying these structures into PC sheets required filling these microwells with PC melt which has zero-shear viscosity of approximately 15,000 Pa.sec at 230 °C[243], which is three orders of magnitude more viscous than the pre-cured Sylgard 184 PDMS. 4 hours of baking time at 230 °C allowed us to copy these geometries even in the absence of externally applied force. Consequently, PC copy molds of circular microwell arrays that are 10 μm in diameter **(Figure**

4.2e), which are frequently used in single cell analysis[249] as well as the elliptical microwells of

similar dimensions **(Figure 4.2f)** for 3D cellular microniches[250] were successfully fabricated.
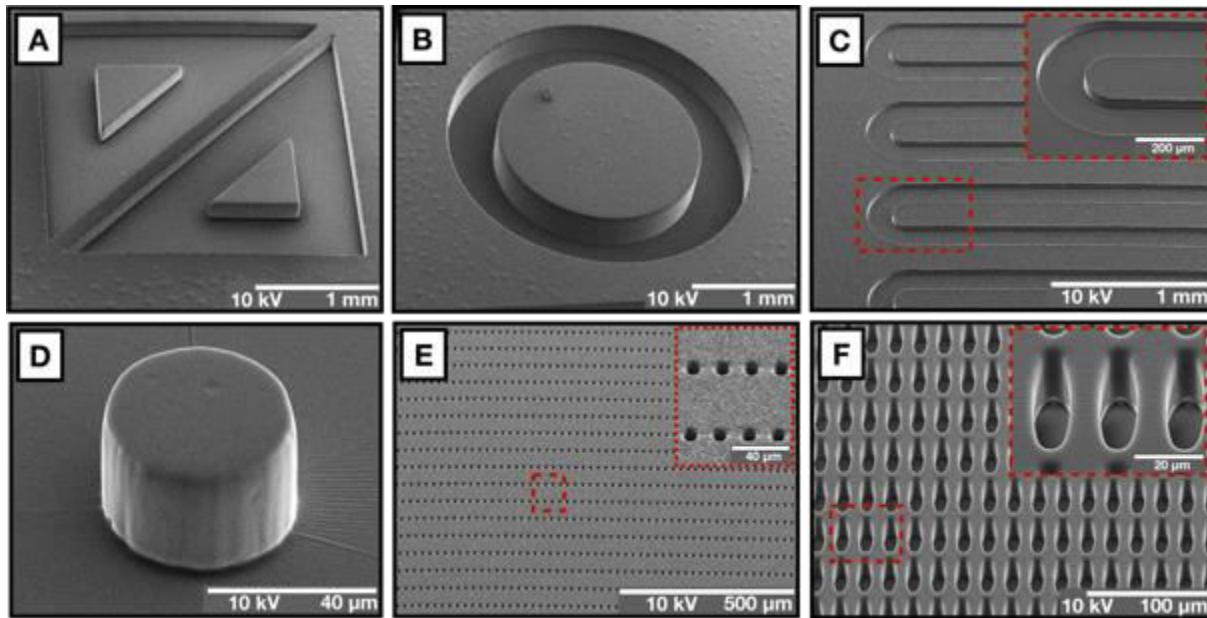
Figure 4. 2. Scanning electron microscopy (SEM) images of various PDMS microsystems with common geometries at different scales fabricated using our polycarbonate heat molding approach. **(a)** 2 mm across triangular test geometries, **(b)** a circular test geometry that is 3 mm in diameter, **(c)** 100 µm wide serpentine microchannels, **(d)** a 40 µm diameter micropost, **(e)** 10 µm diameter circular microwell arrays, **(f)** elliptical microwell arrays with 10 µm in the short axis and 30 µm in the long axis are all fabricated through polycarbonate copy molds successfully.

Fabrication of high-aspect-ratio protrusions and trenches

Geometries that have high-aspect-ratio microfeatures are frequently used in lab-on-chip

applications to take advantage of the elastomeric nature of PDMS. Such geometries can deform

easily and predictably upon the application of external force enabling the development novel

force sensors and microscopic mechanical actuators. This approach has been leveraged to study

biomechanical properties of single cells[251,252], to build mechanically-active organ-on-a-chips

such as lung-on-a-chip[253] and gut-on-a-chip[254], and to apply mechanical stimulation to cells[255]

and model organisms[8]. However, the repeatability of the fabrication of the master molds for

such high-aspect-ratio structures remains a challenge in soft lithography[122] regardless of the master mold fabrication technique due to the inherent problems associated with them as mentioned above. These challenges are exacerbated when continuous high-aspect-ratio microscale features cover large areas.

Duplication of the master molds with such geometries into a copy mold may be the most feasible solution for improving the limited lifetime of master molds and to increase the throughput of the fabrication. However, the techniques that are proposed to duplicate the original master molds either used the application of high contact force[256], rigid intermediate mold[234] or pouring of liquid plastics, which are then cured onto the PDMS molds[230-232]. Although, these techniques are beneficial for some applications, they are not well suited to the fabrication high-aspect-ratio slender geometries such as micropost arrays and thin sidewalls because of the issues with deflection of the high-aspect-ratio microfeatures during the pouring and forced-degassing processes which would cause instantaneous local forces on the slender PDMS microstructures. In addition, polyurethane solutions that are used to fabricate copy molds cannot be degassed after pouring them on PDMS molds due to their limited pot life[230], which almost guarantees the creation of air pockets in high-aspect-ratio indentations.

PC heat molding does not require the application of external forces such as in hot embossing but it still begins the process with a solid PC sheet, which slowly melts into the PDMS mold and penetrates into the high-aspect-ratio features without applying external force. Thus, the PCH molding approach to copy various master mold geometries with high-aspect-ratio protrusions and microchannels at different length scales can be done without deflecting the high-aspect-ratio features **(Figure 4.3)**. For this, Si-Pr master molds with high-aspect-ratio

116

concentric microchannel arrays that were 50 µm wide and 300 µm high (aspect ratio of 6) were

copied into PC copy molds. The melted PC penetrated into these deep trenches and the PDMS

parts fabricated through PC copy molds had intact vertical sidewall structures throughout the

pattern **(Figure 4.3a)**. At lower scales, 5 µm wide and 10 µm high straight microchannel arrays

(with an aspect ratio of 2) were fabricated, which are shown in the SEM images in **Figure 4.3b**.

Furthermore, high-aspect-ratio micropost arrays that are 2.5 µm wide and 10 µm high (aspect

ratio of 4) were copied with PCH molding. PDMS micropost arrays fabricated through PC copy

molds did not appear to deform when compared to PDMS post arrays fabricated through Si-Pr

master molds **(Figure 4.3c, top)**. However, it was noted that the bases of the PDMS micropillars

fabricated through the PC copy mold approach were more rounded than the PDMS micropillars

fabricated through Si-Pr master molds. This may be due to insufficient filling of the base regions

by PC melt at this low length scale.

The quantitative comparison of the dimensions of the micropillars revealed that

micropillars fabricated through the PC copy mold were consistently larger where their height

and diameter has been measured to increase by 5.4% and 4.95%, respectively. On the other

hand, the error bars showing the distribution of the height and diameter throughout the

pattern did not substantially change, implying that the PC heat molding process did not

introduce any further dimensional fluctuation but rather shifts the dimensions of the

micropillars isotropically **(Figure 4.3c, bottom)**. High-aspect-ratio straight sidewalls that were

50 µm wide and 350 high (aspect ratio of 7) were also fabricated through the PCH molding

approach (**Fig 4.3d**). Slender sidewall structures were not deformed during the heat molding

process. The other master mold copying techniques that were tested either deformed the

sidewalls or the copy mold material stuck and led to partial or total rupture of PDMS sidewalls

(**Appendix 4.1**). The quantitative comparison of the PDMS walls fabricated through PC copy

mold and the ones fabricated from the Si-Pr master mold revealed a similar dimensional shift in

the feature dimensions. The high-aspect-ratio PDMS sidewalls fabricated through the PC copy

molds had 3.10% increase in sidewall thickness and 3.77% increase in the central microchannel

width without introducing further variation to the feature dimensions (**Figure 4.3d, bottom**).
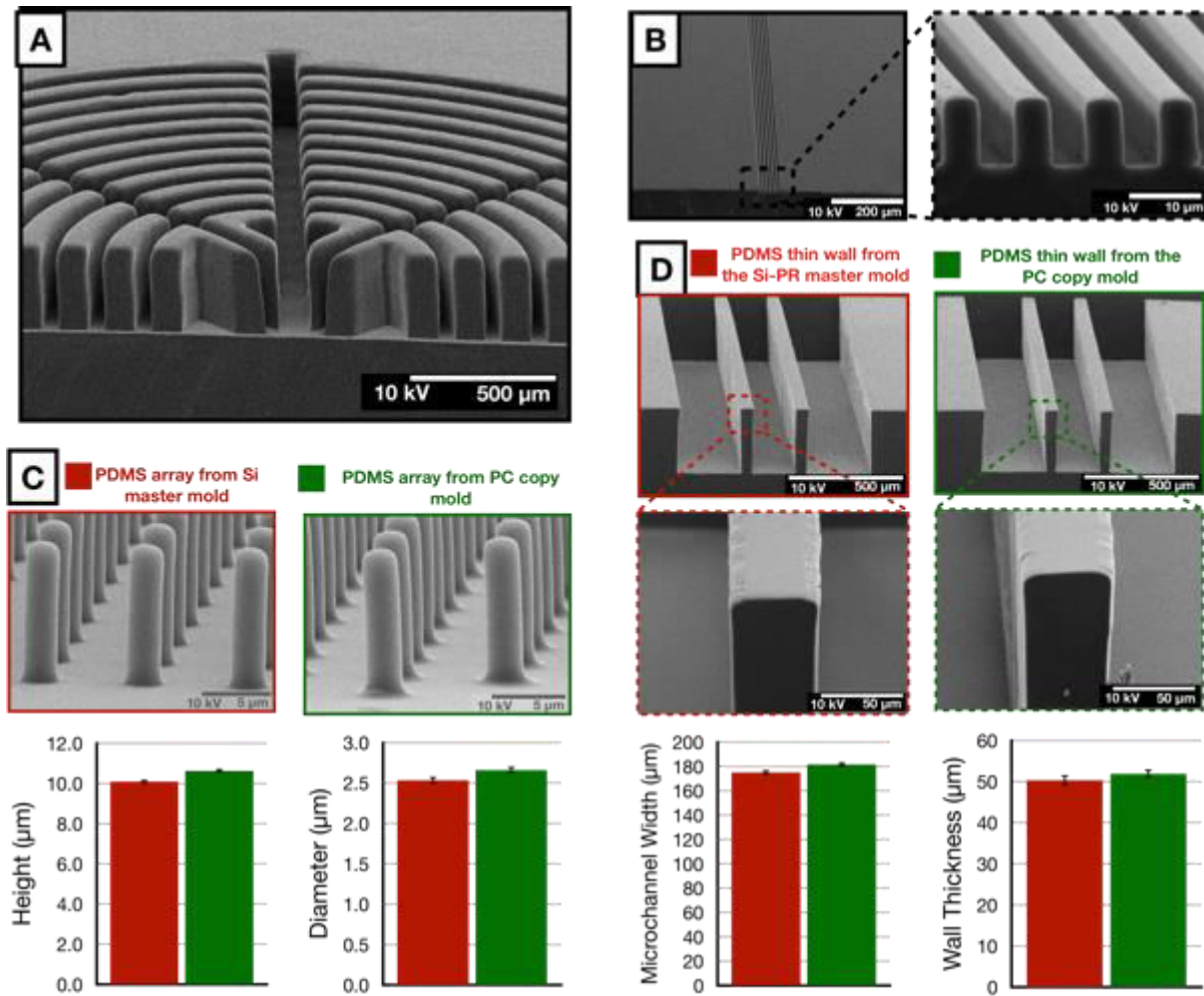
Figure 4. 3. High aspect ratio PDMS microstructures fabricated through polycarbonate heat molding approach. (**a**) Concentric high aspect ratio (AR) microchannel arrays with 300 µm height and 50 µm width (AR=6). Fabrication of these PDMS geometries required successful filling of high-aspect-ratio circular microgrooves with melted polycarbonate during the mold copying process. (**b**) Parallel microchannel array with 5 µm width and 10 µm height (AR=2). (**c**) Quantitative comparison of 10 µm high 2.5 µm diameter high-aspect-ratio (AR=4) PDMS micropost arrays fabricated through the Silicon

118

master mold (red) and polycarbonate copy mold (green), respectively. (Bar graphs) PDMS micropost arrays fabricated through the PC copy mold have a 5.40% increase in height and 4.95% increase in diameter without changing the variation of the micropost dimensions. **(d)** Visual comparison of high-aspect-ratio PDMS sidewall arrays with 350 µm height and 50 µm width (AR=7) fabricated through silicon master mold (red) and PC copy mold (green). Insets show the critical top surface of the walls in more detail where the flat top surface was preserved in the PDMS parts fabricated through the PC copy molds. (Bar graphs) High-aspect-ratio PDMS sidewalls fabricated through PC copy mold demonstrated a 3.10% increase in wall thickness and 3.77% increase in the width of the central microchannel without affecting the variation of the feature dimensions.

High-aspect-ratio geometries can be used as deformable elements actuated by hydraulic or pneumatic pressure[8,257] and it is important to have the tips of the deformable elements flat since these regions are bonded to flat substrates like glass to seal the device. Rounded top surfaces reduce the effective bonding area and would lead to leakage upon the application of the actuation force **(Figure 4.4a)**. Therefore, PDMS sidewall structures fabricated through the PCH molding approach were tested against increasing pneumatic pressures to evaluate the functionality of the microfluidic channels. As pneumatic pressure was applied to the microchannels at either side of the central channel, the PDMS sidewalls deformed inwards and they did not leak or detach up to pressures as high as 40 PSI **(Figure 4.4b)**. High magnification SEM images show the flatness of the tip of the PDMS sidewalls compared to the PDMS sidewall fabricated using the Si-Pr master molds **(Figure 4.3D, insets)** which match the experimental tests. Another master mold copying technique that we examined failed in the pneumatic pressure testing due to the detachment of the PDMS walls from the glass slides upon the application of pneumatic pressure as low as 1 PSI **(Appendix 3.2A)**. SEM images of the sidewall structures of the PDMS sidewalls fabricated through this technique showed rounded tips **(Appendix 3.2B)**, which was likely why these PDMS sidewalls failed during the pneumatic actuation test.

119
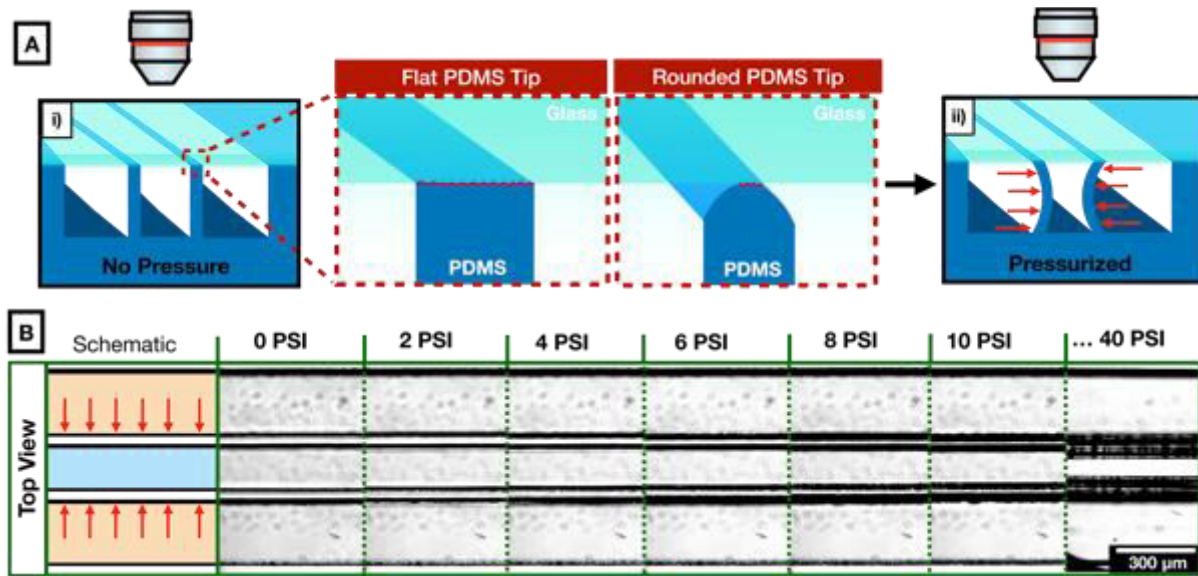
Figure 4. 4. Pneumatic actuation test of the high-aspect-ratio deformable PDMS sidewalls. **(a-i)** Schematic showing the bonding of the PDMS microchannels to the glass slide. (inset). If the tip of the PDMS sidewalls is not flat due to the insufficient filling of the copy mold material, the effective bonding region between the PDMS and the glass slide (shown by the red squiggly lines) decreases, which leads to declined bonding strength. **(a-ii)** Schematic showing the deflection caused by the application of pneumatic pressure to the system after sealing the PDMS geometry with a glass slide. **(b)** DIC microscope images show the gradual deflection of the deformable PDMS sidewalls in response to pneumatic actuation where the effective width of the central microchannel decreases as the walls deflect inwards without detaching from the glass slide.

Combination of different microscale features into a single monolithic mold

With the development of new microfabrication tools, microdevices become increasingly more complicated with combinations of multiple layers of PDMS building blocks[258-260]. This often requires the combination of PDMS layers with different feature geometries obtained from different master molds that have been fabricated using different microfabrication techniques. However, PDMS has different curing characteristics on different molds which can be problematic especially if the final system needs to be structurally active (i.e. mechanical properties of the PDMS features need to be utilized) or if residual uncrosslinked polymer chains remaining in the PDMS needs to be controlled[261,262]. In addition, some of the master mold

120

materials are not thermally stable. For example, heating-cooling cycles lead to delamination of the thick Pr layer in the Si-Pr composite master molds[263]. Some UV curable resins used in 3D printing have low HDT which requires curing of the PDMS at low temperatures for prolonged times, limiting the throughput of fabrication. Furthermore, master molds containing residual sulfur, unsaturated hydrocarbon plasticizers, or organotin catalyst can prevent PDMS from curing thoroughly[264] rendering them unusable even though otherwise they would be useful[202].

Since there is almost no practical limit for the footprint area for the PCH molding approach, we have simultaneously copied 19 unique PDMS microfeatures obtained from master molds fabricated by either photolithography, mechanical micromilling, or 3D printing into a single monolithic PC copy mold in order to prevent these problems associated with complex microfluidic devices **(Figure 4.5a)**. Using this combined PCH molding approach, all of these PDMS parts can be fabricated through a single monolithic PC mold consistently. Given the unique advantages of each master mold fabrication technique such as multi-step complex geometry fabrication with 3D printing **(Figure 4.5a-iii)**, fabrication of the features with continuously changing height distribution with mechanical micromilling **(Figs. 4.5a-ii and 4.5a-iv)**, and high-resolution high-aspect-ratio fabrication using photolithography **(Figs. 4.5a-i and 4.5a-v)**, it would be a tremendous challenge to fabricate these PDMS microfeatures from a single master mold with a single step. As a proof-of-concept fabrication, we have produced PDMS parts from this PC copy mold and fabricated a multilayer microfluidic device **(Figure 4.5b)** where each layer of the microfluidic device was originally fabricated through a different master mold fabrication technique. This shows individual layers that would be very hard to fabricate using a single master mold microfabrication technique. This type of PCH molding approach

could be very useful to produce kits with monolithically unified geometries that could be used

to directly fabricate building blocks for complex multilayered microfluidic systems.
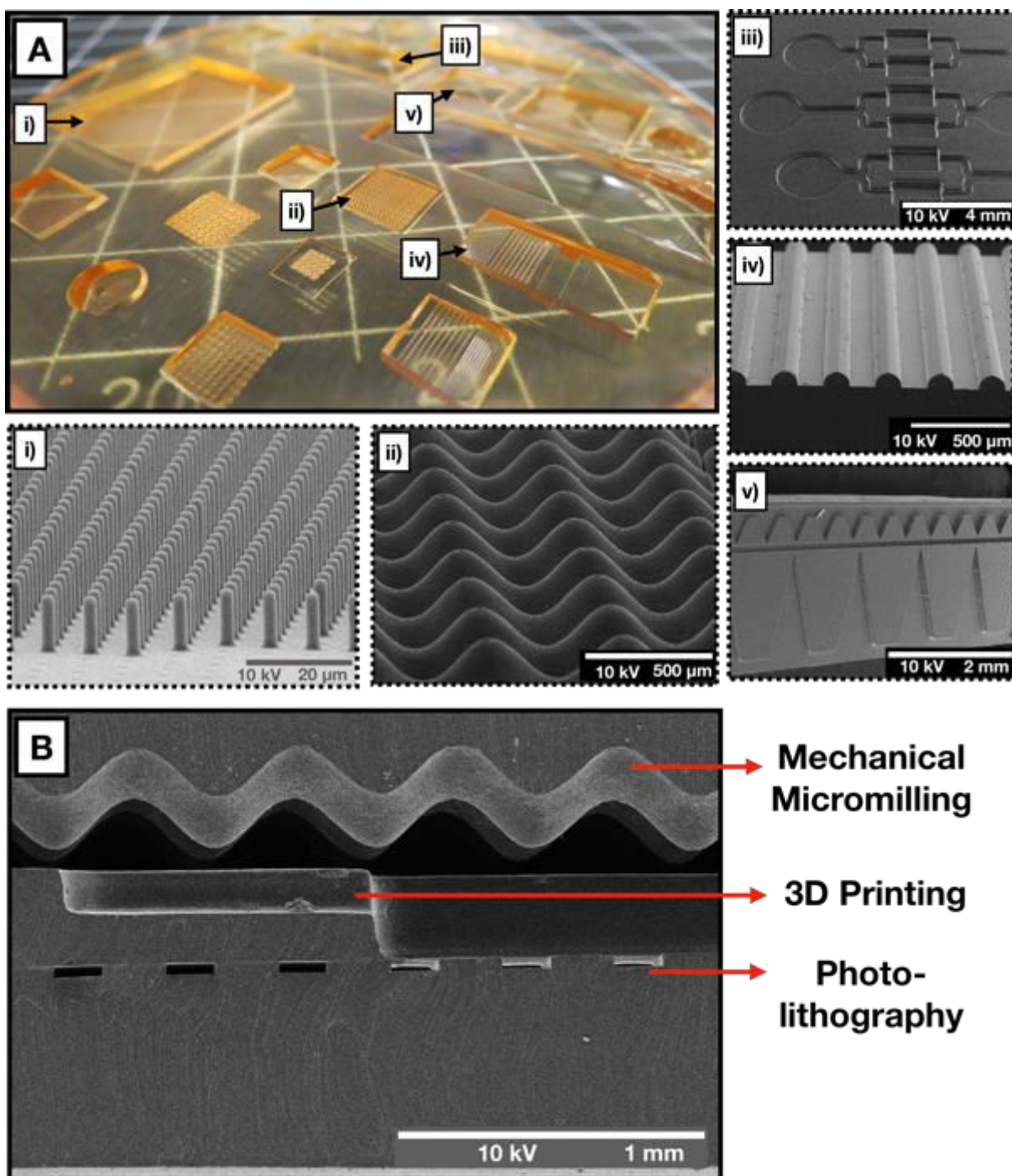
Figure 4. 5. Combination of different microfeatures in a monolithic rigid polycarbonate copy mold. **(a)** Photograph of a 4-inch diameter PC copy mold with 19 different microstructure geometries copied from different master molds, which were fabricated through various microfabrication techniques. Insets show the SEM images of a selection of the PDMS geometries fabricated from this mold (grids are in inches). **(i)**

122

High-aspect-ratio micropost array (master mold was originally fabricated through photolithography), **(ii)** undulated microtopology (master mold was originally fabricated through mechanical micromilling), **(iii)** multistep microfluidic flow circuit (master mold was originally fabricated through stereolithography 3D printing), **(iv)** semicircular micro-rib array (master mold was originally fabricated through mechanical micromilling), **(v)** triangular microfluidic concentrator array (master mold was originally fabricated through photolithography). **(b)** SEM image of the cross section of a proof-of-concept multilayered PDMS microfluidic device fabricated from a single monolithic PC copy mold. Molds needed to fabricate each of these three layers normally require a different fabrication technique. However, these molds were combined into a single monolithic PC copy mold to facilitate fast and reliable fabrication through a single PC copy mold.

Fabrication of submicron features

Geometries with submicron features were used in a variety of Lab-on-a-Chip systems to study biophysical aspects various phenomena such as cell alignment[265], migration[266], signaling[267], gene expression[268], and differentiation[269]. Although the soft lithography approach with PDMS replica molding has the potential to fabricate micro and nanosystems with feature sizes down to ~30 nm, the practical limit of the minimum feature size is tied to the feature resolution of the master molds[215]. The master mold fabrication techniques mentioned previously cannot be directly used to fabricate master molds with submicron features. However, a variety of other techniques have been modified to fabricate microtopologies with submicron feature resolution[270] which then can be adapted to function as master molds for soft lithography[271-274]. To test the limits of the feature size that can be replicated by the PCH molding technique, we used holographic diffraction gratings that have sinusoidal waves with ~1 µm wavelength and ~125 nm amplitude as master mold. We fabricated PC copy molds out of these master molds in the same way as described previously except that we did not coat any samples with TFOCS in order to not affect the submicron feature topology. We, then, quantitatively compared the PDMS samples obtained from the master mold with the ones fabricated through PC copy mold using AFM **(Figure 4.6)**. Similar to the other quantitative

comparisons done on the previous microgeometries, the wavelength of the gratings increased

by 5.9% with PC copy molds. On the other hand, the amplitude of the sinusoidal waves

decreased by 20.8% to 100.6 nm on average for the PDMS samples fabricated through PC copy

molds **(Figure 4.6b)**. Although the submicron topology of the master mold has been successfully

copied by PC heat molding technique **(Figure 4.6a)**, the quantitative comparisons results

demonstrate that in this specific example, the copying fidelity declines as the feature size

decreases. Furthermore, uniformity of the wave amplitude decreased in the PC copy molds,

which resulted in an increase in the standard deviation of the wave amplitude throughout the

sample. Copying smaller feature sizes with different topological characteristics may even be

possible with further optimization on the PCH molding technique; however, we currently do not

have such data.
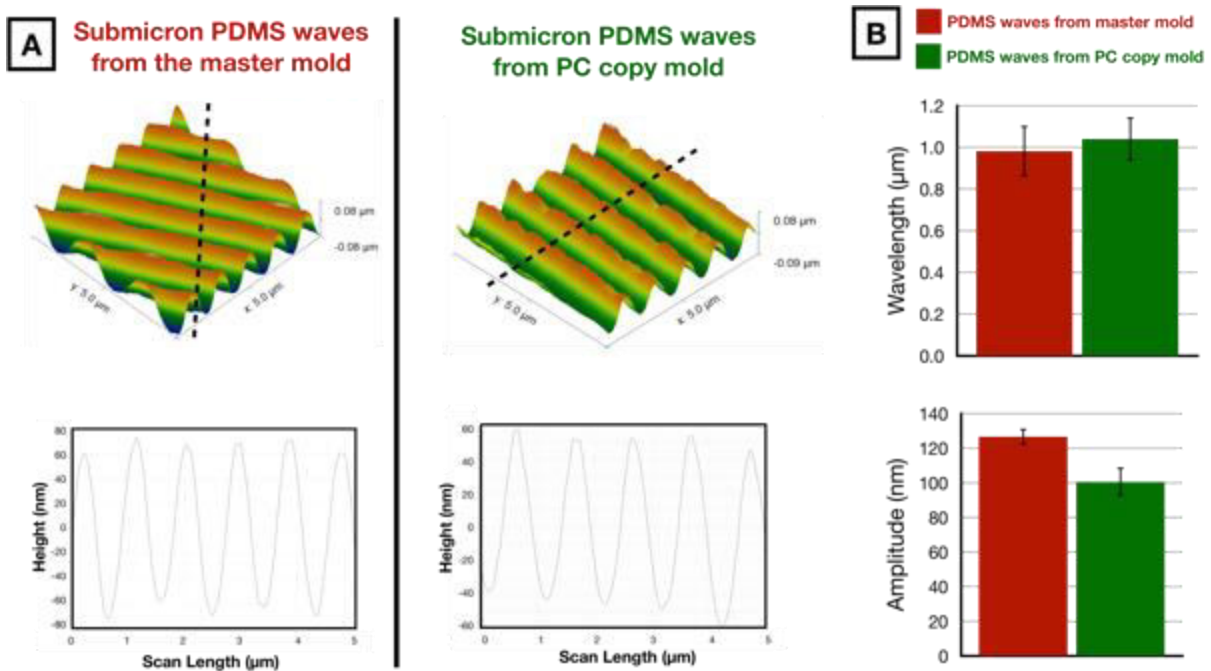
Figure 4. 6. Application of the polycarbonate heat molding technique to submicron features. **(a)** AFM surface topology comparison of the PDMS submicron wave topology fabricated through the master mold and PC copy molds. (bottom) A sample surface profile is plotted across the black dashed lines showing the wavy cross-section. **(b)** Quantitative comparison of the amplitude and the wavelength of the PDMS

wavy topology fabricated through the master mold and PC copy mold. The PDMS parts fabricated through the PC copy mold (green) have a 5.9% increase in the wavelength as would be expected based on previous quantitative comparisons. Also, the amplitude of the waves has a 20.8% decrease implying some limits of the technique for copying features with high fidelity.

Discussion

The PCH molding technique presented here allows for the duplication of master molds into PC sheets to be used in soft lithography without a need for any sophisticated equipment or expensive reagents. This approach can be employed to overcome fabrication problems and limited lifetime challenges associated with the master molds as well as to increase the throughput and feasibility of complex microsystem fabrication. There are several other studies in the literature that introduce different techniques to generate copy molds for various purposes[228,230-232]. Although, these techniques have been successfully used in different applications, none of these approaches show fabrication of copy molds for high-aspect-ratio protrusions at different scales. Since PDMS itself is an elastomeric material, such slender geometries are inherently prone to distortions during the master mold copying process. To our knowledge, fabrication of such copy molds has never been reported and the geometries that have been fabricated through copy molds have never been tested for their structural functionality which is crucial for many applications. Moreover, these techniques have not demonstrated the compatibility of their techniques with master molds fabricated through microfabrication techniques other than photolithography. By showing the compatibility of our technique with micro-milled and 3D-printed master molds we have demonstrated that our PC heat molding technique can be used to fabricate molds not just for 2D microchannels but also for undulating geometries with continuously-changing height and multi-step networks. We also uniquely employed the PC heat molding technique to fabricate copy molds for wavy patterns at the submicron scale. Although,

the overall submicron topology was copied into PC molds, we have observed lower copy fidelity at the submicron scale. We further showed for the first time that multiple unconventional master mold geometries fabricated by different techniques can be unified in a single monolithic mold by simultaneous copying, enabling more consistent and higher-throughput fabrication of multilayered complex microdevices. Lastly, the relatively higher HDT of PC compared to other materials used in different techniques enables its use for flash-curing protocols[275], which would not be possible with other techniques[230].

Overall, the PC heat molding technique introduces a simple approach to create molds complementary to the master molds with a number of advantages over conventional master molds. PC copy molds are monolithic. They do not pose delamination risk which can happen for Si-Pr master molds and is one of the major reasons for their limited lifetime especially when thick Pr coating and high-aspect-ratio features are needed. Since the brittleness of PC[276] is substantially lower than both cross-linked SU-8[277] and monocrystalline silicon[278], it is neither likely for PC copy molds to crack during microfabrication. Also, the same PDMS part can be used repeatably to fabricate more PC molds, increasing the throughput of the mold fabrication. Additionally, when PDMS replica molding is accomplished through PC copy molds, the height of the PDMS part is also preserved. This is very important for many applications where the PDMS thickness is critical for preserving the microchannel geometry[196], for having consistent gas permeation into PDMS microchannels[279,280] or to fabricate microfluidic valves[281]. PDMS parts fabricated through Si-Pr composite master molds generally do not have a consistent thickness since PDMS thickness is determined relatively arbitrarily depending on the exact amount of PDMS poured on Si-Pr molds from one fabrication to the next. Lastly, PDMS is not an ideal material for the commercialization of microfluidic devices due to its undesirable

126

material properties such as their hydrophobic recovery, aging, absorption of small hydrophobic compounds, and short shelf life[262]. New materials such as different thermoplastic elastomers (TPE) have recently gained attention as alternative materials to PDMS for more widely available commercial microfluidic devices[282]. However, studies concerning the investigation of better materials and optimization of the composition and fabrication protocols of TPEs has an inherent risk of damaging the important master molds during the experimental fabrication processes. PC copy molds can be very cheaply fabricated and duplicated which make them extremely well suited for experimental materials without any risk for damaging the master molds.

The PCH molding technique can also potentially be used to fabricate microfluidic devices out of thermoplastics (**Figure 4.1a**). Instead of obtaining PDMS microchannels with a final replica molding step, inlet and outlet holes can be drilled on the PC geometry and then can be heat bonded to another non-patterned sheet of thermoplastic. For this, the process temperature should be defined based on the T_g of the thermoplastic and the thermal degradation temperature of the materials used in the process. Here, the thermal degradation temperature of PC is not taken into account as it is higher than that of PDMS[283].

Together with the aforementioned advantages of the PC heat molding technique, there are also some limitations and drawbacks. The PC copy molds show up to ~6% increase in the feature sizes. Although, this is not desirable, users can account for this prior to fabrication without a need for characterizing each master mold geometry. A 6% dimensional increase in the features fabricated through the PC copy molds are similar to others reported in the literature and lower than the regular ~10% tolerances photolithographic fabrication processes[230]. At the submicron scale, the copying fidelity decreases and is above the ~10% tolerance but the PC heat molding technique still can be used as the submicron topology is conserved. PDMS is highly gas

permeable, which reduces the chance of air being trapped between the melted PC sheets and the PDMS molds. Nevertheless, we rarely observed air trapped between the melted PC sheet and the PDMS molds. This leads to formation of bubbles but they tend to expand and burst in sufficient time with an extended process duration. The consideration of having the PCH molding technique in a vacuum oven for better results may seem plausible due to reducing the chance of air being trapped between the PDMS mold and the melted PC sheet. However, our experiments in a vacuum oven indicated that, no matter how long the PC sheets are being dried prior to the experiments, the remaining absorbed humidity leads PC sheets to produce bubbles upon heating in a vacuum oven, creating defects all around the PC sheet similar to that shown in.

Conclusion

Our PCH molding technique is a desirable method to fabricate alternative master molds for soft lithographic applications. The technique does not necessarily require any hazardous or cytotoxic solvents, costly polymers, or any specialized equipment, which makes it useful to almost any laboratory that has a PC sheet and an oven, which are easy to obtain. This approach can be used to produce PC copy molds that contain high-aspect-ratio protrusions and indentations with vertical sidewalls and flat tips. Using this technique, we have readily molded microstructures at high fidelity with feature sizes as small as 1.0 µm and aspect ratios as large as 7. Furthermore, there is little limit for the footprint area of monolithic PC copy molds. We have demonstrated the fabrication of microfeatures with micron-scale high-aspect-ratio features over areas as large as tens of centimeters. In addition, different master mold geometries that can only be fabricated through various microfabrication techniques can be combined into a single monolithic PC copy mold in a single step process for the fabrication of multilayered complex microdevices. We have characterized the copying fidelity of the technique by comparing different microsystems fabricated through the PC molds to the ones fabricated through master

molds along with the pneumatic tests on devices fabricated using this approach. Finally, we have used the PC heat molding technique to fabricate geometries with submicron feature sizes. Such advantages of fast, reliable, and economical fabrication of copy molds without the need of sophisticated equipment or specialized facilities would allow researchers to more easily scale up their fabrication and share their master mold geometries with each other fostering interdisciplinary collaborations. Since this approach does not require engineering know-how and user expertise, this can be employed in standard science labs and thus can promote the dissemination of the microfabrication technologies from engineers to scientists.

Chapter 5: Conclusion to this Thesis and Future Perspectives

Unlike physics and chemistry which can be driven by theoretical work, biological studies mostly rely on experimental work due to the complex nature of biological systems. This, in turn, requires the development of new engineering tools for biological experiments that are capable of unveiling what remained in dark with conventional tools. Historically, there have been many instances where a single researcher, a polymath, significantly contributed both to the advancement of biological knowledge and to the development of new engineering tools simultaneously. Nevertheless, due to the cumulative nature of both biology and engineering, modern advancements in experimental biology are increasingly dependent on the collaboration of multiple researchers from different backgrounds. In this thesis, I presented three novel biomedical microsystems that I developed as a result of my collaborations with biologists for enabling new experimental paradigms that would not be possible to achieve using conventional laboratory equipment. I characterized these systems using analytical and computational tools followed by experimental verification. While doing so, I strived for devising ways to simplify the use of these systems so that the biologists can use them as a standard tool for their experiments without a need for help from an engineer. After the design and characterization steps, I used these microsystems with our collaborators for proof-of-concept level biological studies. In addition to these microsystems, at the end of my thesis, I also introduced a new technique for easier fabrication of such microsystems.

The first microsystem mentioned here was a flow-free microfluidic steady-state concentration gradient generator for observing the cellular locomotion-driven motility of

immune cells under gradients of chemokines on different substrates. This microsystem enabled us to live-track motile immune cells while they are moving under linear gradients of chemokines. Using this system, we showed that the surface fibronectin concentration, the slope of the chemokine gradient and the average concentration of chemokine, can alter the motility behavior of Jurkat cells in different ways which results in a framework that may enable immune cells to quickly accumulate in inflammation zones while effectively searching for target cells. We have also used an extension of this microsystem with murine CD8+ T cells in order to assess the role of mitochondrial function and hypoglycemic environments in the chemotactic and chemokinetic response of these cells. Our results indicated that while the mitochondrial functions promoting faster cellular migration it desensitizes cells to chemokine gradients. On the other hand, hypoglycemic environments result in the slow migration of cells with an increasing sensitivity to the gradients of chemokines. Although the development and characterization of such a system takes a lot of time and effort, the mature product can be used by biologists without engineering background. Therefore, this system can be used by other immunologists for assessing the motility characteristics of different subsets of immune cells at different activation levels. Furthermore, the microchambers of this microsystem allows for the introduction of tissue slices. In this way, this microsystem can also be utilized to observe movements of immune cells within a native tissue rather than on a 2D substrates.

The second microsystem discussed in this thesis was microfluidic chip that can mechanically stimulate hundreds of Drosophila melanogaster (fruit fly) embryos in the form of compression. The collective design of the different compartments of this chip resulted in a particularly easy-to-use characteristic as embryos can be loaded, aligned, immobilized, compressed, and recovered with minimal user intervention. Using this system, we showed that

131

the genetic expression of a transcription factor, *Twist*, can be controlled by compression in a dose- and duration-dependent manner. Furthermore, we demonstrated that the otherwise localized expression of *Twist* in ventral side, can spread throughout the embryo as a result of the compression of whole embryo. Our results also indicated that the developmental kinetics as well as the hatching rate of the embryos can be altered with compression where, most notably, mild levels of compression can increase the hatching rate rendering them to have higher viability. The actual potential of this chip, though, lays in -omics studies where very high numbers of samples would need to be processed simultaneously. Currently, we are using this chip together with downstream 2-dimentional differential gel electrophoresis (2D-DIGE) analysis to map the mechanically regulated proteins in Drosophila embryos. In the future, while this system can easily be adapted to other small model organisms, it can also be added to the pipeline of other -omics studies that require high sample yield.

The third microsystem introduced here was a multimodal shear stress gradient generator microfluidic device that can expose endothelial cell monolayers to different levels of physiological shear stress magnitudes and their linear gradients along the direction of the flow. This device allows for the controlled exposure of endothelial cells to the forces exerted by blood flow especially at the arteriovenous junctions while observing them under microscope. Using this system, we showed that the different levels of physiological uniform shear stress results in dose-dependent orientation and polarization of endothelial cells against the flow. On the other hand, the introduction of shear stress gradients along the flow alters this response depending on the direction of the gradient where positive shear stress gradient inhibits, and negative shear stress gradients promotes this orientation against the flow. An important application of this device would be the study the roles of shear stress and shear stress transducers on cell membrane

in the formation and progression of arteriovenous malformations (AVMs). For example, a rare genetic disease called, hereditary hemorrhagic telangiectasia (HHT), which is caused by either ALK-1 or Endoglin mutations, is known manifest itself with specific AVMs and it is thought that these AVMs are formed as a result of altered endothelial cell migration patterns due to the pathological mechanotransduction of blood shear stress. This disease can be studied in this system by comparing the orientation and migration of wild type and ALK-1 knockout endothelial cells in response to shear stress modalities that replicate the regions of AVMs.

I concluded this thesis by suggesting a new way of microfabrication technique called, Polycarbonate heat molding (PCH), that may enable the fabrication of the microsystems such as the ones described above in a more robust manner with higher-throughput by copying the original master molds that are used to build these microsystems. Here, I showcased application of this approach to the fabrication of various micron scale features ranging from high-aspect-ratio micropillars and elastomeric walls to undulated topologies and multistep geometries with more than 95%-dimensional fidelity. Furthermore, I tested the limits of this approach using submicron diffraction gratings. I should confess here that the development of this microfabrication technique was initiated by pure serendipity and the selection of polycarbonate as a copy material was only because it was the only feasible plastic available to me at the time. Although polycarbonate proved to be a good material of choice for this application, different plastics with heat deflection temperature lower than the thermal degradation temperature of PDMS should also be tested for their potential benefits. In this respect, in the future, this technique can be adapted to be used with different materials such as polystyrene, Poly (methyl methacrylate), and polyvinyl chloride.

References

1   Whitesides, G. M. The origins and the future of microfluidics. *Nature* **442**, 368, doi:10.1038/nature05058 (2006).

2   Ma, J., Wang, Y. & Liu, J. Biomaterials meet microfluidics: from synthesis technologies to biological applications. *Micromachines* **8**, 255 (2017).

3   Wilson, E. B. *The cell in development and inheritance*. Vol. 4 (Macmillan, 1900).

4   Kitano, H. Towards a theory of biological robustness. *Molecular systems biology* **3** (2007).

5   Bruggeman, F. J. & Westerhoff, H. V. The nature of systems biology. *TRENDS in Microbiology* **15**, 45-50 (2007).

6   Kim, A. A., Nekimken, A. L., Fechner, S., O'Brien, L. E. & Pruitt, B. L. in *Methods in cell biology* Vol. 146   217-259 (Elsevier, 2018).

7   Sonmez, U. M. *et al.* Chemotactic Responses of Jurkat Cells in Microfluidic Flow-Free Gradient Chambers. *Micromachines* **11**, 384 (2020).

8   Shorr, A. Z., Sönmez, U. M., Minden, J. S. & LeDuc, P. R. High-throughput mechanotransduction in Drosophila embryos with mesofluidics. *Lab on a Chip* **19**, 1141-1152, doi:10.1039/c8lc01055b (2019).

9   Sonmez, U. M., Cheng, Y.-W., Watkins, S. C., Roman, B. L. & Davidson, L. A. Endothelial cell polarization and orientation to flow in a novel microfluidic multimodal shear stress generator. *Lab on a Chip* **20**, 4373-4390 (2020).

10   Sonmez, U. M., Coyle, S., Taylor, R. E. & LeDuc, P. R. Polycarbonate Heat Molding for Soft Lithography. *Small* **16**, 2000241 (2020).

11   Scarpa, E. & Mayor, R. Collective cell migration in development. *J Cell Biol* **212**, 143-155, doi:10.1083/jcb.201508047 (2016).

12   Forbes, S. J. & Rosenthal, N. Preparing the ground for tissue regeneration: from mechanism to therapy. *Nature medicine* **20**, 857, doi:10.1038/nm.3653 (2014).

13   Ayala, R., Shu, T. & Tsai, L.-H. Trekking across the brain: the journey of neuronal migration. *Cell* **128**, 29-43, doi:10.1016/j.cell.2006.12.021 (2007).

14   Kunkel, E. J. & Butcher, E. C. Chemokines and the tissue-specific migration of lymphocytes. *Immunity* **16**, 1-4 (2002).

15   Godessart, N. & Kunkel, S. L. Chemokines in autoimmune disease. *Current opinion in immunology* **13**, 670-675 (2001).

16   White, G. E., Iqbal, A. J. & Greaves, D. R. CC chemokine receptors and chronic inflammation—therapeutic opportunities and pharmacological challenges. *Pharmacological reviews* **65**, 47-89 (2013).

17   Roussos, E. T., Condeelis, J. S. & Patsialou, A. Chemotaxis in cancer. *Nature Reviews Cancer* **11**, 573, doi:10.1038/nrc3078 (2011).

18   Muller, A. *et al.* Involvement of chemokine receptors in breast cancer metastasis. *Nature* **410**, 50-56, doi:10.1038/35065016 (2001).

19   Gerard, C. & Rollins, B. J. Chemokines and disease. *Nature immunology* **2**, 108, doi:10.1038/84209 (2001).

20   Korkmaz, E. *et al.* Therapeutic intradermal delivery of tumor necrosis factor-alpha antibodies using tip-loaded dissolvable microneedle arrays. *Acta biomaterialia* **24**, 96-105 (2015).

21   Restifo, N. P., Dudley, M. E. & Rosenberg, S. A. Adoptive immunotherapy for cancer: harnessing the T cell response. *Nature Reviews Immunology* **12**, 269, doi:10.1038/nri3191 (2012).

22   Boyden, S. The chemotactic effect of mixtures of antibody and antigen on polymorphonuclear leucocytes. *Journal of Experimental Medicine* **115**, 453-466 (1962).

23   Kim, Y. *et al.* Mechanochemical actuators of embryonic epithelial contractility. *Proceedings of the National Academy of Sciences of the United States of America* **111**, 14366-14371, doi:10.1073/pnas.1405209111 (2014).

24   Hazar, M. *et al.* 3D Bio-etching of a Complex Composite-like Embryonic Tissue. *Lab on a Chip* **15**, 3293-3299, doi:10.1039/c5lc00530b (2015).

25   Chung, H. H. *et al.* Highly permeable silicon membranes for shear free chemotaxis and rapid cell labeling. *Lab Chip* **14**, 2456-2468, doi:10.1039/c4lc00326h (2014).

26   Chiu, D. T. *et al.* Small but perfectly formed? Successes, challenges, and opportunities for microfluidics in the chemical and biological sciences. *Chem* **2**, 201-223 (2017).

27   Dertinger, S. K., Chiu, D. T., Jeon, N. L. & Whitesides, G. M. Generation of gradients having complex shapes using microfluidic networks. *Analytical Chemistry* **73**, 1240-1246 (2001).

28   Jeon, N. L. *et al.* Generation of solution and surface gradients using microfluidic systems. *Langmuir* **16**, 8311-8316, doi:DOI 10.1021/la000600b (2000).

29   Beta, C., Fröhlich, T., Bödeker, H. U. & Bodenschatz, E. Chemotaxis in microfluidic devices—a study of flow effects. *Lab on a Chip* **8**, 1087-1096 (2008).

30   Warren, K., Mpagazehe, J., LeDuc, P. & Higgs III, C. Geometric effects in microfluidics on heterogeneous cell stress using an Eulerian–Lagrangian approach. *Lab on a Chip* **16**, 593-598 (2016).

31   Walker, G. M. *et al.* Effects of flow and diffusion on chemotaxis studies in a microfabricated gradient generator. *Lab on a Chip* **5**, 611-618, doi:10.1039/b417245k (2005).

32   Walker, G. M., Zeringue, H. C. & Beebe, D. J. Microenvironment design considerations for cellular scale studies. *Lab on a Chip* **4**, 91-97, doi:10.1039/b311214d (2004).

33   Melchionna, R. *et al.* Laminar shear stress inhibits CXCR4 expression on endothelial cells: functional consequences for atherogenesis. *The FASEB journal* **19**, 629-631, doi:10.1096/fj.04-2219fje (2005).

34   Cheng, S.-Y. *et al.* A hydrogel-based microfluidic device for the studies of directed cell migration. *Lab on a Chip* **7**, 763-769, doi:10.1039/b618463d (2007).

35   Abhyankar, V. V. *et al.* A platform for assessing chemotactic migration within a spatiotemporally defined 3D microenvironment. *Lab on a Chip* **8**, 1507-1515, doi:10.1039/b803533d (2008).

36   Wu, H., Huang, B. & Zare, R. N. Generation of complex, static solution gradients in microfluidic channels. *Journal of the American Chemical Society* **128**, 4194-4195, doi:10.1021/ja058530o (2006).

37   Mosadegh, B. *et al.* Generation of stable complex gradients across two-dimensional surfaces and three-dimensional gels. *Langmuir* **23**, 10910-10912, doi:10.1021/la7026835 (2007).

38   Haring, A. P. *et al.* 3D Printed Multiplexed Competitive Migration Assays with Spatially Programmable Release Sources. *Advanced Biosystems*, doi:10.1002/adbi.201900225 (2019).

39   Petrie Aronin, C. E. *et al.* Migrating Myeloid Cells Sense Temporal Dynamics of Chemoattractant Concentrations. *Immunity* **47**, 862-874 e863, doi:10.1016/j.immuni.2017.10.020 (2017).

40   Toh, A. G., Wang, Z., Yang, C. & Nguyen, N.-T. Engineering microfluidic concentration gradient generators for biological applications. *Microfluidics and nanofluidics* **16**, 1-18 (2014).

41   Saadi, W. *et al.* Generation of stable concentration gradients in 2D and 3D environments using a microfluidic ladder chamber. *Biomed Microdevices* **9**, 627-635, doi:10.1007/s10544-007-9051-9 (2007).

42   Irimia, D., Charras, G., Agrawal, N., Mitchison, T. & Toner, M. Polar stimulation and constrained cell migration in microfluidic channels. *Lab on a Chip* **7**, 1783-1790, doi:10.1039/b710524j (2007).

43   Keenan, T. M., Frevert, C. W., Wu, A., Wong, V. & Folch, A. A new method for studying gradient-induced neutrophil desensitization based on an open microfluidic chamber. *Lab on a Chip* **10**, 116-122, doi:10.1039/b913494h (2010).

44   Mishra, S., Pena, J. S., Redenti, S. & Vazquez, M. A novel electro-chemotactic approach to impact the directional migration of transplantable retinal progenitor cells. *Exp Eye Res* **185**, 107688, doi:10.1016/j.exer.2019.06.002 (2019).

45   Biswenger, V. *et al.* Characterization of EGF-guided MDA-MB-231 cell chemotaxis in vitro using a physiological and highly sensitive assay system. *PLoS One* **13**, e0203040, doi:10.1371/journal.pone.0203040 (2018).

46   Frank, T. & Tay, S. Flow-switching allows independently programmable, extremely stable, high-throughput diffusion-based gradients. *Lab Chip* **13**, 1273-1281, doi:10.1039/c3lc41076e (2013).

47   Schwarz, J. *et al.* A microfluidic device for measuring cell migration towards substrate-bound and soluble chemokine gradients. *Sci Rep* **6**, 36440, doi:10.1038/srep36440 (2016).

48   Wu, J., Wu, X. & Lin, F. Recent developments in microfluidics-based chemotaxis studies. *Lab on a Chip* **13**, 2484-2499, doi:10.1039/c3lc50415h (2013).

49   Kothapalli, C. R. *et al.* A high-throughput microfluidic assay to study neurite response to growth factor gradients. *Lab on a Chip* **11**, 497-507, doi:10.1039/c0lc00240b (2011).

50   Atencia, J., Morrow, J. & Locascio, L. E. The microfluidic palette: a diffusive gradient generator with spatio-temporal control. *Lab on a Chip* **9**, 2707-2714, doi:10.1039/b902113b (2009).

51   Uzel, S. G. *et al.* Simultaneous or Sequential Orthogonal Gradient Formation in a 3D Cell Culture Microfluidic Platform. *Small* **12**, 612-622, doi:10.1002/smll.201501905 (2016).

52   Atencia, J., Cooksey, G. A. & Locascio, L. E. A robust diffusion-based gradient generator for dynamic cell assays. *Lab on a Chip* **12**, 309-316, doi:10.1039/c1lc20829b (2012).

53   Muinonen-Martin, A. J., Veltman, D. M., Kalna, G. & Insall, R. H. An improved chamber for direct visualisation of chemotaxis. *PloS one* **5**, e15309, doi:10.1371/journal.pone.0015309 (2010).

54   Xia, Y. & Whitesides, G. M. Soft lithography. *Angewandte Chemie International Edition* **37**, 550-575, doi:10.1002/(SICI)1521-3773(19980316)37:5<550::AID-ANIE550>3.0.CO;2-G (1998).

55   Yazdi, A. A. *et al.* 3D printing: an emerging tool for novel microfluidics and lab-on-a-chip applications. *Microfluidics and Nanofluidics* **20**, 50, doi:ARTN 50

10.1007/s10404-016-1715-4 (2016).

56   Ho, C. M. B., Ng, S. H., Li, K. H. H. & Yoon, Y.-J. 3D printed microfluidics for biological applications. *Lab on a Chip* **15**, 3627-3637, doi:10.1039/c5lc00685f (2015).

57   Ghosh, S., Preet, A., Groopman, J. E. & Ganju, R. K. Cannabinoid receptor CB2 modulates the CXCL12/CXCR4-mediated chemotaxis of T lymphocytes. *Molecular immunology* **43**, 2169-2179 (2006).

58   Zaman, S. N., Resek, M. E. & Robbins, S. M. Dual acylation and lipid raft association of Src - family protein tyrosine kinases are required for SDF - 1/CXCL12 - mediated chemotaxis in the Jurkat human T cell lymphoma cell line. *Journal of leukocyte biology* **84**, 1082-1091 (2008).

59   Zhou, Y. & Lin, Q. Microfluidic flow-free generation of chemical concentration gradients. *Sensor Actuat B-Chem* **190**, 334-341, doi:10.1016/j.snb.2013.08.073 (2014).

60   Halldorsson, S., Lucumi, E., Gómez-Sjöberg, R. & Fleming, R. M. T. Advantages and challenges of microfluidic cell culture in polydimethylsiloxane devices. *Biosensors and Bioelectronics* **63**, 218-231 (2015).

61   Jóźwik, A., Soroczyńska, M., Witkowski, J. M. & Bryl, E. CD3 receptor modulation in Jurkat leukemic cell line. *Folia Histochem Cyto* **42**, 41-43 (2004).

62   Jaqaman, K. *et al.* Robust single-particle tracking in live-cell time-lapse sequences. *Nature methods* **5**, 695, doi:10.1038/nmeth.1237 (2008).

63   Tinevez, J.-Y. *et al.* TrackMate: An open and extensible platform for single-particle tracking. *Methods* **115**, 80-90, doi:10.1016/j.ymeth.2016.09.016 (2017).

64   Maheshwari, G. & Lauffenburger, D. A. Deconstructing (and reconstructing) cell migration. *Microscopy research and technique* **43**, 358-368, doi:10.1002/(SICI)1097-0029(19981201)43:5<358::AID-JEMT2>3.0.CO;2-D (1998).

65   Tanford, C. *Physical chemistry of macromolecules*. (Wiley, 1961).

66   Aran, K., Sasso, L. A., Kamdar, N. & Zahn, J. D. Irreversible, direct bonding of nanoporous polymer membranes to PDMS or glass microdevices. *Lab on a Chip* **10**, 548-552, doi:10.1039/b924816a (2010).

67   Chueh, B.-h. *et al.* Leakage-free bonding of porous membranes into layered microfluidic array systems. *Analytical chemistry* **79**, 3504-3508, doi:10.1021/ac062118p (2007).

68   Wu, H., Huang, B. & Zare, R. N. Construction of microfluidic chips using polydimethylsiloxane for adhesive bonding. *Lab on a Chip* **5**, 1393-1398, doi:10.1039/b510494g (2005).

69   Weninger, W. & von Andrian, U. H. in *Seminars in immunology.* 257-270 (Elsevier).

70   Debes, G. F. *et al.* Chemokine receptor CCR7 required for T lymphocyte exit from peripheral tissues. *Nature immunology* **6**, 889, doi:10.1038/ni1238 (2005).

71   Wu, X. *et al.* Analysis of CCR7 mediated T cell transfectant migration using a microfluidic gradient generator. *Journal of immunological methods* **419**, 9-17 (2015).

72   Nagy, K. *et al.* Microfluidic study of the chemotactic response of Escherichia coli to amino acids, signaling molecules and secondary metabolites. *Biomicrofluidics* **9**, 044105, doi:10.1063/1.4926981 (2015).

73   Butler, J. T., Samantaray, S., Beeson, C. C., Ray, S. K. & Banik, N. L. Involvement of calpain in the process of Jurkat T cell chemotaxis. *Journal of neuroscience research* **87**, 626-635 (2009).

74   Berthier, E., Surfus, J., Verbsky, J., Huttenlocher, A. & Beebe, D. An arrayed high-content chemotaxis assay for patient diagnosis. *Integrative Biology* **2**, 630-638, doi:10.1039/c0ib00030b (2010).

75   Nandagopal, S., Wu, D. & Lin, F. Combinatorial guidance by CCR7 ligands for T lymphocytes migration in co-existing chemokine fields. *PloS one* **6**, e18183, doi:10.1371/journal.pone.0018183 (2011).

76   Mehling, M., Frank, T., Albayrak, C. & Tay, S. Real-time tracking, retrieval and gene expression analysis of migrating human T cells. *Lab on a Chip* **15**, 1276-1283, doi:10.1039/c4lc01038h (2015).

77   Håkansson, L. & Venge, P. The combined action of hyaluronic acid and fibronectin stimulates neutrophil migration. *The Journal of Immunology* **135**, 2735-2739 (1985).

78   Lacalle, R. A. *et al.* PTEN regulates motility but not directionality during leukocyte chemotaxis. *Journal of cell science* **117**, 6207-6215 (2004).

79   Griffith, J. W., Sokol, C. L. & Luster, A. D. Chemokines and chemokine receptors: positioning cells for host defense and immunity. *Annual review of immunology* **32**, 659-702, doi:10.1146/annurev-immunol-032713-120145 (2014).

80   Crank, J. *The mathematics of diffusion*. (Oxford university press, 1979).

81   Skoge, M. *et al.* Gradient sensing in defined chemotactic fields. *Integrative Biology* **2**, 659-668, doi:10.1039/c0ib00033g (2010).

82   Kolaczkowska, E. & Kubes, P. Neutrophil recruitment and function in health and inflammation. *Nature Reviews Immunology* **13**, 159, doi:10.1038/nri3399 (2013).

83   Parent, C. A., Blacklock, B. J., Froehlich, W. M., Murphy, D. B. & Devreotes, P. N. G protein signaling events are activated at the leading edge of chemotactic cells. *Cell* **95**, 81-91 (1998).

84   Andrew, N. & Insall, R. H. Chemotaxis in shallow gradients is mediated independently of PtdIns 3-kinase by biased choices between random protrusions. *Nat Cell Biol* **9**, 193-U191, doi:10.1038/ncb1536 (2007).

85   Summers, C. *et al.* Neutrophil kinetics in health and disease. *Trends in immunology* **31**, 318-324, doi:10.1016/j.it.2010.05.006 (2010).

86   Owen, J. A., Punt, J. & Stranford, S. A. *Kuby immunology*. (WH Freeman New York, 2013).

87   Fernandez-Sanchez, M.-E., Brunet, T., Röper, J.-C. & Farge, E. Mechanotransduction's impact on animal development, evolution, and tumorigenesis. *Annual review of cell and developmental biology* **31**, 373-397 (2015).

88   Brouzés, E., Supatto, W. & Farge, E. Is mechano - sensitive expression of twist involved in mesoderm formation? *Biology of the Cell* **96**, 471-477 (2004).

89   Brouzés, E. & Farge, E. Interplay of mechanical deformation and patterned gene expression in developing embryos. *Current opinion in genetics & development* **14**, 367-374 (2004).

90   Ip, Y. T. & Gridley, T. Cell movements during gastrulation: snail dependent and independent pathways. *Current opinion in genetics & development* **12**, 423-429 (2002).

91   Costa, M., Wilson, E. T. & Wieschaus, E. A putative cell signal encoded by the folded gastrulation gene coordinates cell shape changes during Drosophila gastrulation. *Cell* **76**, 1075-1089 (1994).

92   St Johnston, D. & Nüsslein-Volhard, C. The origin of pattern and polarity in the Drosophila embryo. *Cell* **68**, 201-219 (1992).

93   Wozniak, M. A. & Chen, C. S. Mechanotransduction in development: a growing role for contractility. *Nature reviews Molecular cell biology* **10**, 34-43 (2009).

94   Farge, E. Mechanical induction of Twist in the Drosophila foregut/stomodeal primordium. *Current biology* **13**, 1365-1377 (2003).

95   Supatto, W. *et al.* In vivo modulation of morphogenetic movements in Drosophila embryos with femtosecond laser pulses. *Proceedings of the National Academy of Sciences* **102**, 1047-1052 (2005).

96   Desprat, N., Supatto, W., Pouille, P.-A., Beaurepaire, E. & Farge, E. Tissue deformation modulates twist expression to determine anterior midgut differentiation in Drosophila embryos. *Developmental cell* **15**, 470-477 (2008).

97   Desprat, N. *et al.* Embryos Drosophila Invagination in Mechanical Signals Trigger Myosin II Redistribution and Mesoderm. *Science Signaling* **2**, ra16-ra16 (2009).

98   Filas, B. A., Xu, G. & Taber, L. A. in *Tissue Morphogenesis*   3-16 (Springer, 2015).

99   Chen, C. *et al.* Design and operation of a microfluidic sorter for Drosophila embryos. *Sensors and Actuators B: Chemical* **102**, 59-66 (2004).

100   Chung, K. *et al.* A microfluidic array for large-scale ordering and orientation of embryos. *Nature methods* **8**, 171-176 (2011).

101   Levario, T. J., Zhan, M., Lim, B., Shvartsman, S. Y. & Lu, H. Microfluidic trap array for massively parallel imaging of Drosophila embryos. *Nature protocols* **8**, 721-736 (2013).

102   Bernstein, R. W. *et al.* Characterization of fluidic microassembly for immobilization and positioning of Drosophila embryos in 2-D arrays. *Sensors and Actuators A: Physical* **114**, 191-196 (2004).

103   Zhang, X. *et al.* Microoptical characterization and modeling of positioning forces on Drosophila embryos self-assembled in two-dimensional arrays. *Journal of Microelectromechanical Systems* **14**, 1187-1197 (2005).

104   Cui, X. *et al.* Lensless high-resolution on-chip optofluidic microscopes for Caenorhabditis elegans and cell imaging. *Proceedings of the National Academy of Sciences* **105**, 10670-10675 (2008).

105   Dagani, G. T. *et al.* Microfluidic self-assembly of live Drosophila embryos for versatile high-throughput analysis of embryonic morphogenesis. *Biomedical microdevices* **9**, 681-694 (2007).

106   Kim, Y. *et al.* Mechanochemical actuators of embryonic epithelial contractility. *Proceedings of the National Academy of Sciences* **111**, 14366-14371 (2014).

107   Gershow, M. *et al.* Controlling airborne cues to study small animal navigation. *Nature methods* **9**, 290-296 (2012).

108   Ohyama, T. *et al.* High-throughput analysis of stimulus-evoked behaviors in Drosophila larva reveals multiple modality-specific escape strategies. *PloS one* **8**, e71706 (2013).

109   Ghaemi, R., Rezai, P., Iyengar, B. G. & Selvaganapathy, P. R. Microfluidic devices for imaging neurological response of Drosophila melanogaster larva to auditory stimulus. *Lab on a Chip* **15**, 1116-1122 (2015).

110   Zhang, W., Yan, Z., Jan, L. Y. & Jan, Y. N. Sound response mediated by the TRP channels NOMPC, NANCHUNG, and INACTIVE in chordotonal organs of Drosophila larvae. *Proceedings of the National Academy of Sciences* **110**, 13612-13617 (2013).

111   Lockery, S. R. *et al.* Artificial dirt: microfluidic substrates for nematode neurobiology and behavior. *Journal of neurophysiology* **99**, 3136-3143 (2008).

112   Park, S. *et al.* Enhanced Caenorhabditis elegans locomotion in a structured microfluidic environment. *PloS one* **3**, e2550 (2008).

113   Zappe, S., Fish, M., Scott, M. P. & Solgaard, O. Automated MEMS-based Drosophila embryo injection system for high-throughput RNAi screens. *Lab on a Chip* **6**, 1012-1019 (2006).

114   Delubac, D. *et al.* Microfluidic system with integrated microinjector for automated Drosophila embryo injection. *Lab on a Chip* **12**, 4911-4919 (2012).

115   Sivagnanam, V. & Gijs, M. A. Exploring living multicellular organisms, organs, and tissues using microfluidic systems. *Chemical reviews* **113**, 3214-3247 (2013).

116   Kurth, F., Eyer, K., Franco-Obregón, A. & Dittrich, P. S. A new mechanobiological era: microfluidic pathways to apply and sense forces at the cellular level. *Current opinion in chemical biology* **16**, 400-408 (2012).

117   Kubicek, J. D., Brelsford, S., Ahluwalia, P. & LeDuc, P. R. Integrated lithographic membranes and surface adhesion chemistry for three-dimensional cellular stimulation. *Langmuir* **20**, 11552-11556 (2004).

118   Steward, R. L., Cheng, C.-M., Wang, D. L. & LeDuc, P. R. Probing cell structure responses through a shear and stretching mechanical stimulation technique. *Cell biochemistry and biophysics* **56**, 115-124 (2010).

119   Fakhoury, J. R., Sisson, J. C. & Zhang, X. Microsystems for controlled genetic perturbation of live Drosophila embryos: RNA interference, development robustness and drug screening. *Microfluidics and nanofluidics* **6**, 299-313 (2009).

120   Chiu, D. T. *et al.* Small but perfectly formed? Successes, challenges, and opportunities for microfluidics in the chemical and biological sciences. *Chem* **2**, 201-223 (2017).

121   Narciso, C. E., Contento, N. M., Storey, T. J., Hoelzle, D. J. & Zartman, J. J. Release of applied mechanical loading stimulates intercellular calcium waves in Drosophila wing discs. *Biophysical journal* **113**, 491-501 (2017).

122   Folch, A. *Introduction to bioMEMS*. (CRC Press, 2016).

123   Xia, Y. & Whitesides, G. M. Soft lithography. *Annual review of materials science* **28**, 153-184 (1998).

124   Lee, H. *et al.* A new fabrication process for uniform SU-8 thick photoresist structures by simultaneously removing edge bead and air bubbles. *Journal of Micromechanics and Microengineering* **21**, 125006 (2011).

125   Qin, D., Xia, Y. & Whitesides, G. M. Soft lithography for micro-and nanoscale patterning. *Nature protocols* **5**, 491 (2010).

126   Campos-Ortega, J. A. & Hartenstein, V. *The embryonic development of Drosophila melanogaster*. (Springer Science & Business Media, 2013).

127   Carrer, J., Mansur, W., Scuciato, R. & Fleischfresser, S. in *10th World Congress on Computational Mechanics.* (Citeseer).

128   Cowper, G. The shear coefficient in Timoshenko's beam theory. (1966).

129   Young, W. C., Budynas, R. G. & Sadegh, A. M. *Roark's formulas for stress and strain*. (McGraw-Hill Education, 2012).

130   Baratta, F. I. When is a beam a plate? *Journal of the American Ceramic Society* **64**, C - 86-C - 86 (1981).

131   Cook, R. D. & Young, W. C. *Advanced mechanics of materials*. Vol. 2 (Prentice Hall Upper Saddle River, NJ, 1999).

132   Pritchard, R. H., Lava, P., Debruyne, D. & Terentjev, E. M. Precise determination of the Poisson ratio in soft materials with 2D digital image correlation. *Soft Matter* **9**, 6037-6045 (2013).

133   Schindelin, J. *et al.* Fiji: an open-source platform for biological-image analysis. *Nature methods* **9**, 676-682 (2012).

134   Berthier, E., Young, E. W. & Beebe, D. Engineers are from PDMS-land, Biologists are from Polystyrenia. *Lab on a Chip* **12**, 1224-1237 (2012).

135   Chuang, Y.-J., Tseng, F.-G. & Lin, W.-K. Reduction of diffraction effect of UV exposure on SU-8 negative thick photoresist by air gap elimination. *Microsystem Technologies* **8**, 308-313 (2002).

136   Ling, Z. G., Lian, K. & Jian, L. in *Advances in Resist Technology and Processing XVII.* 1019-1027 (International Society for Optics and Photonics).

137   Lorenz, H., Despont, M., Vettiger, P. & Renaud, P. Fabrication of photoplastic high-aspect ratio microparts and micromolds using SU-8 UV resist. *Microsystem Technologies* **4**, 143-146 (1998).

138   Lin, C.-H., Lee, G.-B., Chang, B.-W. & Chang, G.-L. A new fabrication process for ultra-thick microfluidic microstructures utilizing SU-8 photoresist. *Journal of Micromechanics and Microengineering* **12**, 590 (2002).

139   Johnston, I., McCluskey, D., Tan, C. & Tracey, M. Mechanical characterization of bulk Sylgard 184 for microfluidics and microengineering. *Journal of Micromechanics and Microengineering* **24**, 035017 (2014).

140   Wang, Z., Volinsky, A. A. & Gallant, N. D. Crosslinking effect on polydimethylsiloxane elastic modulus measured by custom - built compression instrument. *Journal of Applied Polymer Science* **131** (2014).

141   Liu, M., Sun, J., Sun, Y., Bock, C. & Chen, Q. Thickness-dependent mechanical properties of polydimethylsiloxane membranes. *Journal of micromechanics and microengineering* **19**, 035028 (2009).

142   Placet, V. & Delobelle, P. Mechanical properties of bulk polydimethylsiloxane for microfluidics over a large range of frequencies and aging times. *Journal of Micromechanics and Microengineering* **25**, 035009 (2015).

143   Shen, Y., Xi, N. & Zhang, R. in *2008 IEEE International Conference on Robotics and Biomimetics.* 31-36 (IEEE).

144   Yanez, L. Z. & Camarillo, D. B. Microfluidic analysis of oocyte and embryo biomechanical properties to improve outcomes in assisted reproductive technologies. *MHR: Basic science of reproductive medicine* **23**, 235-247 (2017).

145   Fung, Y.-c. *Biomechanics: mechanical properties of living tissues*. (Springer Science & Business Media, 2013).

146   Forgacs, G., Foty, R. A., Shafrir, Y. & Steinberg, M. S. Viscoelastic properties of living embryonic tissues: a quantitative study. *Biophysical journal* **74**, 2227-2234 (1998).

147   Campas, O. in *Seminars in cell & developmental biology.* 119-130 (Elsevier).

148   Malik, W., Prasad, S., Rajagopal, K. & Preziosi, L. On the modeling of the viscoelastic response of embryonic tissues. *Mathematics and mechanics of solids* **13**, 81-91 (2008).

149   Foe, V. E. & Alberts, B. M. Reversible chromosome condensation induced in Drosophila embryos by anoxia: visualization of interphase nuclear organization. *The Journal of cell biology* **100**, 1623-1636 (1985).

150   Yang, M.-H. & Wu, K.-J. TWIST activation by hypoxia inducible factor-1 (HIF-1): implications in metastasis and development. *Cell cycle* **7**, 2090-2096 (2008).

151   Yang, M.-H. *et al.* Direct regulation of TWIST by HIF-1α promotes metastasis. *Nature cell biology* **10**, 295-305 (2008).

152   Coralli, C., Cemazar, M., Kanthou, C., Tozer, G. M. & Dachs, G. U. Limitations of the reporter green fluorescent protein under simulated tumor conditions. *Cancer research* **61**, 4784-4790 (2001).

153   Roman, B. L. & Pekkan, K. Mechanotransduction in embryonic vascular development. *Biomech Model Mechanobiol* **11**, 1149-1168, doi:10.1007/s10237-012-0412-9 (2012).

154   Tkachenko, E. *et al.* The nucleus of endothelial cell as a sensor of blood flow direction. *Biology open* **2**, 1007-1012 (2013).

155   Coan, D. E., Wechezak, A. R., Viggers, R. F. & Sauvage, L. R. Effect of shear stress upon localization of the Golgi apparatus and microtubule organizing center in isolated cultured endothelial cells. *J Cell Sci* **104 (Pt 4)**, 1145-1153 (1993).

156   Hikita, T. *et al.* PAR-3 controls endothelial planar polarity and vascular inflammation under laminar flow. *EMBO Rep* **19**, doi:10.15252/embr.201745253 (2018).

157   Ridley, A. J. *et al.* Cell migration: integrating signals from front to back. *Science* **302**, 1704-1709, doi:10.1126/science.1092053 (2003).

158   Kwon, H. B. *et al.* In vivo modulation of endothelial polarization by Apelin receptor signalling. *Nat Commun* **7**, 11805, doi:10.1038/ncomms11805 (2016).

159   Weijts, B. *et al.* Blood flow-induced Notch activation and endothelial migration enable vascular remodeling in zebrafish embryos. *Nature communications* **9**, 5314, doi:10.1038/s41467-018-07732-7 (2018).

160   Masuda, M. & Fujiwara, K. The biased lamellipodium development and microtubule organizing center position in vascular endothelial cells migrating under the influence of fluid flow. *Biol Cell* **77**, 237-245, doi:10.1016/s0248-4900(05)80193-5 (1993).

161   Morgan, J. T. *et al.* Nesprin-3 regulates endothelial cell morphology, perinuclear cytoskeletal architecture, and flow-induced polarization. *Molecular biology of the cell* **22**, 4324-4334, doi:10.1091/mbc.E11-04-0287 (2011).

162   LaMack, J. A. & Friedman, M. H. Individual and combined effects of shear stress magnitude and spatial gradient on endothelial cell gene expression. *Am J Physiol Heart Circ Physiol* **293**, H2853-2859, doi:10.1152/ajpheart.00244.2007 (2007).

163   Yoshino, D., Sakamoto, N. & Sato, M. Fluid shear stress combined with shear stress spatial gradients regulates vascular endothelial morphology. *Integrative biology : quantitative biosciences from nano to macro* **9**, 584-594, doi:10.1039/c7ib00065k (2017).

164   Levitt, M. R. *et al.* Genetic correlates of wall shear stress in a patient-specific 3D-printed cerebral aneurysm model. *J Neurointerv Surg* **11**, 999-1003, doi:10.1136/neurintsurg-2018-014669 (2019).

165   DePaola, N., Gimbrone Jr, M. A., Davies, P. F. & Dewey Jr, C. F. Vascular endothelium responds to fluid shear stress gradients. *Arteriosclerosis and thrombosis: a journal of vascular biology* **12**, 1254-1257 (1992).

166   Udan, R. S., Vadakkan, T. J. & Dickinson, M. E. Dynamic responses of endothelial cells to changes in blood flow during vascular remodeling of the mouse yolk sac. *Development* **140**, 4041-4050, doi:10.1242/dev.096255 (2013).

167   Franco, C. A. *et al.* Dynamic endothelial cell rearrangements drive developmental vessel regression. *PLoS Biol* **13**, e1002125, doi:10.1371/journal.pbio.1002125 (2015).

168   Shojima, M. *et al.* Magnitude and role of wall shear stress on cerebral aneurysm: computational fluid dynamic study of 20 middle cerebral artery aneurysms. *Stroke* **35**, 2500-2505, doi:10.1161/01.STR.0000144648.89172.0f (2004).

169   Dolan, J. M., Kolega, J. & Meng, H. High wall shear stress and spatial gradients in vascular pathology: a review. *Ann Biomed Eng* **41**, 1411-1427, doi:10.1007/s10439-012-0695-0 (2013).

170   Kulcsar, Z. *et al.* Hemodynamics of cerebral aneurysm initiation: the role of wall shear stress and spatial wall shear stress gradient. *AJNR Am J Neuroradiol* **32**, 587-594, doi:10.3174/ajnr.A2339 (2011).

171   Huo, Y., Wischgoll, T. & Kassab, G. S. Flow patterns in three-dimensional porcine epicardial coronary arterial tree. *Am J Physiol Heart Circ Physiol* **293**, H2959-2970, doi:00586.2007 [pii]

10.1152/ajpheart.00586.2007 (2007).

172   Bernabeu, M. O. *et al.* Computer simulations reveal complex distribution of haemodynamic forces in a mouse retina model of angiogenesis. *J R Soc Interface* **11**, doi:10.1098/rsif.2014.0543 (2014).

173   Chen, H. *et al.* Microfluidic models of physiological or pathological flow shear stress for cell biology, disease modeling and drug development. *TrAC Trends in Analytical Chemistry* (2019).

174   Sakariassen, K. S., Orning, L. & Turitto, V. T. The impact of blood shear rate on arterial thrombus formation. *Future Sci OA* **1**, FSO30, doi:10.4155/fso.15.28 (2015).

175   Balogh, P. & Bagchi, P. Three-dimensional distribution of wall shear stress and its gradient in red cell-resolved computational modeling of blood flow in in vivo-like microvascular networks. *Physiol Rep* **7**, e14067, doi:10.14814/phy2.14067 (2019).

176   van der Meer, A. D., Poot, A. A., Feijen, J. & Vermes, I. Analyzing shear stress-induced alignment of actin filaments in endothelial cells with a microfluidic assay. *Biomicrofluidics* **4**, 11103, doi:10.1063/1.3366720 (2010).

177   Shao, J. *et al.* Integrated microfluidic chip for endothelial cells culture and analysis exposed to a pulsatile and oscillatory shear stress. *Lab Chip* **9**, 3118-3125, doi:10.1039/b909312e (2009).

178   Tzima, E. *et al.* A mechanosensory complex that mediates the endothelial cell response to fluid shear stress. *Nature* **437**, 426-431, doi:nature03952 [pii]

10.1038/nature03952 (2005).

179   Booth, R. & Kim, H. Characterization of a microfluidic in vitro model of the blood-brain barrier (muBBB). *Lab Chip* **12**, 1784-1792, doi:10.1039/c2lc40094d (2012).

180   Wong, A. K., P, L. L., Boroda, N., Rosenberg, S. R. & Rabbany, S. Y. A Parallel-Plate Flow Chamber for Mechanical Characterization of Endothelial Cells Exposed to Laminar Shear Stress. *Cell Mol Bioeng* **9**, 127-138, doi:10.1007/s12195-015-0424-5 (2016).

181   Min, E. *et al.* Activation of Smad 2/3 signaling by low shear stress mediates artery inward remodeling. *bioRxiv*, 691980 (2019).

182   Kriesi, C. *et al.* Integrated Flow Chamber Device for Live Cell Microscopy. *Frontiers in bioengineering and biotechnology* **7**, 91 (2019).

183   Crum, R. J., Diestelkamp, W. S. & Krane, C. M. Pravastatin™ suppresses venous shear stress dependent induction of Aquaporin 1 protein expression in human umbilical vein endothelial cells in vitro. *Bios* **89**, 174-184 (2019).

184   Song, J. W. *et al.* Computer-controlled microcirculatory support system for endothelial cell culture and shearing. *Anal Chem* **77**, 3993-3999, doi:10.1021/ac050131o (2005).

185   Booth, R., Noh, S. & Kim, H. A multiple-channel, multiple-assay platform for characterization of full-range shear stress effects on vascular endothelial cells. *Lab Chip* **14**, 1880-1890, doi:10.1039/c3lc51304a (2014).

186   Ostrowski, M. A. *et al.* Multiplexed Fluid Flow Device to Study Cellular Response to Tunable Shear Stress Gradients. *Ann Biomed Eng* **44**, 2261-2272, doi:10.1007/s10439-015-1500-7 (2016).

187   Sinha, R. *et al.* A medium throughput device to study the effects of combinations of surface strains and fluid-flow shear stresses on cells. *Lab Chip* **15**, 429-439, doi:10.1039/c4lc01259c (2015).

188   Zhang, X., Huk, D., Wang, Q., Lincoln, J. & Zhao, Y. A microfluidic shear device that accommodates parallel high and low stress zones within the same culturing chamber. *Biomicrofluidics* **8**, 054106 (2014).

189   Voyvodic, P. L., Min, D. & Baker, A. B. A multichannel dampened flow system for studies on shear stress-mediated mechanotransduction. *Lab Chip* **12**, 3322-3330, doi:10.1039/c2lc40526a (2012).

190   Feng, S., Mao, S., Zhang, Q., Li, W. & Lin, J.-M. Online analysis of drug toxicity to cells with shear stress on an integrated microfluidic chip. *ACS sensors* **4**, 521-527 (2019).

191   Tkachenko, E., Gutierrez, E., Ginsberg, M. H. & Groisman, A. An easy to assemble microfluidic perfusion device with a magnetic clamp. *Lab Chip* **9**, 1085-1095, doi:10.1039/b812184b (2009).

192   Song, M. J., Dean, D. & Tate, M. L. K. In situ spatiotemporal mapping of flow fields around seeded stem cells at the subcellular length scale. *PLoS one* **5** (2010).

193   Shemesh, J. *et al.* Flow-induced stress on adherent cells in microfluidic devices. *Lab Chip* **15**, 4114-4127, doi:10.1039/c5lc00633c (2015).

194   Gray, B. L., Lieu, D. K., Collins, S. D., Smith, R. L. & Barakat, A. I. Microchannel platform for the study of endothelial cell shape and function. *Biomedical Microdevices* **4**, 9-16 (2002).

195   Hardy, B. S., Uechi, K., Zhen, J. & Pirouz Kavehpour, H. The deformation of flexible PDMS microchannels under a pressure driven flow. *Lab Chip* **9**, 935-938, doi:10.1039/b813061b (2009).

196   Gervais, T., El-Ali, J., Gunther, A. & Jensen, K. F. Flow-induced deformation of shallow microfluidic channels. *Lab Chip* **6**, 500-507, doi:10.1039/b513524a (2006).

197   Shah, R. K. & London, A. L. *Laminar flow forced convection in ducts: a source book for compact heat exchanger analytical data*. (Academic press, 2014).

198   Kim, H. W., Lim, J., Rhie, J. W. & Kim, D. S. Investigation of effective shear stress on endothelial differentiation of human adipose-derived stem cells with microfluidic screening device. *Microelectronic Engineering* **174**, 24-27 (2017).

199   Zheng, W. *et al.* A microfluidic flow-stretch chip for investigating blood vessel biomechanics. *Lab on a Chip* **12**, 3441-3450 (2012).

200   Chung, B. J., Robertson, A. & Peters, D. The numerical design of a parallel plate flow chamber for investigation of endothelial cell response to shear stress. *Computers & Structures* **81**, 535-546 (2003).

201   Sebastian, B. & Dittrich, P. S. Microfluidics to mimic blood flow in health and disease. *Annual review of fluid mechanics* **50**, 483-504 (2018).

202   Bhattacharjee, N., Urrios, A., Kang, S. & Folch, A. The upcoming 3D-printing revolution in microfluidics. *Lab Chip* **16**, 1720-1742, doi:10.1039/c6lc00163g (2016).

203   Papaioannou, T. G. & Stefanadis, C. Vascular wall shear stress: basic principles and methods. *Hellenic J Cardiol* **46**, 9-15 (2005).

204   Barbee, K. A., Davies, P. F. & Lal, R. Shear stress-induced reorganization of the surface topography of living endothelial cells imaged by atomic force microscopy. *Circ Res* **74**, 163-171, doi:10.1161/01.res.74.1.163 (1994).

205   Barbee, K. A. Changes in surface topography in endothelial monolayers with time at confluence: influence on subcellular shear stress distribution due to flow. *Biochem Cell Biol* **73**, 501-505, doi:10.1139/o95-055 (1995).

206   Kim, A. A., Nekimken, A. L., Fechner, S., O'Brien, L. E. & Pruitt, B. L. Microfluidics for mechanobiology of model organisms. *Methods Cell Biol* **146**, 217-259, doi:10.1016/bs.mcb.2018.05.010 (2018).

207   Zheng, W., Wang, Z., Zhang, W. & Jiang, X. A simple PDMS-based microfluidic channel design that removes bubbles for long-term on-chip culture of mammalian cells. *Lab on a Chip* **10**, 2906-2910 (2010).

208   Frye, K. *et al.* Cell Cycle-Dependent Dynamics of the Golgi-Centrosome Association in Motile Cells. *Cells* **9**, 1069 (2020).

209   Qin, X. *et al.* MicroRNA-19a mediates the suppressive effect of laminar flow on cyclin D1 expression in human umbilical vein endothelial cells. *Proceedings of the National Academy of Sciences* **107**, 3240-3244 (2010).

210   Rouleau, L., Farcas, M., Tardif, J.-C., Mongrain, R. & Leask, R. L. Endothelial cell morphologic response to asymmetric stenosis hemodynamics: effects of spatial wall shear stress gradients. *Journal of biomechanical engineering* **132** (2010).

211   Yamamoto, E. *et al.* Endothelial shear stress and plaque erosion: a computational fluid dynamics and optical coherence tomography study. *JACC: Cardiovascular Imaging* **12**, 374-375 (2019).

212   Sakamoto, N., Saito, N., Han, X., Ohashi, T. & Sato, M. Effect of spatial gradient in fluid shear stress on morphological changes in endothelial cells in response to flow. *Biochemical and biophysical research communications* **395**, 264-269, doi:10.1016/j.bbrc.2010.04.002 (2010).

213   Dolan, J. M., Meng, H., Singh, S., Paluch, R. & Kolega, J. High fluid shear stress and spatial shear stress gradients affect endothelial proliferation, survival, and alignment. *Ann Biomed Eng* **39**, 1620-1631, doi:10.1007/s10439-011-0267-8 (2011).

214   Mack, J. J. *et al.* NOTCH1 is a mechanosensor in adult arteries. *Nature communications* **8**, 1-19 (2017).

215   Zhao, X.-M., Xia, Y. & Whitesides, G. M. Soft lithographic methods for nano-fabrication. *Journal of Materials Chemistry* **7**, 1069-1074 (1997).

216   McDonald, J. C. *et al.* Fabrication of microfluidic systems in poly (dimethylsiloxane). *ELECTROPHORESIS: An International Journal* **21**, 27-40 (2000).

217   Whitesides, G. M., Ostuni, E., Takayama, S., Jiang, X. & Ingber, D. E. Soft lithography in biology and biochemistry. *Annual review of biomedical engineering* **3**, 335-373, doi:10.1146/annurev.bioeng.3.1.335 (2001).

218   Walsh Iii, D. I., Kong, D. S., Murthy, S. K. & Carr, P. A. Enabling microfluidics: from clean rooms to makerspaces. *Trends in biotechnology* **35**, 383-392 (2017).

219   Au, A. K., Lee, W. & Folch, A. Mail-order microfluidics: evaluation of stereolithography for the production of microfluidic devices. *Lab on a Chip* **14**, 1294-1301, doi:10.1039/c3lc51360b (2014).

220   Hong, S. J., Choi, S., Choi, Y., Allen, M. & May, G. S. 404-408 (IEEE).

221   Hupert, M. L. *et al.* Evaluation of micromilled metal mold masters for the replication of microchip electrophoresis devices. *Microfluidics and Nanofluidics* **3**, 1-11, doi:10.1007/s10404-006-0091-x (2007).

222   Guckenberger, D. J., de Groot, T. E., Wan, A. M. D., Beebe, D. J. & Young, E. W. K. Micromilling: a method for ultra-rapid prototyping of plastic microfluidic devices. *Lab on a Chip* **15**, 2364-2378, doi:10.1039/c5lc00234f (2015).

223   Yazdi, A. A. *et al.* 3D printing: an emerging tool for novel microfluidics and lab-on-a-chip applications. *Microfluidics and Nanofluidics* **20**, doi:10.1007/s10404-016-1715-4 (2016).

224   Garcia-Colomo, A., Wood, D., Martina, F. & Williams, S. W. A comparison framework to support the selection of the best additive manufacturing process for specific aerospace applications. *International Journal of Rapid Manufacturing, Underscience Publishers, UK*, 2 (2019).

225   Cumpston, B. H. *et al.* Two-photon polymerization initiators for three-dimensional optical data storage and microfabrication. *Nature* **398**, 51 (1999).

226   Saha, S. K. *et al.* Scalable submicrometer additive manufacturing. *Science* **366**, 105-109, doi:10.1126/science.aax8760 (2019).

227   Zhou, X., Hou, Y. & Lin, J. A review on the processing accuracy of two-photon polymerization. *AIP Advances* **5**, 030701, doi:Artn 030701

10.1063/1.4916886 (2015).

228   Jiang, X. *et al.* Controlling mammalian cell spreading and cytoskeletal arrangement with conveniently fabricated continuous wavy features on poly (dimethylsiloxane). *Langmuir* **18**, 3273-3280, doi:10.1021/la011668+ (2002).

229   Jeon, J. S., Chung, S., Kamm, R. D. & Charest, J. L. Hot embossing for fabrication of a microfluidic 3D cell culture platform. *Biomedical microdevices* **13**, 325-333 (2011).

230   Desai, S. P., Freeman, D. M. & Voldman, J. Plastic masters-rigid templates for soft lithography. *Lab Chip* **9**, 1631-1637, doi:10.1039/b822081f (2009).

231   Wang, Y. *et al.* Benchtop micromolding of polystyrene by soft lithography. *Lab Chip* **11**, 3089-3097, doi:10.1039/c1lc20281b (2011).

232   Nargang, T. M. *et al.* Liquid polystyrene: a room-temperature photocurable soft lithography compatible pour-and-cure-type polystyrene. *Lab Chip* **14**, 2698-2708, doi:10.1039/c4lc00045e (2014).

233   Wilson, M. E. *et al.* Fabrication of circular microfluidic channels by combining mechanical micromilling and soft lithography. *Lab Chip* **11**, 1550-1555, doi:10.1039/c0lc00561d (2011).

234   Becker, H. & Heim, U. Hot embossing as a method for the fabrication of polymer high aspect ratio structures. *Sensors and Actuators A: Physical* **83**, 130-135, doi:Doi 10.1016/S0924-4247(00)00296-X (2000).

235   Soper, S. A. *et al.*   (ACS Publications, 2000).

236   Becker, H. & Gartner, C. Polymer microfabrication technologies for microfluidic systems. *Anal Bioanal Chem* **390**, 89-111, doi:10.1007/s00216-007-1692-2 (2008).

237   Yang, S. & DeVoe, D. L. in *Microfluidic Diagnostics*   115-123 (Springer, 2013).

238   Martinez-Duarte, R. & Madou, M. SU-8 photolithography and its impact on microfluidics. *Microfluidics and Nanofluidics Handbook*, 231-268 (2011).

239   Yu, J. Z., Korkmaz, E., Berg, M. I., LeDuc, P. R. & Ozdoganlar, O. B. Biomimetic scaffolds with three-dimensional undulated microtopographies. *Biomaterials* **128**, 109-120, doi:10.1016/j.biomaterials.2017.02.014 (2017).

240   Blaga, A. & Yamasaki, R. S. Surface microcracking induced by weathering of polycarbonate sheet. *Journal of Materials Science* **11**, 1513-1520, doi:Doi 10.1007/Bf00540886 (1976).

241   Long, T. S. & Sokol, R. J. Molding polycarbonate: Moisture degradation effect on physical and chemical properties. *Polymer Engineering & Science* **14**, 817-822, doi:DOI 10.1002/pen.760141202 (1974).

242   Camino, G., Lomakin, S. M. & Lazzari, M. Polydimethylsiloxane thermal degradation Part 1. Kinetic aspects. *Polymer* **42**, 2395-2402, doi:Doi 10.1016/S0032-3861(00)00652-2 (2001).

243   Yang, F. Viscosity measurement of polycarbonate by using a penetration viscometer. *Polymer Engineering & Science* **37**, 101-104, doi:DOI 10.1002/pen.11650 (1997).

244   Lee, L. H. Relationships between surface wettability and glass temperatures of high polymers. *Journal of Applied Polymer Science* **12**, 719-730 (1968).

245   Gilman, J. J. Direct measurements of the surface energies of crystals. *Journal of applied physics* **31**, 2208-2218, doi:Doi 10.1063/1.1735524 (1960).

246   Karthikeyan, K. & Sujatha, L. Study of Permissible Flow Rate and Mixing Efficiency of the Micromixer Devices. *International Journal of Chemical Reactor Engineering* **17**, doi:10.1515/ijcre-2018-0047 (2019).

247   Nagrath, S. *et al.* Isolation of rare circulating tumour cells in cancer patients by microchip technology. *Nature* **450**, 1235-1239, doi:10.1038/nature06385 (2007).

248   Liu, Z. *et al.* Rapid isolation of cancer cells using microfluidic deterministic lateral displacement structure. *Biomicrofluidics* **7**, 11801, doi:10.1063/1.4774308 (2013).

249   Rettig, J. R. & Folch, A. Large-scale single-cell trapping and imaging using microwell arrays. *Analytical chemistry* **77**, 5628-5634, doi:10.1021/ac0505977 (2005).

250   Liu, W. *et al.* Microcryogels as injectable 3-D cellular microniches for site-directed and augmented cell delivery. *Acta Biomater* **10**, 1864-1875, doi:10.1016/j.actbio.2013.12.008 (2014).

251   Tan, J. L. *et al.* Cells lying on a bed of microneedles: an approach to isolate mechanical force. *Proceedings of the National Academy of Sciences* **100**, 1484-1489, doi:10.1073/pnas.0235407100 (2003).

252   Taylor, R. E. *et al.* Sacrificial layer technique for axial force post assay of immature cardiomyocytes. *Biomed Microdevices* **15**, 171-181, doi:10.1007/s10544-012-9710-3 (2013).

253   Huh, D. *et al.* Reconstituting organ-level lung functions on a chip. *Science* **328**, 1662-1668, doi:10.1126/science.1188302 (2010).

254   Kim, H. J., Li, H., Collins, J. J. & Ingber, D. E. Contributions of microbiome and mechanical deformation to intestinal bacterial overgrowth and inflammation in a human gut-on-a-chip. *Proceedings of the National Academy of Sciences* **113**, E7-E15, doi:10.1073/pnas.1522193112 (2016).

255   Pavesi, A. *et al.* Controlled electromechanical cell stimulation on-a-chip. *Sci Rep* **5**, 11800, doi:10.1038/srep11800 (2015).

256   Koerner, T., Brown, L., Xie, R. & Oleschuk, R. D. Epoxy resins as stamps for hot embossing of microstructures and microfluidic channels. *Sensors and Actuators B: Chemical* **107**, 632-639, doi:10.1016/j.snb.2004.11.035 (2005).

257   Nekimken, A. L. *et al.* Pneumatic stimulation of C. elegans mechanoreceptor neurons in a microfluidic trap. *Lab on a Chip* **17**, 1116-1127, doi:10.1039/c6lc01165a (2017).

258   Long, Z., Shen, Z., Wu, D., Qin, J. & Lin, B. Integrated multilayer microfluidic device with a nanoporous membrane interconnect for online coupling of solid-phase extraction to microchip electrophoresis. *Lab Chip* **7**, 1819-1824, doi:10.1039/b711741h (2007).

259   Warkiani, M. E., Tay, A. K. P., Guan, G. & Han, J. Membrane-less microfiltration using inertial microfluidics. *Scientific reports* **5**, 11018, doi:ARTN 11018

10.1038/srep11018 (2015).

260   Vernetti, L. *et al.* Functional Coupling of Human Microphysiology Systems: Intestine, Liver, Kidney Proximal Tubule, Blood-Brain Barrier and Skeletal Muscle. *Sci Rep* **7**, 42296, doi:10.1038/srep42296 (2017).

261 Unger, M. A., Chou, H.-P., Thorsen, T., Scherer, A. & Quake, S. R. Monolithic microfabricated valves and pumps by multilayer soft lithography. *Science* **288**, 113-116, doi:10.1126/science.288.5463.113 (2000).

262 Berthier, E., Young, E. W. & Beebe, D. Engineers are from PDMS-land, Biologists are from Polystyrenia. *Lab Chip* **12**, 1224-1237, doi:10.1039/c2lc20982a (2012).

263 Wang, M., Li, J., Ngo, K. & Xie, H. Silicon molding techniques for integrated power MEMS inductors. *Sensors and Actuators A: Physical* **166**, 157-163, doi:10.1016/j.sna.2010.12.012 (2011).

264 SYLGARD™ 184 Silicone Elastomer Technical Datasheet. (Dow Corning, Inc., 2019).

265 Biela, S. A., Su, Y., Spatz, J. P. & Kemkemer, R. Different sensitivity of human endothelial cells, smooth muscle cells and fibroblasts to topography in the nano–micro range. *Acta biomaterialia* **5**, 2460-2466, doi:10.1016/j.actbio.2009.04.003 (2009).

266 Kim, D.-H. *et al.* Mechanosensitivity of fibroblast cell shape and movement to anisotropic substratum topography gradients. *Biomaterials* **30**, 5433-5444, doi:10.1016/j.biomaterials.2009.06.042 (2009).

267 Curtis, A. S. G., Dalby, M. & Gadegaard, N. Cell signaling arising from nanotopography: implications for nanomedical devices. *Nanomedicine (Lond)* **1**, 67-72, doi:10.2217/17435889.1.1.67 (2006).

268 Biggs, M. J. P. *et al.* Adhesion formation of primary human osteoblasts and the functional response of mesenchymal stem cells to 330 nm deep microgrooves. *Journal of the Royal Society Interface* **5**, 1231-1242 (2008).

269 Brammer, K. S., Choi, C., Frandsen, C. J., Oh, S. & Jin, S. Hydrophobic nanopillars initiate mesenchymal stem cell aggregation and osteo-differentiation. *Acta biomaterialia* **7**, 683-690, doi:10.1016/j.actbio.2010.09.022 (2011).

270 Ermis, M., Antmen, E. & Hasirci, V. Micro and Nanofabrication methods to control cell-substrate interactions and cell behavior: A review from the tissue engineering perspective. *Bioactive materials* **3**, 355-369, doi:10.1016/j.bioactmat.2018.05.005 (2018).

271 Park, S. H. *et al.* Fabrication of nano-precision PDMS replica using two-photon photopolymerization and vacuum pressure difference technique. *BULLETIN-KOREAN CHEMICAL SOCIETY* **25**, 1119-1120 (2004).

272 Block, I. D., Chan, L. L. & Cunningham, B. T. Large-area submicron replica molding of porous low-k dielectric films and application to photonic crystal biosensor fabrication. *Microelectronic Engineering* **84**, 603-608 (2007).

273 Losic, D., Mitchell, J. G., Lal, R. & Voelcker, N. H. Rapid fabrication of micro - and nanoscale patterns by replica molding from diatom biosilica. *Advanced Functional Materials* **17**, 2439-2446 (2007).

274 Chidambaram, N., Kirchner, R., Altana, M. & Schift, H. High fidelity 3D thermal nanoimprint with UV curable polydimethyl siloxane stamps. *Journal of Vacuum Science & Technology B, Nanotechnology and Microelectronics: Materials, Processing, Measurement, and Phenomena* **34**, 06K401 (2016).

275 O'Neill, A., Soo Hoo, J. & Walker, G. Rapid curing of PDMS for microfluidic applications. *Lab on a Chip. Chips & Tips. http://www. rsc. org/Publishing/Journals/lc/Chips_and_Tips/index. asp* (2006).

276 Smit, R. J. M. & van Houten, J. G. A. Large Strain Behaviour of Polycarbonate. *EUT, Faculty of Mechanical Engineering Report No. WFW* **94** (1994).

277 Robin, C. J., Vishnoi, A. & Jonnalagadda, K. N. Mechanical behavior and anisotropy of spin-coated SU-8 thin films for MEMS. *Journal of Microelectromechanical Systems* **23**, 168-180 (2013).

278   Tsuchiya, T. Evaluation of mechanical properties of MEMS materials and their standardization. *Reliability of MEMS*, 1-25 (2008).

279   Merkel, T. C., Bondar, V. I., Nagai, K., Freeman, B. D. & Pinnau, I. Gas sorption, diffusion, and permeation in poly (dimethylsiloxane). *Journal of Polymer Science Part B: Polymer Physics* **38**, 415-434, doi:Doi 10.1002/(Sici)1099-0488(20000201)38:3<415::Aid-Polb8>3.0.Co;2-Z (2000).

280   Halldorsson, S., Lucumi, E., Gomez-Sjoberg, R. & Fleming, R. M. T. Advantages and challenges of microfluidic cell culture in polydimethylsiloxane devices. *Biosens Bioelectron* **63**, 218-231, doi:10.1016/j.bios.2014.07.029 (2015).

281   Oh, K. W. & Ahn, C. H. A review of microvalves. *Journal of Micromechanics and Microengineering* **16**, R13-R39, doi:10.1088/0960-1317/16/5/r01 (2006).

282   Roy, E., Galas, J. C. & Veres, T. Thermoplastic elastomers for microfluidics: towards a high-throughput fabrication method of multilayered microfluidic devices. *Lab Chip* **11**, 3193-3196, doi:10.1039/c1lc20251k (2011).

283   Lee, L. H. Mechanisms of thermal degradation of phenolic condensation polymers. I. Studies on the thermal stability of polycarbonate. *Journal of Polymer Science Part A: General Papers* **2**, 2859-2873 (1964).
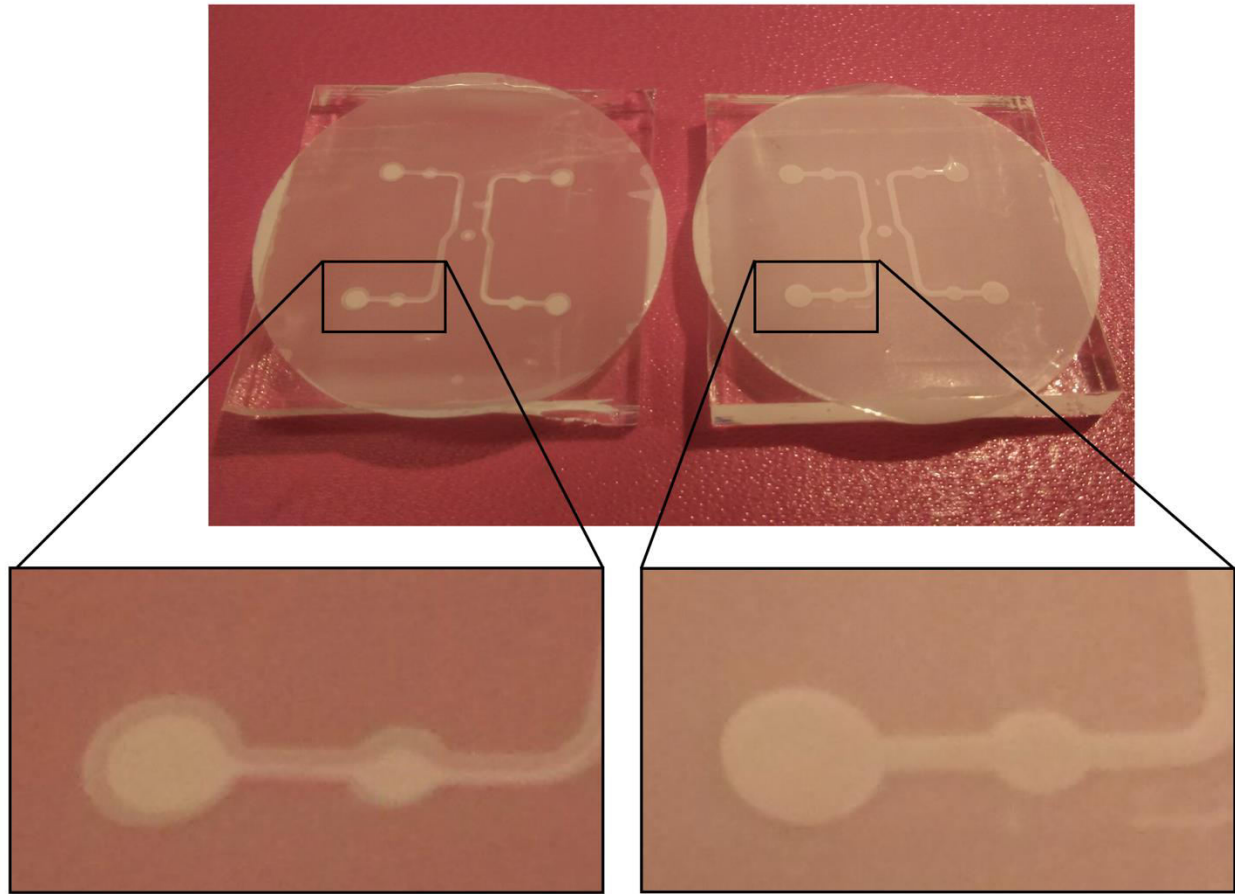
Appendix

Appendix 1.1
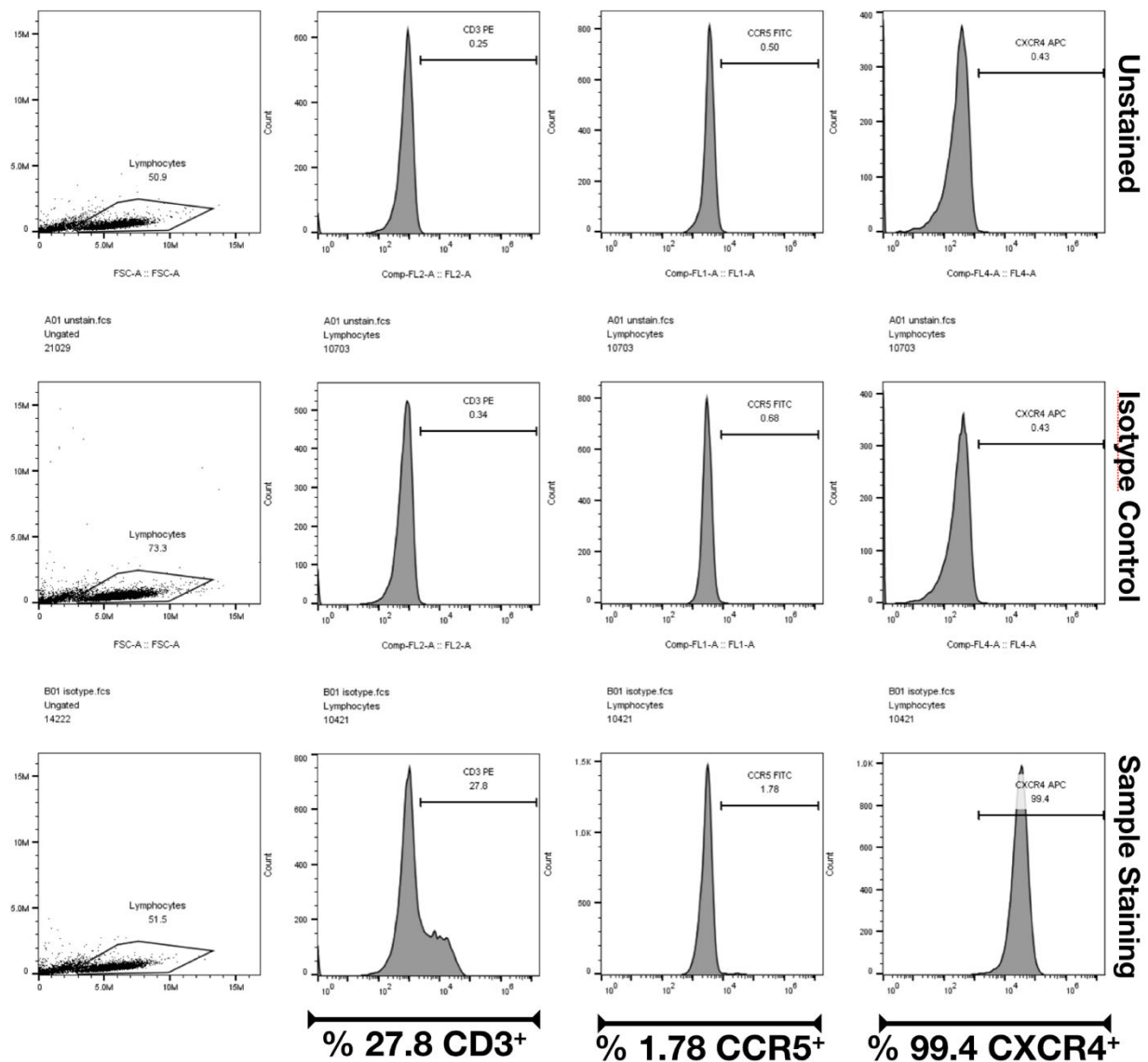
Receptor expression analysis data for Jurkat cells showing %99.4 CXCR4 expression which is the receptor for CXCL12 chemokine.
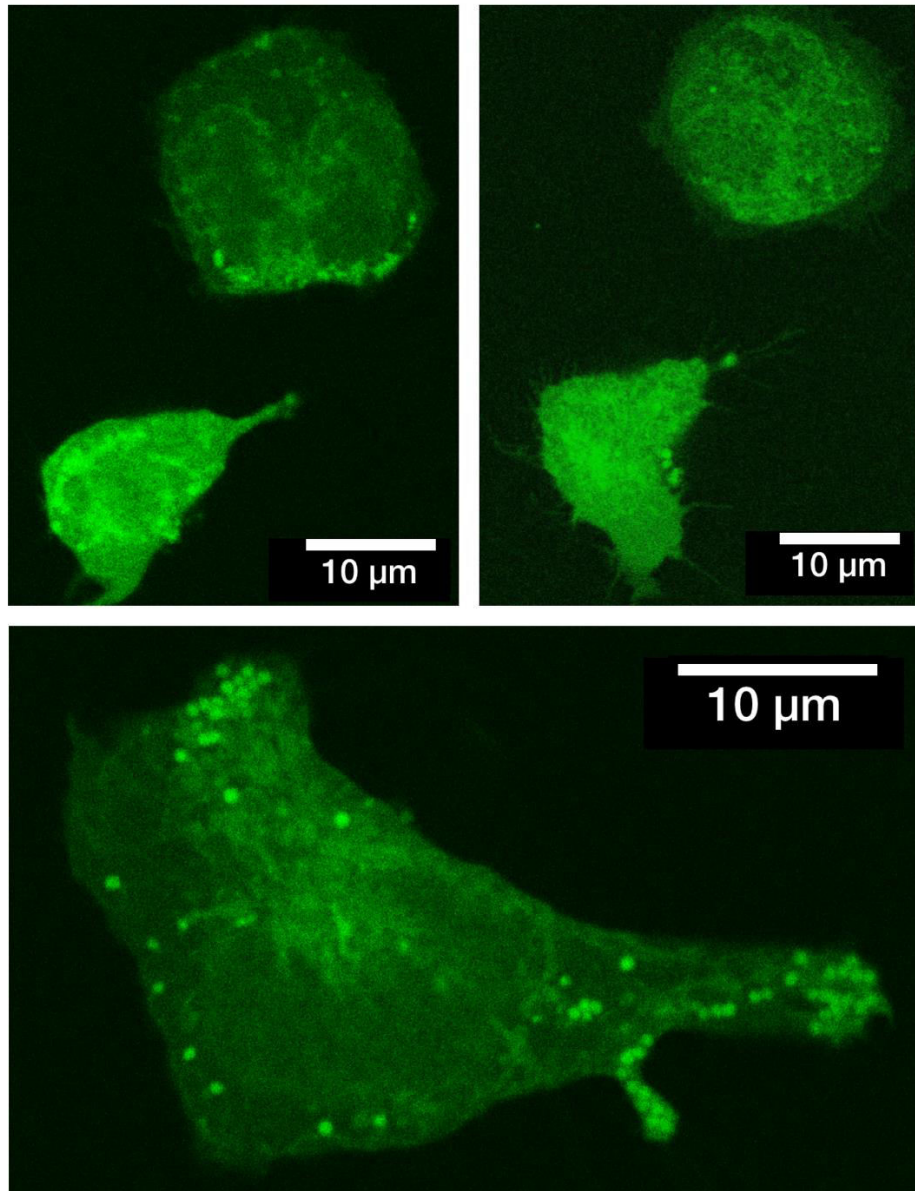
Appendix 1.2

Comparison of two different membrane integration techniques. (left) A PC membrane is integrated to a microfluidic channel using PDMS prepolymer as an intermediate adhesive layer. In short, PDMS was mixed with its curing agent with 10:1 ratio. Later, the PDMS prepolymer was diluted in Toluene with 1:1 mass ratio. The diluted PDMS prepolymer was poured on a pre-cleaned glass slide and spun 3 seconds at 500 rpm and 60 seconds at 1500 rpm, respectively, to obtain a 4 μm thick layer of PDMS prepolymer on the glass slide [1]. A coated glass slide was then stamped against the patterned surface of the PDMS microchannel. Finally, the membrane was brought in contact with the microchannel for bonding. Assembly was maintained at 60 ^{o}C in an oven for 2 hours for the curing of the PDMS prepolymer to induce irreversible bonding. (right) A PC membrane integrated to a microfluidic channel with APTES treatment and subsequent oxygen plasma bonding (details of the fabrication are in the main text). Unlike the first technique, here the membrane was bonded to the PDMS with covalent bonding to ensure that only the region of the membrane that is in contact with the PDMS was bonded while the rest of the membrane remained intact. However, in the first technique, the diluted PDMS prepolymer was absorbed by the membrane, partially sealing some regions of the membrane that were supposed to remain intact (see the insets). This resulted in a narrowed effective membrane region which affected adversely the gradient generation mechanism. Furthermore, the intermediate PDMS prepolymer layer required very careful handling of the membrane since contamination of membrane with the PDMS prepolymer could lead to irreversible clogging of

the membrane. These issues caused a low success rate, especially during the alignment of the two PDMS layers where any relative motion between two layers resulted in membrane clogging. Finally, while the integration of the membrane to the PDMS layer occurred instantaneously in the APTES technique, it required subsequent curing steps of the assembly in the adhesive PDMS prepolymer technique which, in turn, increased total fabrication time.
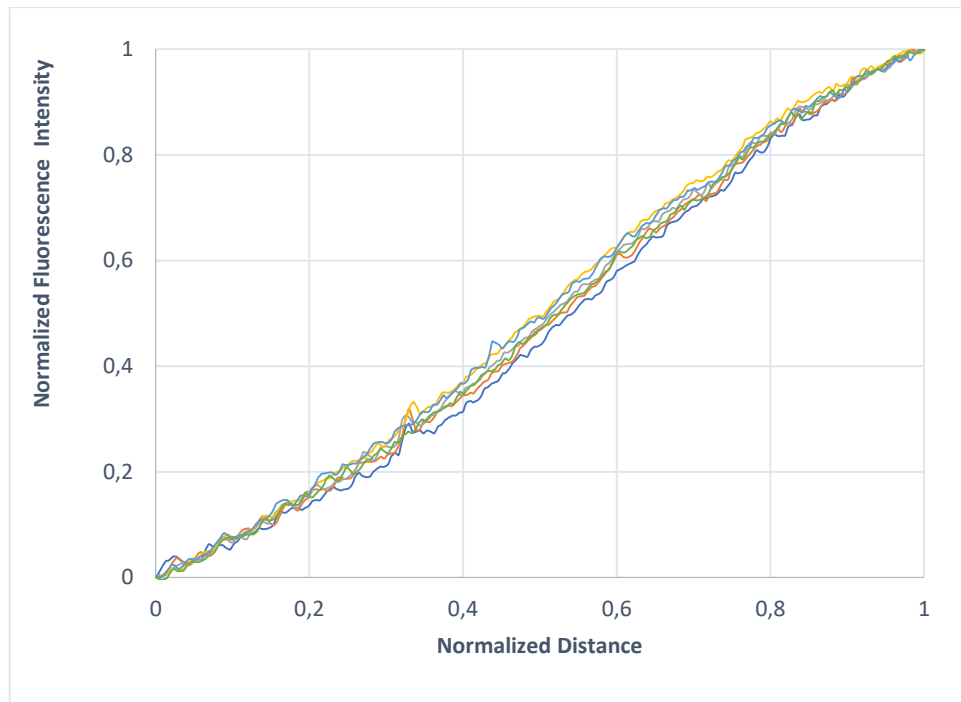
[1] Wu, H., Huang, B., & Zare, R. N. (2005). Construction of microfluidic chips using polydimethylsiloxane for adhesive bonding. Lab on a Chip, 5(12), 1393-1398.

Appendix 1.3

High resolution images (63x) of Jurkat cells stained with CellTracker Green BOPIDY in flow-free microfluidic gradient chamber.

Appendix 1.4

Plot displaying stable linear concentration gradient over time in flow-free chamber (blue line = 0 min.; orange line = 30 min.; grey line = 60 min.; yellow line = 90 min.; red line = 120 min.; green line = 150 min.).

Appendix 2.1

Analytical model of sidewall deflection:

Definitions

t = Thickness of the wall (50 $\times 10^{-6}$m)

h = Height of the wall (251.8 $\times 10^{-6}$ m)

L = Length of the wall, i.e. width (2 $\times 10^{-2}$ m) P = Pressure (5 PSI = 34473.8 N/m^2)

ω = Force per unit height (N/m)

$u(x)$ = Wall deflection (m)

E = Young's modulus (N/m^2)

I = Second moment of area (m^4)

For beams with rectangular cross-section, $\quad I = \dfrac{L \cdot t^3}{12}$

v = Poisson's ratio: $-\dfrac{d\varepsilon_y}{d\varepsilon_x}$, unitless. For PDMS, $v = 0.5$

Eq. 3.2 Timoshenko's beam theory:

κ = shear coefficient

G = shear modulus

A = cross-section area of the beam ($t \times L$)
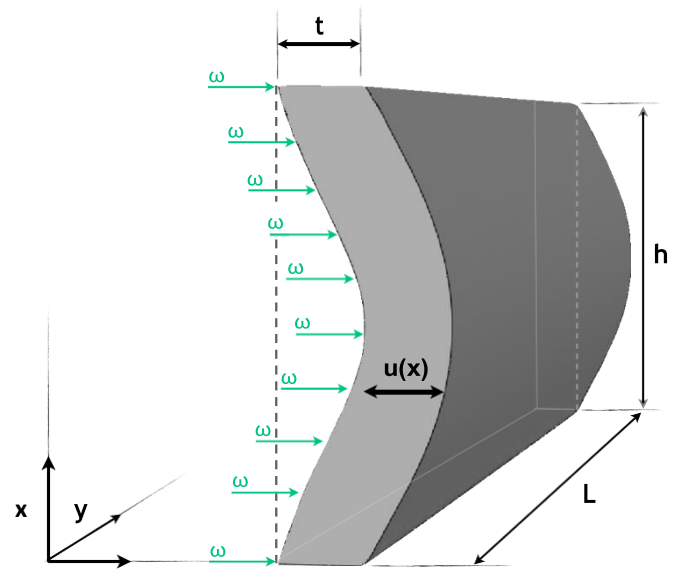
Shear deformation:

u_{max} at $x = h/2$

can be calculated with the following conversions:

$\omega = P \cdot L$

$$I \quad = \frac{L \cdot t^3}{12} \qquad \text{for rectangular cross-section}$$

$$\kappa = \frac{10(1+v)}{12+11v} \qquad \text{for rectangular cross-section}$$

$$G = \frac{E}{2(1+v)} \qquad \text{assuming elastic and isotropic material}$$

Yielding Eq. 4 in the main text.

Schematic of an analytical model of deformable sidewalls. This nomenclature is somewhat counterintuitive because we're considering a sidewall as a beam. In a beam, the region between two fixed pointsis the length; in a sidewall, this x-dimension is the height. Likewise, the width of a beam corresponds to the length of the channel (y), and the thickness of a beam corresponds to the width of the channel (z).
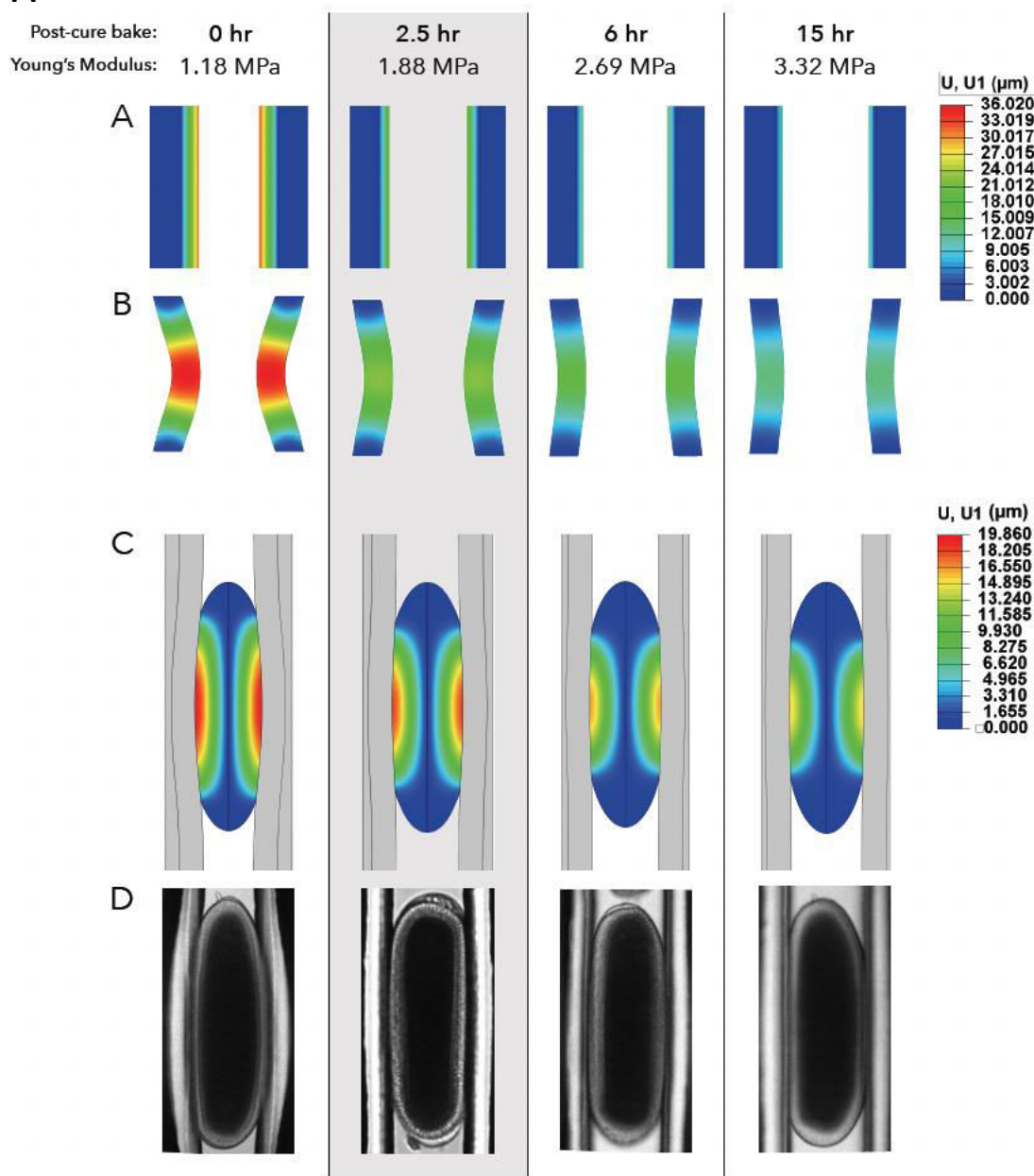
Appendix 2.2
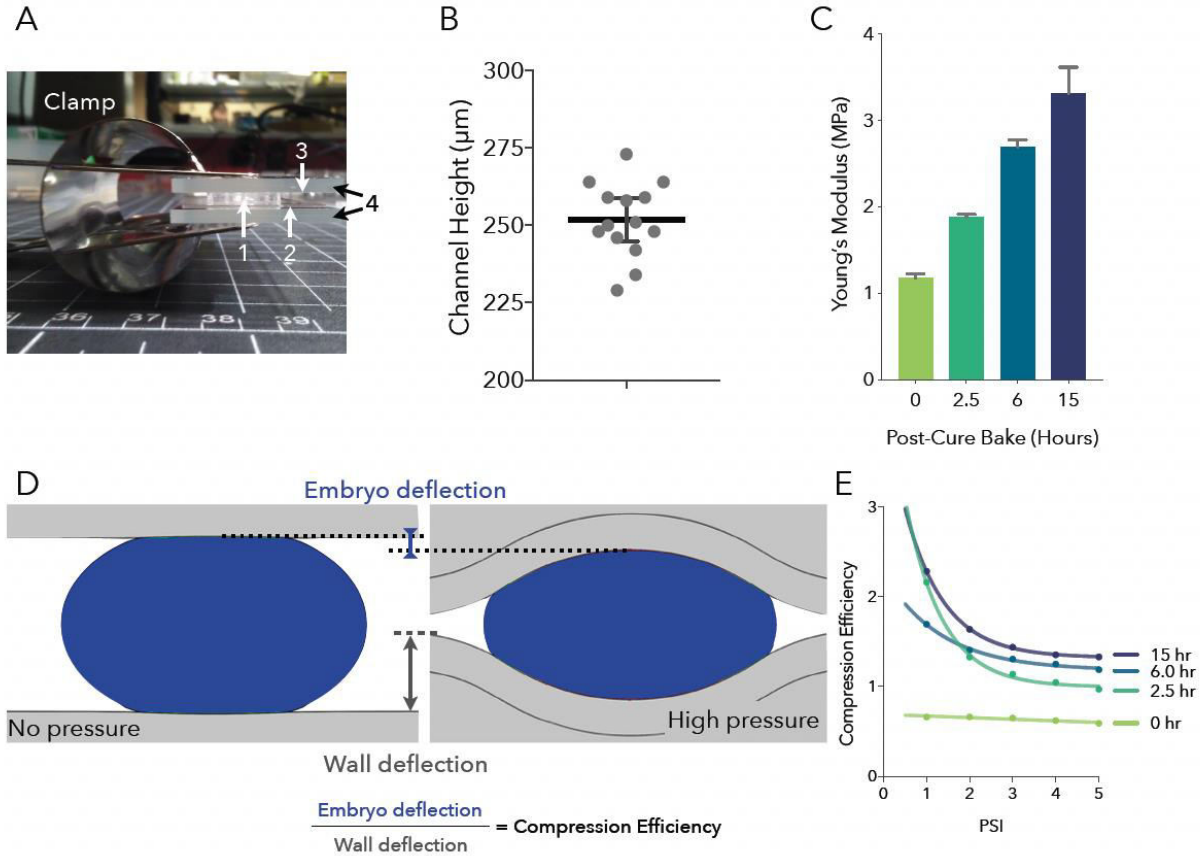
(A) Photograph of the microfluidic device during post-bake. A polycarbonate sheet (1) covered the PDMS-glass assembly (2, 3). The assembly was held between two thick glass slides (4) and clamped to ensure physical contact between PDMS and the coverslip while curing. Marks are cm. **(B)** Profilometry measurements of channel height show a mean of 251.8 μm with uniformity (1 − σ/μ × 100) > 95%. **(C)** Young's modulus of 50 μm sidewalls with differential post-cure baking. Deflection was measured at 10 points and calculated by Eq. 6. SEM bars. **(D)** Illustration of "compression efficiency" parameter – the ratio of embryo deflection to wall deflection. Compression efficiency measures a deformable wall's preference for compressing over wrapping. **(E)** Plot of compression efficiency over 5 PSI for channels with a range of post-bake durations. In the no-bake condition (0 hours), sidewalls are deflected with minimal embryo compression. As the rigidity of the walls increases, compression efficiency increases. Simulation results in **Appendix 2.4.**
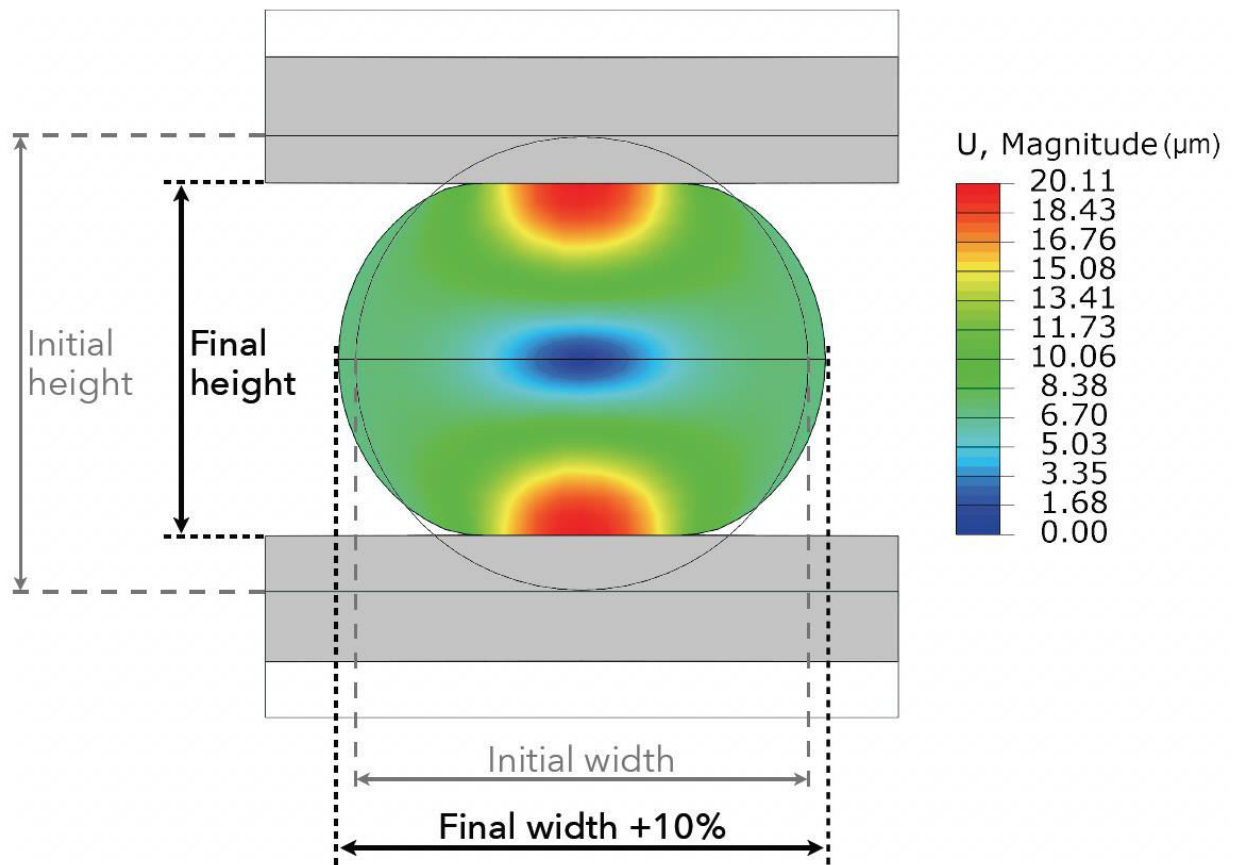
Appendix 2.3
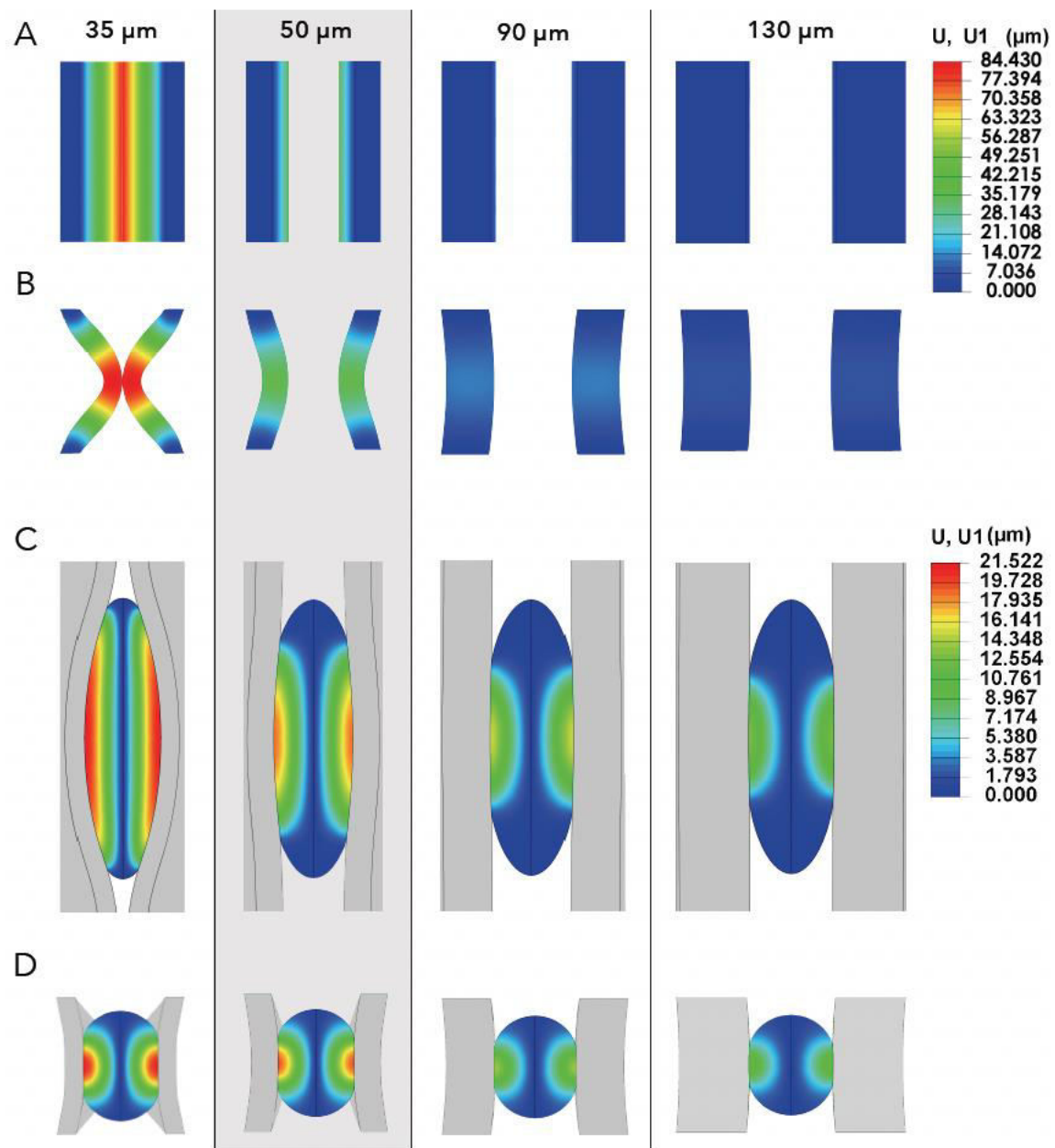
Simulation results of uniaxial node displacement at 5 PSI with variable wall thickness. **(A, B)** Empty channel, top view and side section. 35 μm walls close completely. **(C, D)** Channel with embryo, top view and side section. 35 μm walls showed heavy wrapping around the embryo, while 90+= μm walls showed low displacement resulting in low compression. 50 μm walls (shaded) were selected.

Appendix 2.4

Simulation results and micrographs of embryo compression at 5 PSI with variable wall rigidity. 50 μm thick walls were given a range of Young's modulus as a result of variable post-bake curing times **(Appendix 2.2C)**. **(A, B)** Empty channel, top view and side section. **(C)** Channel with embryo, top view **(side section in Figure 2.2E)**. Less rigid walls showed greater wrapping around the embryo. **(D)** Micrographs from experimental results. 2.5-hour post-cure bake (shaded) was selected.
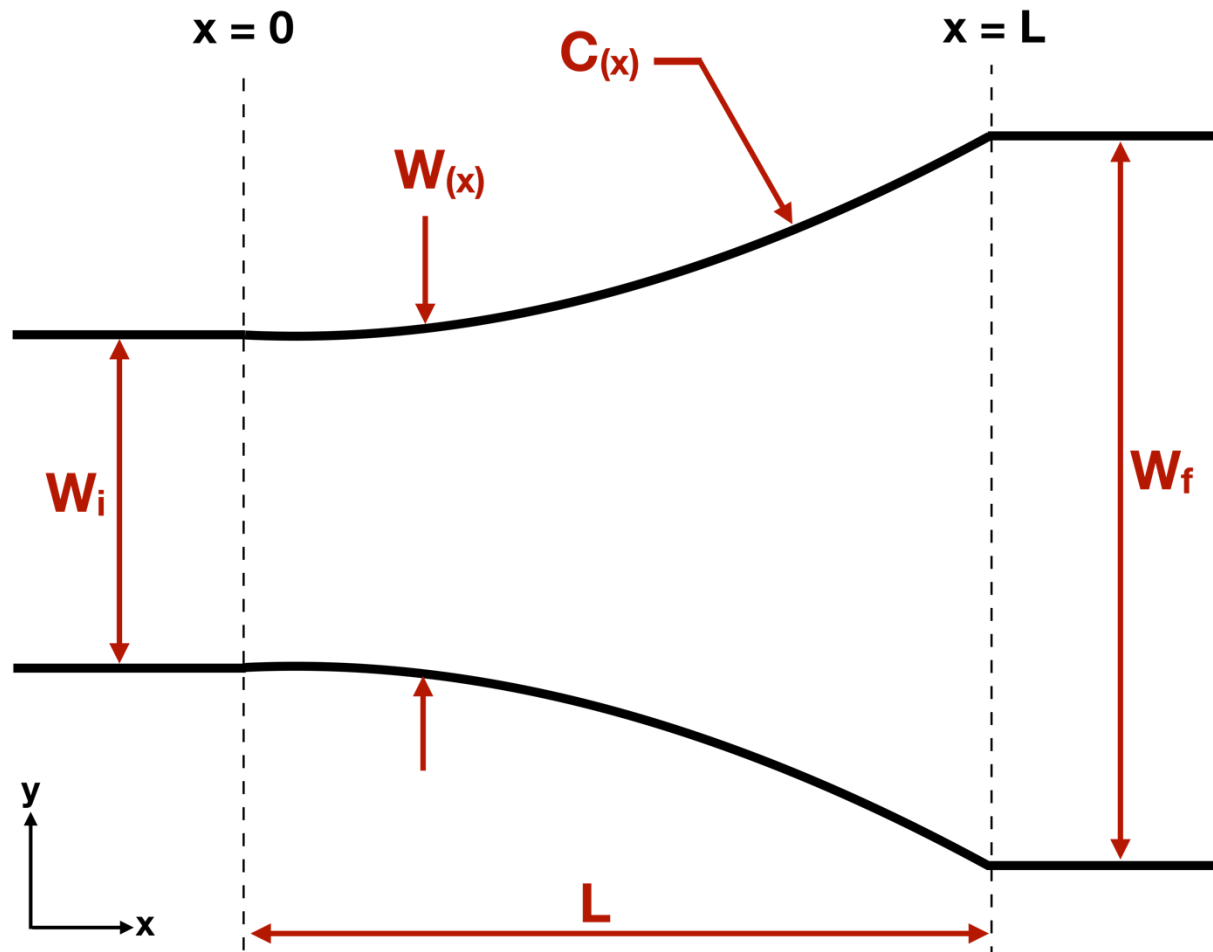
Appendix 2.5

Simulation results of embryo compression between two rigid walls such that lateral expansion is 10%. Before width expands, height decreases (red). As a result, the inferred compression is substantially larger than 10%.

Appendix 2.6

Embryo width   Max: 195 µm   Mean: 180 µm   Min: 160 µm
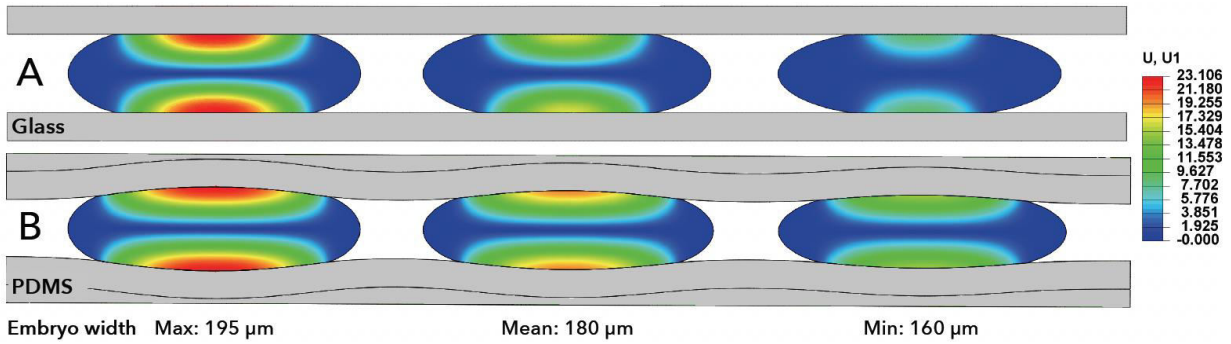
Flexible walls are more consistent than rigid glass when compressing a distribution of widths. Simulation of embryos of maximum, median, and minimum width at Stage 5. **(A)** When compressed by rigid glass, the channel width is consistent, applying more compression to wider embryos. **(B)** When compressed by flexible PDMS, the channel width is unique to each embryo, which resists deformation as a function of width. This results in a more consistent compression.

Appendix 3.1

Annotations of the parameters used for analytical characterization of the streamwise wall shear stress gradients in the microfluidic chip.

Appendix 3.2

he solution of the Navier-Stokes equations for the steady-state laminar flow of an incompressible Newtonian fluid between two infinitely long parallel plates leads to a well-known flow regime known as Hele-Shaw flow. Since the microfluidic channels generally have low aspect ratio (i.e. height << width), the hydrodynamic characterization of the flow can be initially simplified with this parallel plate assumption. The parabolic flow profile of Hele-Shaw flow demonstrates a parabolic velocity distribution across the height of the gap in the following form

$$v(z) = \frac{6}{h^2} z(h - z)\underline{v}$$ (eq. A1)

where $\underline{v}$ is the mean velocity, h is the height of the gap, and z is the coordinate along the height of the gap starting as zero from the bottom surface of the microchannel. In this way, the wall shear stress acting on the cells in the microchannel regions with uniform width can be approximated as

$$\tau_w = \frac{6\mu Q}{wh^2}$$ (eq. A2)

where μ is the dynamic viscosity of the fluid, Q is the volumetric flow rate, and w is the width and h is the height of the microchannel. Microchannel regions with changing width are expected to have linear stream-wise shear stress gradients (i.e., along the x axis) in order to expose cells consistently to the same gradient slope in the given region. The linear shear gradient can be expressed in the form of

$$\tau_w(x) = ax + b$$ (eq. A3)

where a and b can be found by solving this equation at the boundaries of the linear shear stress gradient regions. Using the Hele-Shaw flow assumption, the wall shear stress at the beginning of the linear shear stress gradient region can be calculated as

$$\tau_w(x)_{[x=0]} = b = \frac{6\mu Q}{w_i h^2}$$ (eq. A4)

where w_i is the width of the microchannel at the beginning of the linear shear stress gradient region at $x = 0$ **(Appendix 3.2)**. Using the same Hele-Shaw flow assumption, the wall shear stress at the end of the linear shear stress gradient region can be similarly found as

$$\tau_w(x)_{[x=L]} = aL + \frac{6\mu Q}{w_i h^2} = \frac{6\mu Q}{w_f h^2}$$ (eq. A5)

where L is the length of the region and w_f is the final width of the linear shear stress gradient region at $x = L$. From this equation a can be found as

$$a = \frac{6\mu Q}{h^2} \frac{(w_i - w_f)}{L w_i w_f} \qquad \text{(eq. A6)}$$

which also represents the slope of the linear wall shear stress gradient generated in x-direction. Using these parameters, the magnitude of this wall shear stress at the given point along the x axis can then be written as

$$\tau_w(x) = \frac{6\mu Q}{h^2} \frac{(w_i - w_f)}{L w_i w_f} x + \frac{6\mu Q}{w_i h^2} \qquad \text{(eq. A7)}$$

The formula for the function that describes the microchannel width can be derived from this equation as
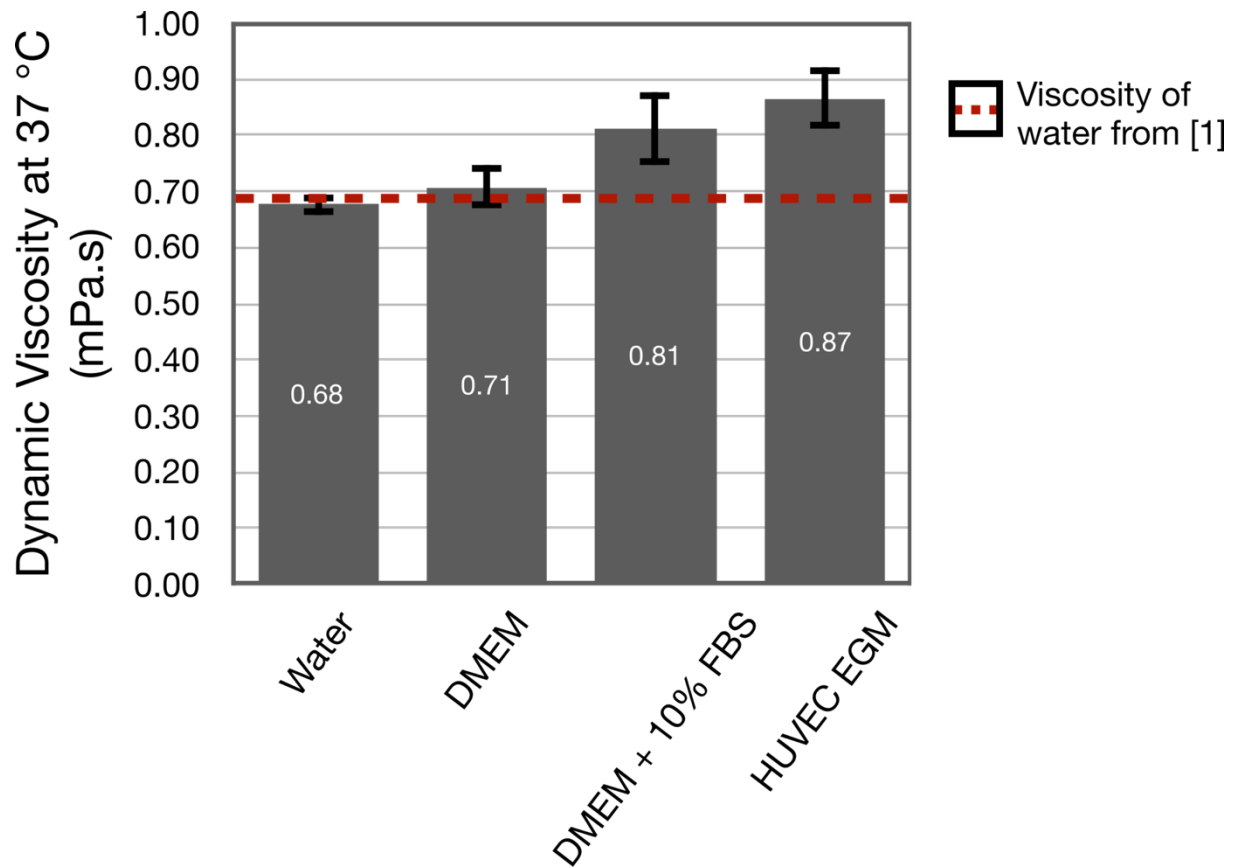
$$w(x) = \frac{L w_i w_f}{(w_i - w_f)x + L w_f} \qquad \text{(eq. A8)}$$

Since there are two symmetrically curved sidewalls at each side of the microchannel that defines the width of the channel, the formula needed for plotting each sidewall becomes

$$c(x) = \frac{L w_i w_f}{2((w_i - w_f)x + L w_f)} \qquad \text{(eq. A9)}$$

which can be used to model the microchannel regions with linear shear stress gradient in a CAD software.

Appendix 3.3

Dynamic viscosity values of various cell culture media at 37°C. The average value of the water viscosity was 2.89% different than the value in the literature. Addition of 10% FBS (Fetal Bovine Serum) into DMEM (Dulbecco's Modified Eagle Medium) increased dynamic viscosity of the media. The complete HUVEC EGM (Human Umbilical Cord Vascular Endothelial Cell Growth Media) that was used throughout this study had even higher viscosity. Data are presented as mean ± SD.

Appendix 3.4
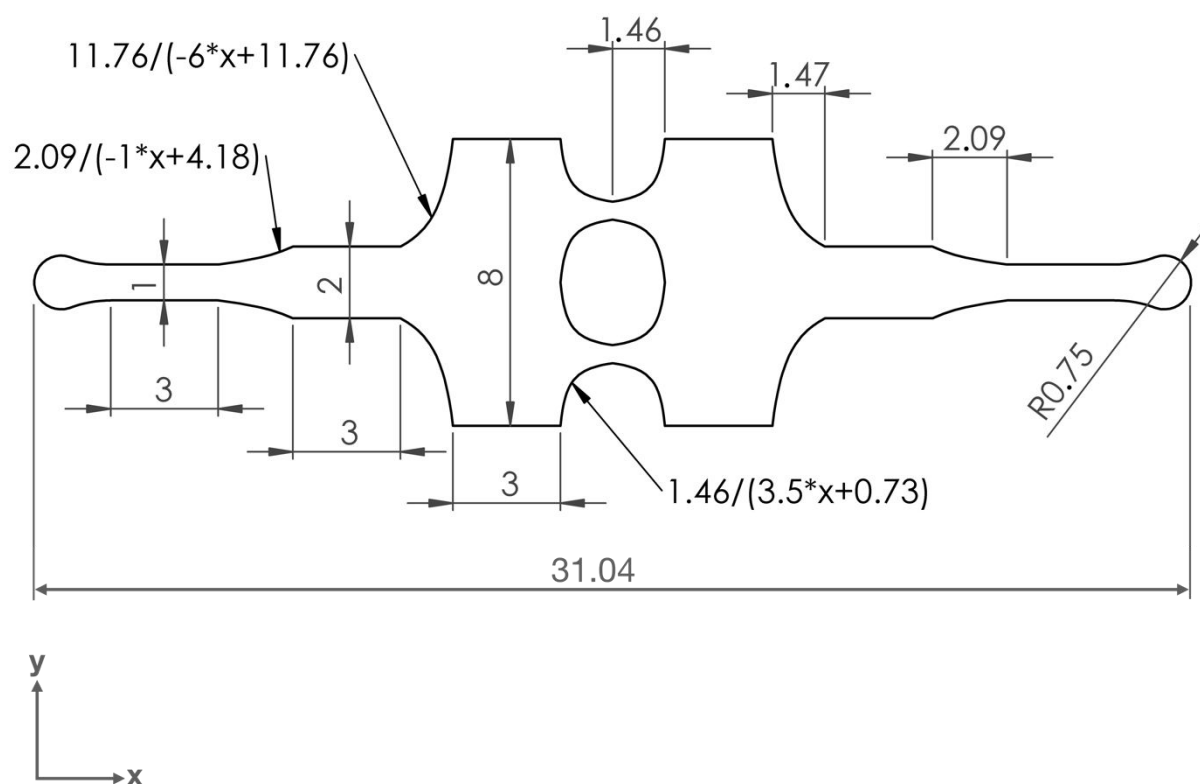
The dimensions of the microfluidic chip used in the experiments. The equations describing the curved sidewalls were generated using Equation 6 in the manuscript. The height of the different microchannels regions is constant and equal to 200 µm. The microfluidic chip is symmetric with respect to x- and y-axes. All units are in mm.

Appendix 3.5

Flow Direction →
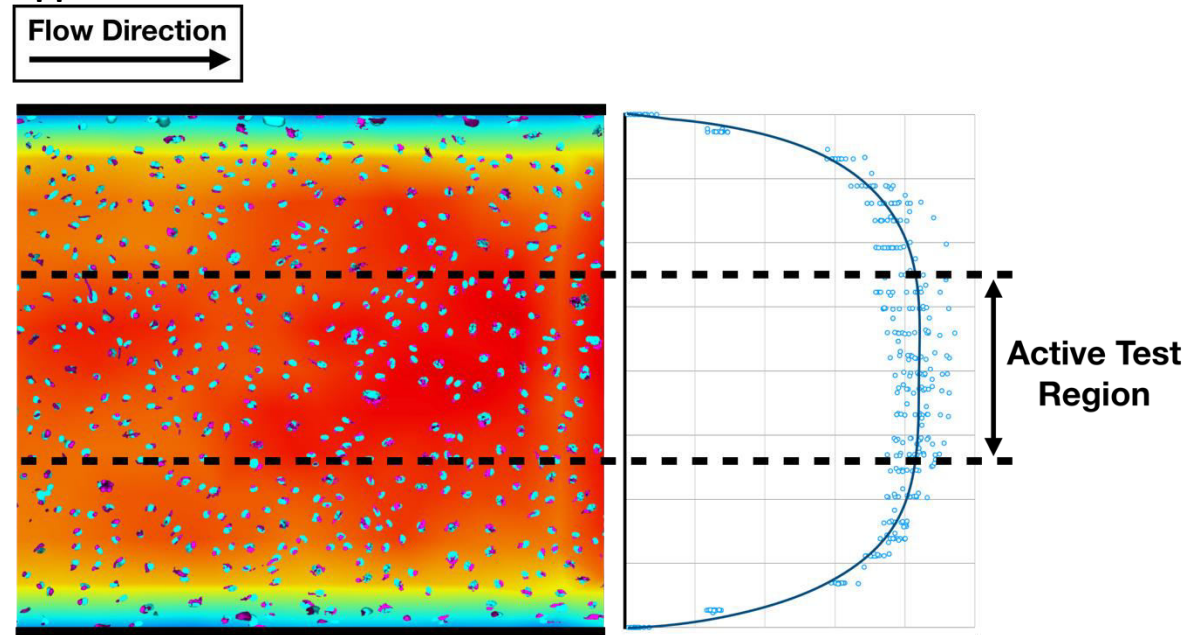
Computational Fluid Dynamics (CFD) simulation results showed the distribution of the shear stress across the bottom surface of the microchannel where the endothelial cells were seeded. Fluorescent images of Golgi and nuclei of the human umbilical vein endothelial cells (HUVECs) overlaid with the shear stress map. Due to the sidewalls, the shear stress exerted on the cells was lower at either side of the microchannel. Therefore, only the HUVECs in the central region of the microchannel (shown between two parallel dashed lines) were analyzed.

Appendix 3.6
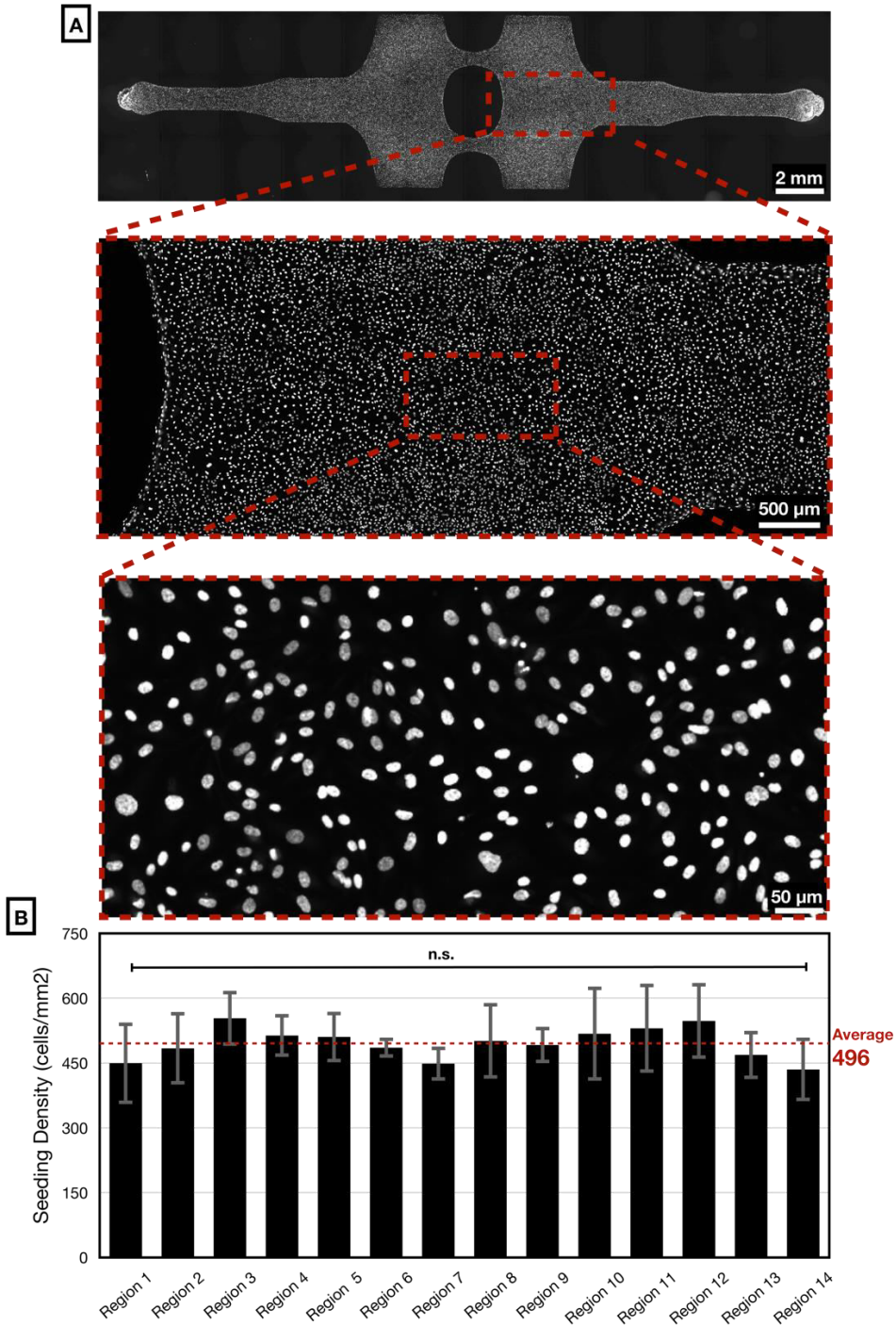
Uniform endothelial cell monolayer across the entire microfluidic chip. **(A)** Nuclei were stained with Hoescht 33342 and imaged with an epifluorescence microscope. Images show the distribution of the cells across the microfluidic chip with increasing magnification. **(B)**

Quantitative analysis of the cell seeding density showed the number of HUVECs per mm^2 of each region in the microfluidic chip, with the red dashed line showing the average of all the regions. The number of cells increased as the microchannels got wider. This would be expected as the cells can more easily attached to surface fibronectin when they slowed down in large microchannel regions. However, this change was not statistically significant (p=0.178 by one-way ANOVA). Data are presented as mean ± SD.

Appendix 3.7
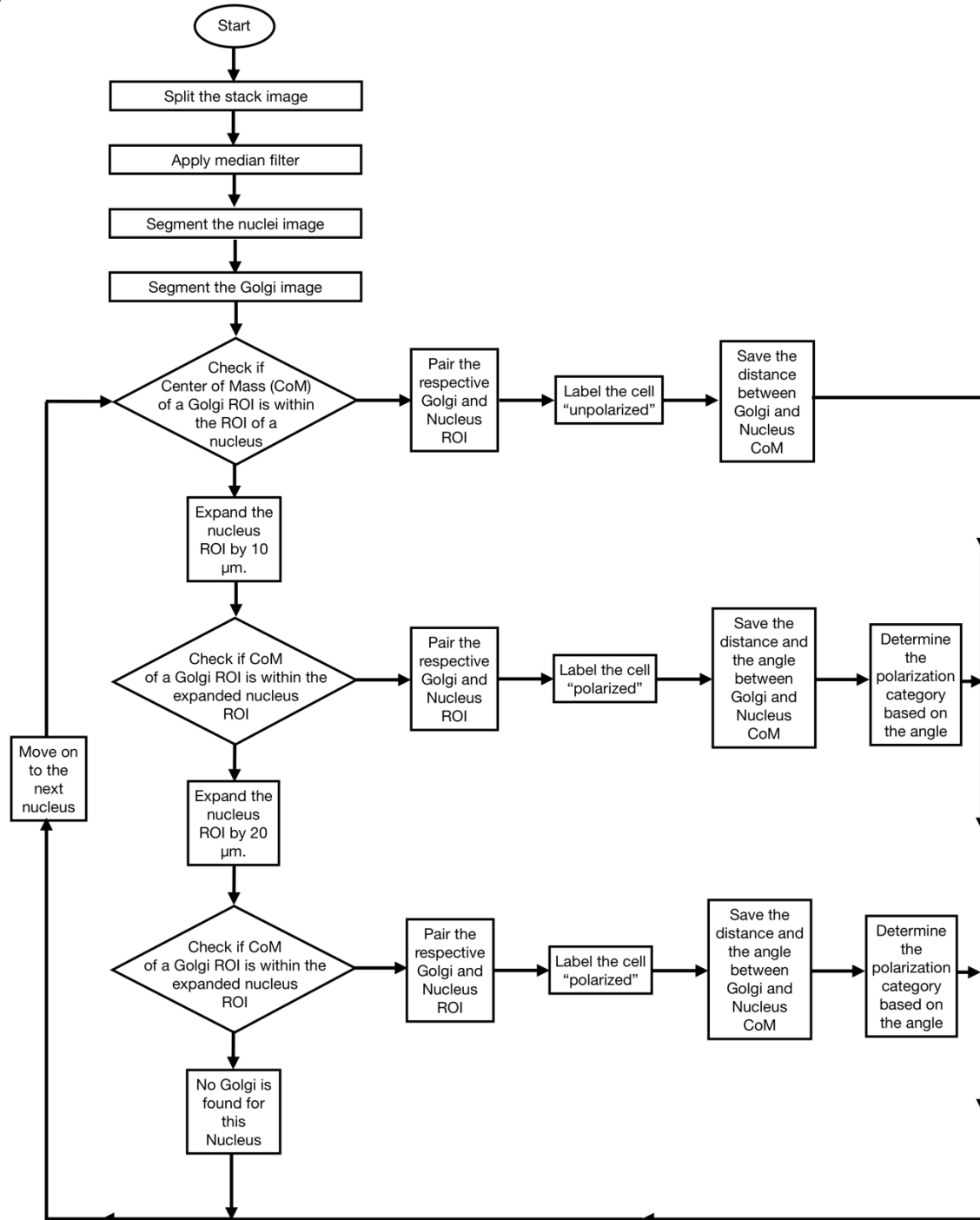
Flowchart of the macro for automated Golgi-nucleus polarization and orientation analyses. After the preprocessing for lowering the noise, the Golgi and nuclei are segmented and paired.

The cells where the center of mass (CoM) of Golgi are outside the nucleus are designated as polarized. The polarized cells are binned into four categories based on the angle of the vector connecting the center of the nucleus and Golgi. Within a 45° interval, if the Golgi is upstream of the nucleus, the cell is designated as upstream polarized. If the Golgi is downstream of the nucleus, the cell is designated as downstream polarized. If the Golgi is to the side of the nucleus, the cell is designated as right or left polarized. The macro produces a polarization map image where all nuclei are labelled with different colors based on their polarization category.

Appendix 3.8
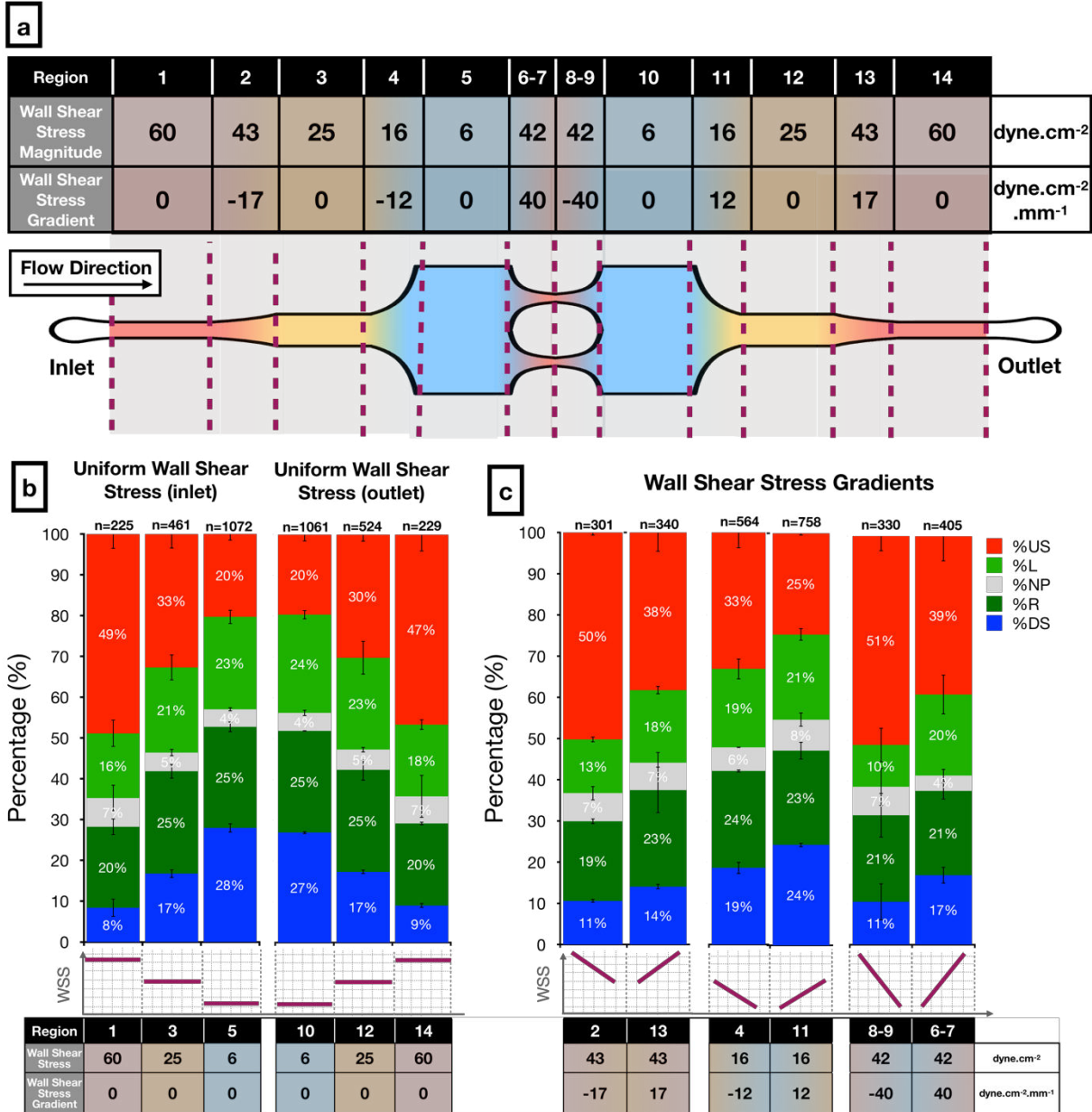
Golgi-nucleus polarization and orientation in a microfluidic chip with different dimensions that create higher magnitudes of wall shear stress (WSS) and steeper wall shear stress gradients (WSSG). Confluent human umbilical vein endothelial cells (HUVECs) were exposed to different shear stress modalities for 24 hours. **(a)** Schematic and table showing the magnitudes and slopes of the WSS and WSSG, respectively, across the microfluidic chip. **(b)** Stacked bar graphs

showing Golgi-nucleus orientation patterns of HUVECs in response to different levels of uniform WSS. **(c)** Stacked bar graphs showed the Golgi-nucleus polarization patterns of HUVECs that were exposed to different WSSGs.

In b and c, Golgi-nucleus orientation is indicated as upstream (red), downstream (blue), right (dark green), left (light green), or nonpolarized (gray). n = number of cells analyzed in each region. Data from a single experiment; mean ± SEM.

Appendix 3.9
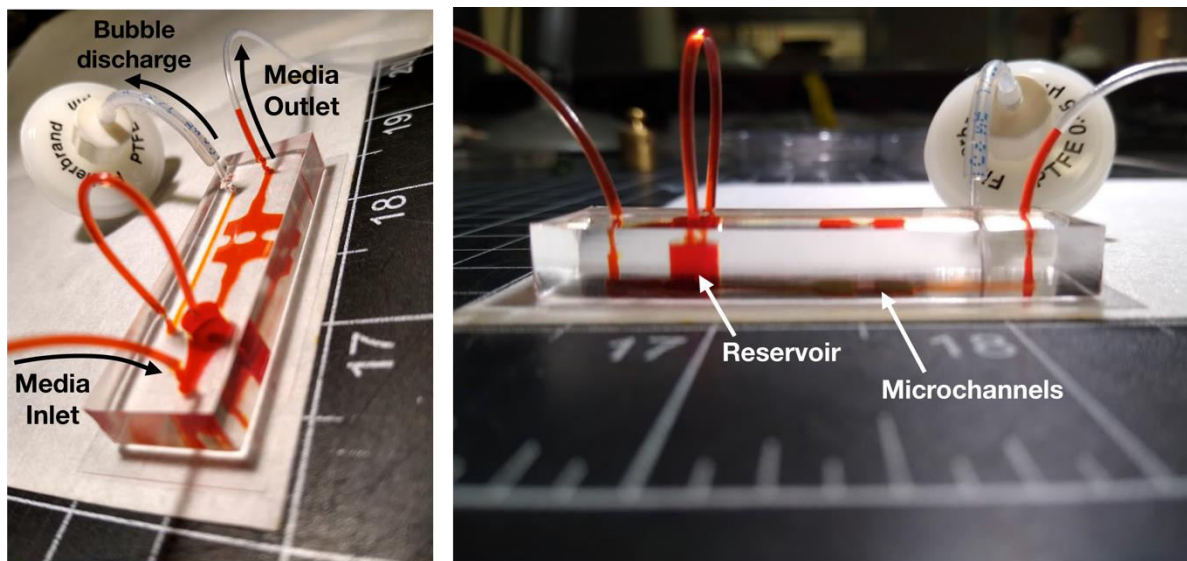
The on-chip integration of the bubble trap. Photos show the microfluidic chip with the integrated bubble trap for decreasing the "lab-around-the-chip". All the microchannels were filled with red food dye to facilitate visualization. The 2 mm diameter reservoir upstream of the microchannels was connected to a narrow bubble discharge channel that was plugged with a syringe filter to maintain sterility inside the microchannel. As the bubbles entered to the microfluidic chip through the inlet tubing, they rose and trapped in the reservoir region due to their buoyancy. Over time, these bubbles were pushed into the bubble discharge channel because of the positive pressure inside the microfluidic chip and they left the system through the membrane filter. In this way, the microchannels could be maintained bubble-free without using an external debubbler.

Appendix 4.1
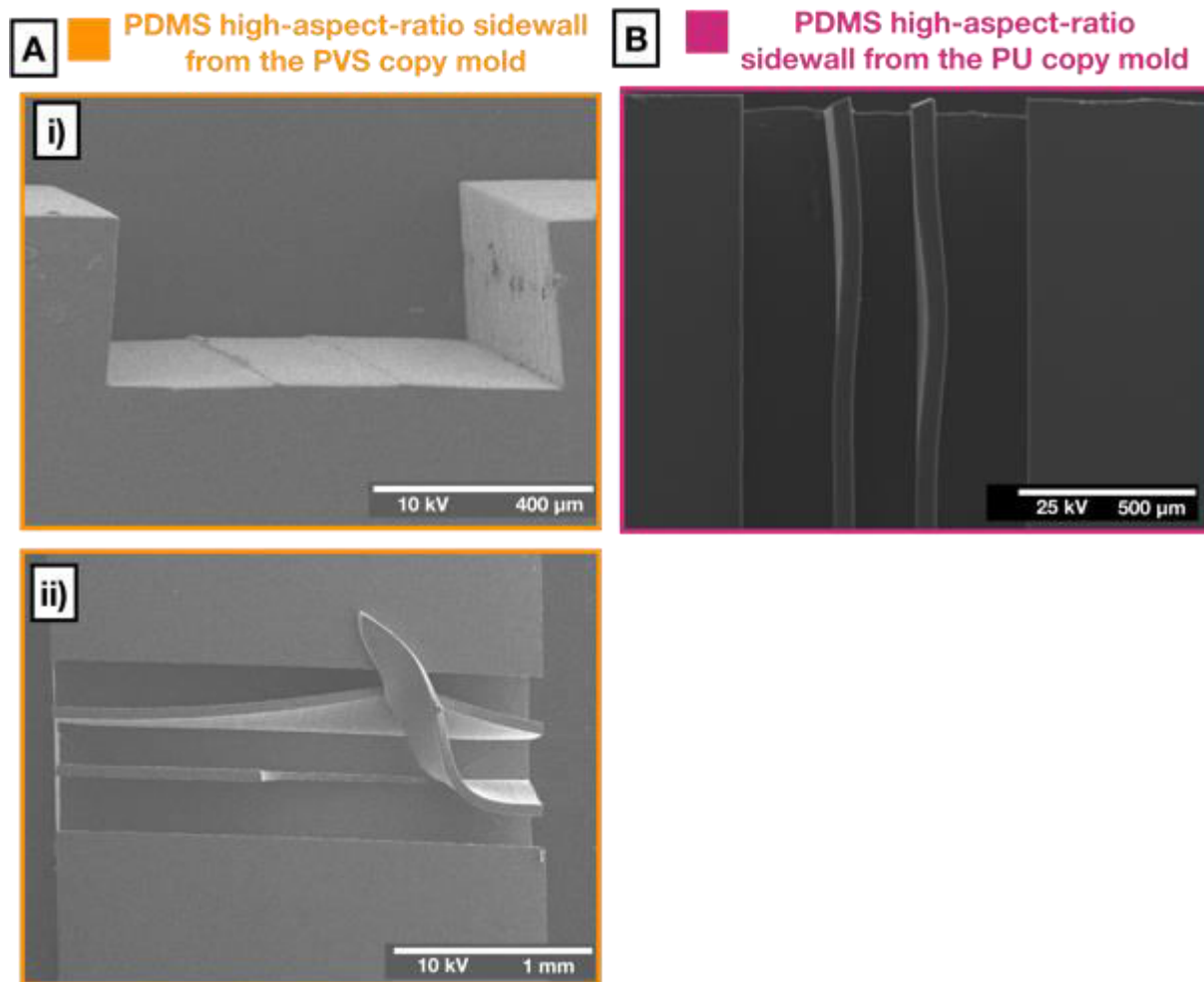
Failure of the structural integrity of the high-aspect-ratio PDMS structures fabricated through copy molds. (A) Adhesion of PVS copy molds[1] to PDMS structures either causes: i) total rupture or ii) partial tearing of the high-aspect-ratio protrusions. B) Pouring the liquid PU[2] on deformable PDMS molds led to distortion of the high-aspect-ratio sidewalls.

[1] M. E. Wilson, N. Kota, Y. Kim, Y. Wang, D. B. Stolz, P. R. LeDuc, O. B. Ozdoganlar, *Lab Chip.* 2011, *11*, 8.
[2] S. P. Desai, D. M. Freeman, J. Voldman, *Lab Chip.* 2009, *9*, 11.

Appendix 4.2
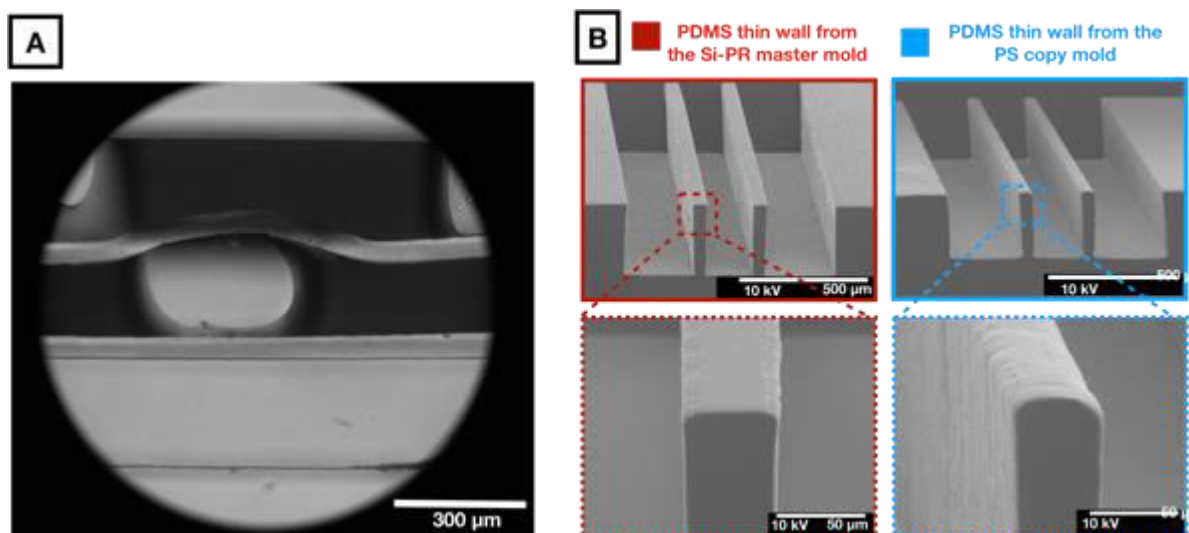
Failure of PDMS microchannels fabricated through a PS copy mold approach[1] in pressure based functional tests. **(A)** The PDMS microfluidic device fabricated through the PS copy mold failed after the application of pneumatic actuation, which caused leakage. Water with food dye was used to fill the central channel for visualization. **(B)** SEM images of the high-aspect-ratio PDMS side walls. Although the geometry was copied successfully, the rounded tips of the walls prevented strong oxygen plasma bonding between the PDMS and glass due to a lower contact area. This caused the failure of the entire device in the pressure based functional test.

[1] Y. Wang, J. Balowski, C. Phillips, R. Phillips, C. E. Sims, N. L. Allbritton, *Lab Chip.* 2011, *11*, 18.